Design and control of hybrid electric vehicle for efficient urban use.

Mehroze Iqbal

THESE DE DOCTORAT DE L'ETABLISSEMENT UNIVERSITE BOURGOGNE FRANCHE-COMTE

PREPAREE A FEMTO-ST
(Franche-Comté Électronique Mécanique Thermique et Optique - Sciences et Technologies)

Ecole doctorale n°37
Sciences Physiques pour l'Ingénieur et Microtechniques (SPIM)

Doctorat de Génie électrique

Par
M. IQBAL Mehroze

Design et contrôle d'un véhicule électrique hybride pour une utilisation urbaine efficace

(Design and control of hybrid electric vehicle for efficient urban use)

Thèse présentée et soutenue à UTBM (E107), le vendredi 09 septembre 2022

Composition du Jury:

M. Mickael HILAIRET (Pr.)	Université Bourgogne Franche-Comté	Président du jury
M. Emmanuel GODOY (Pr.)	L2S CentraleSupélec	Rapporteur
M. Olivier GEHAN (Dr.)	Ecole Nationale Supérieure d'Ingénieurs de Caen	Rapporteur
M. Abdel AITOUCHE (Pr.)	Université de Lille	Examinateur
Mme. Amel BENMOUNA (Dr.)	ESTA - École Ingénieur et Commerce	Examinatrice
M. Mohamed BENCHOUIA (Pr.)	Université Mohamed Khider Biskra	Examinateur
M. Mohamed BECHERIF (Dr.)	Université Bourgogne Franche-Comté	Directeur de thèse
M. Haitham Saad RAMADAN (Dr.)	L'Institut International sur le Stockage de l'Hydrogene	Codirecteur de thèse

Titre : Design et contrôle d'un véhicule électrique hybride pour une utilisation urbaine efficace.

Mots clés : Véhicule électrique hybride ; pile à combustible ; dimensionnement ; gestion de l'énergie en ligne ; dégradation ; environnement urbain

Résumé : L'objectif de cette thèse est de développer un cadre original et générique pour synergiser les aspects de design et de contrôle afin d'améliorer les perspectives des véhicules électriques hybrides (HEVs). L'application est spécifiquement illustrée pour la variante à pile à combustible des HEV (FCHEV). Une attention particulière est réservée aux environnements urbains en raison de nature intermittente, qui peut avoir un impact négatif sur les performances du véhicule.
Du point de la design, des paramètres spécifiques du véhicule sont utilisés pour dimensionner les composants FCHEV. En conséquence, une configuration de base est offerte, qui devrait assurer des performances stables, mais au détriment de sources surdimensionnées. Pour remédier à cette situation, un nouveau concept de coefficients de design flexibles est introduit afin d'attribuer une gamme de dimensionnement acceptable aux sources. Ensuite, les coefficients sont utilisés pour coordonner systématiquement le dimensionnement avec le gestion de l'énergie en ligne (OEMS).
Du côté du contrôle, la méthode de séparation des fréquences (FSM) est proposée comme un OEMS potentiel, en raison de sa flexibilité de réalisation en ligne. The applicability of a novel adaptive variant of FSM is explored. L'OEMS proposé est adapté à une performance cohérente, avec une attention réciproque à la consommation d'hydrogène et à la dégradation des sources. Pour cela, un concept de coût rationalisé et d'optimiseur en ligne basé sur l'horizon de recherche est proposé pour obtenir un compromis judicieux entre les principaux objectifs d'optimisation.
L'approche proposée est validée conceptuellement dans les simulations numériques réalisées sous MATLAB/Simulink. Plusieurs cycles de fonctionnement hypothétiques et un cycle avec des données de fonctionnement réelles sont étudiés en détail. L'applicabilité en temps réel de l'OEMS proposé est également validée par un banc d'essai expérimental avec un système électrique hybride à petite échelle.

Title: Design and control of hybrid electric vehicle for efficient urban use

Keywords: Hybrid electric vehicle; fuel cell; sizing; online energy management; degradation; urban environment

Abstract: This dissertation aims to develop an original and generic framework to synergize the design and control aspects to improve the prospects of hybrid electric vehicles (HEVs). The application is specifically depicted for the fuel cell variant of HEV (FCHEV). Special attention is given to urban environments because of their intermittent nature, which can have a negative impact on vehicle performance.
On the design side, specific vehicle parameters are utilized to size FCHEV powertrain components. Consequently, a unique baseline configuration is furnished, which is expected to provide consistent performance, but at the price of oversized sources. To overcome this, a novel concept of flexible design coefficients is introduced to assign an acceptable sizing range to sources. Then, the introduced coefficients are used to systematically coordinate sizing procedure with online energy management system (OEMS) of FCHEV.
At the control side, rules-based frequency separation method (FSM) is used as the standard OEMS, owing to its flexible online implementation. The applicability of a novel adaptive variant of FSM is explored. The proposed OEMS is tailored for consistent performance, with reciprocal awareness towards hydrogen consumption and sources degradation. For that, a concept of rationalized-cost and search-horizon based online optimizer is introduced to reach an insightful trade-off among the key optimization objectives.
The proposed coordinated approach is conceptual validated in the numerical simulations realized under MATLAB/Simulink. Several hypothetical driving cycles and a cycle with real driving data is extensively studied. The real-time applicability of proposed OEMS is also validated by an experimental test-bench with small-scale hybrid power system.

Design and control of hybrid electric vehicle for efficient urban use

Dissertation for the Doctoral studies in Electrical Engineering

Doctoral School: **SPIM**

Author: **Mehroze IQBAL**

Director: **Dr. Mohamed BECHERIF**

Co-director: **Dr. Haitham S. RAMADAN**

Abstract of dissertation

Electrification of transportation sector is a leading candidate to tackle the persistent dependence on depleting gasoline fuels, and thus reduce the air pollution and the global warming. In this context, hybrid electric vehicle (HEV) in general and fuel cell hybrid electric vehicle (FCHEV) in particular are the technological innovations that offer considerable potential thanks to their ecological, efficient, and silent operation. Compared to its competitors, the FCHEV outperforms gasoline powered HEVs in terms of emissions production. In addition, the increased travelling range and reduced refueling time are facilitated compared to battery electric vehicles. Despite their unique attributes, the existing commercial competitiveness of FCHEVs is lagging the competition. Among numerous factors to blame, the major ones are higher manufacturing cost, inadequate refueling facilities, and durability issues. A systematic coordination of both the design and control aspects with a balanced trade-off between ownership price, hydrogen consumption, and source degradation is the key to resolve these shortfalls. With this background, this dissertation proposes an original solution to coordinate the sizing procedure with the online energy management of FCHEV, beside improving both aspects at the individual level.

In the first stage, a generic methodology is implemented to size the FCHEV powertrain elements by leveraging specific vehicular parameters such as the desired acceleration response and the maximum vehicle speed. The first stage yields a unique baseline powertrain system which is expected to provide consistent performance under a variety of driving conditions. However, the baseline system generally favors oversized energy sources. To overcome this limitation without compromising the vehicle performance, a novel concept of flexible design coefficients is introduced to assign an acceptable sizing range to the energy sources. Then, the introduced design coefficients are used to systematically coordinate the sizing procedure with the online energy management system (OEMS) in the second stage. Consequently, the most appropriate FCHEV configuration is selected from the assigned sizing range with an informed trade-off among key operational objectives.

The second stage details the steps involved in the design of FCHEV's OEMS. Essentially, the rule-based frequency separation method (FSM) is used as the baseline OEMS, owing to its flexible online implementation. The applicability of a novel adaptive variant of FSM is extensively explored. The proposed OEMS is tailored to support consistent performance under a wide range of driving situations, with reciprocal awareness of both hydrogen consumption and sources degradation. For this purpose, a concept of rationalized-cost is introduced to reach an insightful trade-off among the considered optimization objectives. Thereafter, a search-horizon based online optimizer is developed to tune the frequency-driven power separation rule (PSR) subject to instantaneous minimization of the rationalized-cost. To realize the storage system limitations indicated by soft/hard constraints, a dedicated repair procedure based on droop-criteria is integrated to dynamically adjust the charging/discharging rates of the storage devices.

In the final stage, the conceptual and practical performance of the proposed methods is critically evaluated in various driving environments and in a variety of vehicle configurations via numerical simulations and experimental setup. Special attention is given to urban driving cycles, because of their stringent and intermittent speed requirements, as well as extended start-stops. These distinct characteristics can have a negative effect on the health of sources, hydrogen consumption, and operational efficiency. However, the investigation is not limited to urban cycles only, and several standard hypothetical driving cycles, such as WLTP (class 1), LA92, US06, and Artemis (highway and urban) are studied. Moreover, the driving cycle with real driving data such as ETC FIGE-4 is also adopted to reflect what can be expected from the proposed method in the real environments. Finally, a hybrid fuel cell/battery electric vehicle is studied with parameters similar to a commercial grade vehicle (Toyota Mirai), and performance is statistically compared against the distinct variants of FSM based OEMS such as offline tuned FSM and conventional FSM. Figure 1 presents the graphical abstract of presented workflow.

The proposed scheme to coordinate the design and control aspects is readily scalable to a variety of hybrid vehicles with different configurations and profiles. In addition, the proposed OEMS is expected to provide reliable performance under various driving conditions. The adaptive nature of OEMS should also provide a reasonable trade-off between the fuel consumption and the sources degradation.

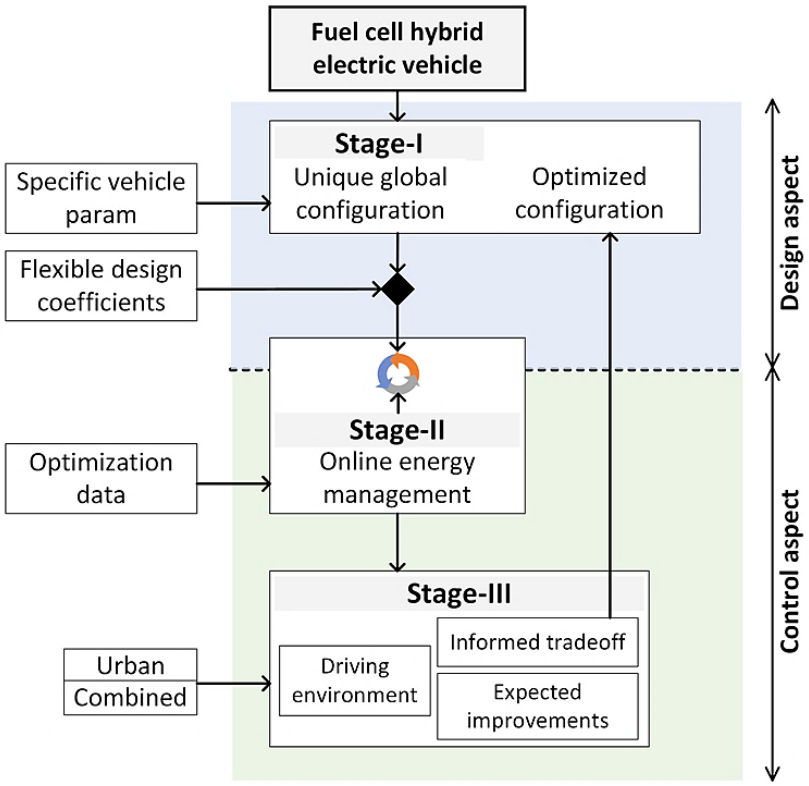

Figure 1: The graphical abstract of research workflow.

Table of contents

List of figures

List of tables

Nomenclature

BEV	:	Battery electric vehicle	GHG	:	Greenhouse gasses
BoL	:	Beginning-of-life	ICE	:	Internal combustion engine
CF	:	Convex framework	ICEV	:	Internal combustion engine vehicle
CO	:	Convex optimization	ICEHV	:	ICE hybrid vehicle
DP	:	Dynamic programming	HEV	:	Hybrid electric vehicle
DoH	:	Degree of hybridization	LAD	:	Level of accelerated degradation
EEC	:	Equivalent energy consumption	ODS	:	Optimization-driven strategies
EF	:	Equivalent factor	OEMS	:	Online energy management system
EMS	:	Energy management system	PEMFC	:	Proton exchange membrane FC
ESD	:	Electrical storage device	PSR	:	Power separation rule
ESM	:	Extremum seeking method	PI	:	Proportional-integral
EoL	:	End-of-life	PMP	:	Pontryagin's minimum principle
FC	:	Fuel cell	PH	:	Predictive horizon
FDC	:	Flexible design coefficients	RDS	:	Rules-driven strategies
FCHEV	:	Fuel cell hybrid electric vehicle	SC	:	Supercapacitors
FSM		Frequency separation method	SoH	:	State-of-health
FL	:	Fuzzy logic	SoC	:	State-of-charge
GA	:	Genetic algorithm			

Chapter 1: General introduction

The introductory chapter of dissertation presents contextual background, primary motivations, and objectives of this research work. Accordingly, the scientific contributions of this research work are outlined, and the plan of dissertation is detailed in a brief manner.

1.1 Background and motivation

Global warming, fossil fuel depletion, and air pollution are among the most pressing issues confronted by the modern society. The transportation sector, in essence, can play a central role in alleviating these concerns. In addition to its prominent energy consumption, the transportation sector is one of the leading producers of greenhouse gas (GHG) emissions. According to international energy agency, the transportation sector contributed 24% of global GHG emissions in 2018, and 74% of these emissions were originated from road transportation [1], as depicted in Figure 2a. At the national level, a study conducted in [2] indicates that in Metropolitan France, on average 29% of total emissions resulted from transportation, as shown in Figure 2b. With the present conditions, this trend is expected to increase with the continued reliance on the conventional fuels.

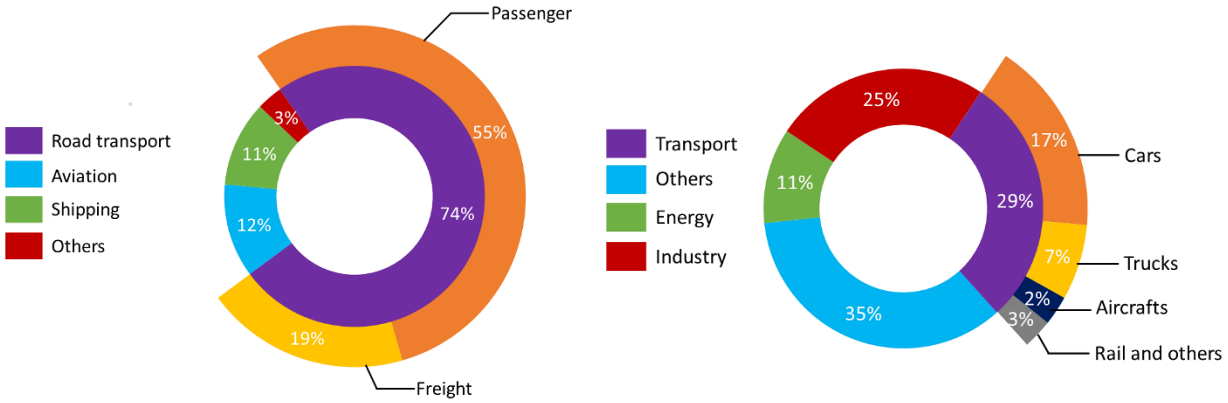

a) Global sector-wise GHG emissions [1]. b) Sector-wise GHG emissions in France [2].

Figure 2: Contribution of the transportation sector towards GHG emissions.

In this context, to reduce the sustained reliance on depleting fossil fuels and to curtail greenhouse gas emissions, conventional vehicles are expected to be banned by 2040 in the United Kingdom [3]. Likewise, by 2050, the Europe aims to reduce GHG emissions up to 80% by completely electrifying the transportation sector [4]. The electrification of transportation sector is therefore prompting rapid advances in the hybrid vehicles, which are recognized as ecological alternatives to their conventional counterparts. Another important consideration is that the fully electrified vehicles can be powered by green sources such as photovoltaic and wind turbines [5, 6]. Thus, the complete transportation cycle is entirely green (from the green sources to the wheels) [7, 8].

The transportation sector in general and vehicular technology in particular have undergone extensive research over the past decade, particularly within the electrification paradigm. Electrification, in general, consists of powering the vehicle propulsion system from an electrical source in order to entirely or partly decrease the dependence on gasoline fuels. Subsequently, the simplest and the most feasible option is the battery electric vehicle (BEV), for which the internal combustion engine (ICE) is completely replaced by an electric motor paired with a battery system [9, 10]. A pure BEV is a noiseless and emission-free alternative to internal combustion engine vehicles (ICEVs). In addition, the BEV traction motor delivers superior operating efficiency compared to ICEV. However, on whole, BEVs have some technical shortcomings, such as reduced autonomy, longer charging time, and safety issues [11]. Hybridizing the conventional ICE and a contemporary battery system into a single package (ICEHV) is a commercially and technically promising proposition that can exploit the benefits of both systems [12]. To name a few, ICEHV technology can improve both the driving range and fuel efficiency. In addition, a plug-in option can also be provided in ICEHV to extend the autonomy by charging the battery through external means [13].

Nevertheless, the fundamental problem of using gasoline as primary fuel in HEVs still exists. In addition, charging the battery from power grid can substantially raise the emissions over long term. In this regard, the pursuit of an adequate and environmentally friendly option to completely replace the traditional ICE has become highest priority across the transportation sector [14]. As a promising prospect, the fuel cell (FC) technology can replace ICE in the ICEHVs to avoid reliance on depleting gasoline fuels with zero emissions and noiseless operation [15]. The FCHEVs are therefore receiving growing interest, as they can offer reduced refueling times and extended driving autonomy compared to BEVs [16]. These distinct operational characteristics render FCHEVs a superior option compared to competing HEVs.

Despite distinct merits, the mainstream acceptability of FCHEVs is lagging that of the competition. Several technical shortfalls, such as higher ownership price [17], limited refueling infrastructure [18], and durability issues [19] are the main culprits. These shortcomings can be resolved by improving and synergizing the design and control aspects in an efficient manner. The former aspect can be improved by properly configuring the FCHEV's powertrain components with a fair trade-off between design and operational economy. The latter aspect can be improved by reducing the hydrogen consumption and prolonging the sources lifespan, which is achieved at the energy management level. Nonetheless, an 'optimal operational and design economy' can only be achieved by systematically coordinating the sizing aspect with the OEMS, in addition to improving both aspects at the individual level.

Motivated by the importance of this emerging research area, the dissertation aims to develop an original and generic framework to synergize design and control aspects in order to improve the prospects of FC technology in the vehicular applications. The proposed framework is applicable

in a consistent and effective manner to a variety of HEVs as well as to a diverse range of driving environments.

1.2 Aim and objectives

The research work aims to improve the prospects of FCHEVs by introducing decisive and ingenious technical developments. The essential design and control aspects are coordinated systematically, in addition to their optimization at the individual level. To achieve the intended goal, different research objectives are defined as follows:

- *Design aspect*: To select a commercially viable topology of FCHEV powertrain system. Afterwards, devise a generic procedure to deliver a unique global configuration of the selected powertrain system.
- *Control aspect*: To develop a robust and driving-environment resilient OEMS, with mutual awareness towards key operation objectives such as hydrogen consumption, and sources degradation. With this vision, the rules-based control techniques are proposed due to their flexible nature. However, vehicle operation with rule-based techniques is not necessarily optimal. To solve this problem, an adaptive framework is offered to update the power separation rules in an instantaneous manner.
- *Coordination aspect*: To present systematically coordination of the sizing aspect and OEMS of FCHEV. The proposed scheme is expected to yield an appropriate powertrain configuration with an informed compromise among manufacturing and operational economy.
- *Validation aspect*: To construct both a conceptual and an experimental evaluation criterion for the performance demonstration of proposed methodologies under a wide range of driving conditions and for distinct vehicle profiles. A special section is reserved for urban driving environments, as they are characterized by severe and intermittent speed requirements, which may negatively impact the vehicle performance.

1.3 Scientific contributions

The flow of research work is presented in Figure 3, which resulted in numerous scientific contributions, including the generic tool, the experimentally validated solution, and the research articles. The details are as follows:

- A generic MATLAB/Simulink based tool to configure and size the powertrain elements of FCHEVs. The application can be easily extended to a range of HEVs with distinct profiles and dimensions. Moreover, the proposed tool also facilitates a controlled trade-off among design and operational economy, when coordinated with the OEMS.
- An experimentally validated power conditioning setup consisting of parallel connected boost converters. The setup is appropriate for FC based high power setups devoted to vehicular applications.

- A driving-environment resilient OEMS equally effective for hypothetical and commercial-grade hybrid powertrain systems. Traction power is distributed among hybrid propulsion sources with simultaneous consideration of fuel economy, and source degradation.
- Robust and efficient low-level control for interleaved and classical power conditioning devices. Two techniques are proposed: the classical proportional-integral compensator and the global model predictive controller.
- The research work has led to several articles published in reputable journals. The details are as follows [20-23]:

  - **IQBAL Mehroze**, LAURENT Julien, BENMOUNA Amel, BECHERIF Mohamed, et al. Ageing-aware load following control for composite-cost optimal energy management of fuel cell hybrid electric vehicle. *Energy*, 2022, p. 124233.
  - **IQBAL Mehroze**, BECHERIF Mohamed, RAMADAN Haitham S., et al. Dual-layer approach for systematic sizing and online energy management of fuel cell hybrid vehicles. *Applied Energy*, 2021, vol. 300, p. 117345.
  - **IQBAL Mehroze**, RAMADAN Haitham S., and BECHERIF Mohamed. Health-aware frequency separation method for online energy management of fuel cell hybrid vehicle considering efficient urban utilization. *International Journal of Hydrogen Energy*, 2021, vol. 46, no 29, p. 16030-16047.
  - **IQBAL Mehroze**, BENMOUNA Amel, ELTOUMI Fouad, et al. Cooperative operation of parallel connected boost converters for low voltage-high power applications: an experimental approach. *Energy Procedia*, 2019, vol. 162, p. 349-358.

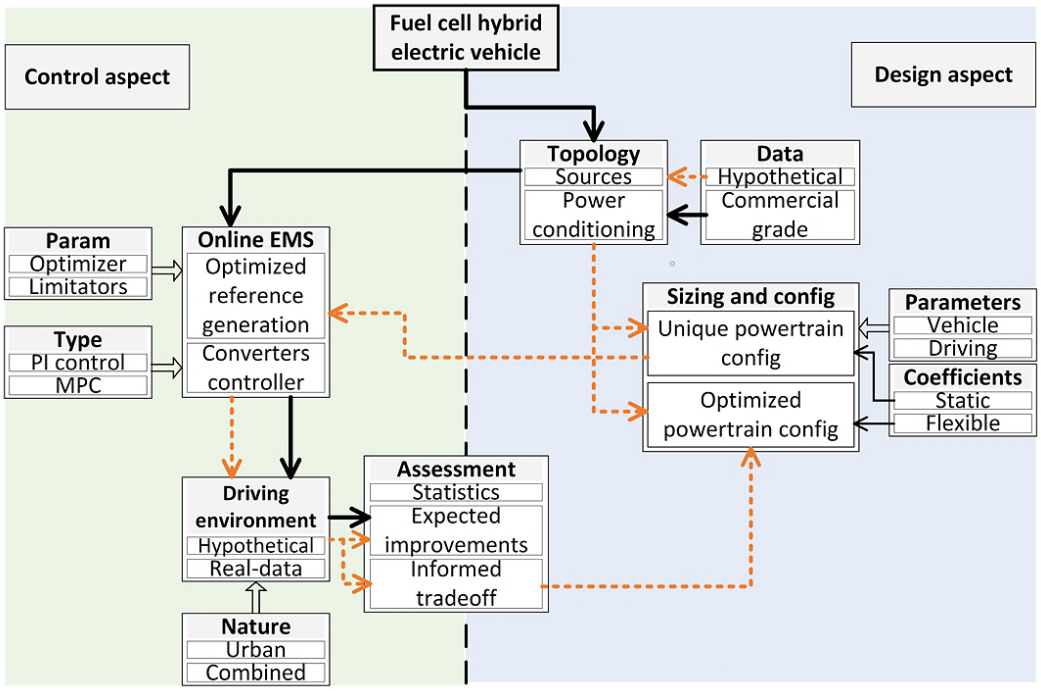

Figure 3: Schematic diagram exhibiting the procedural flow of research work.

1.4 Dissertation outline

The residual of dissertation is briefly outlined as follows:

- Chapter 2: State-of-the-art presents emerging development trends in the context of HEV technology. The relative competitive positioning of FCHEV is discussed. Various state-of-the-art techniques for configuring the propulsion system of FCHEV are elaborated as well as cutting-edge OEMS are described.
- Chapter 3: The proposed approach for key design aspects details the complete procedure to design an FCHEV subject to on-road requirements. The process begins with the proper selection of energy sources and their mathematical modeling. Next, hypothetical and practical layout schemes are presented with the studied power conversion topologies. Finally, the generic sizing and configuration method based on design coefficients is presented to identify the base configuration and the flexible but practical sizing range.
- Chapter 4: The proposed approach for key control aspects presents the proposed approach for the key control aspects of studied FCHEVs. The background and working philosophy of the proposed OEMS based on frequency separation method is presented alongside developed converter control schemes. The detailed mathematical formulation including the optimization and decision frameworks are jointly laid out for the proposed high/low level control schemes of the studied FCHEVs.
- Chapter 5: Results and discussion is dedicated for the critical evaluation of the developed methods to address the key design and control aspects of the studied FCHEVs. Various vital operational aspects of the considered hypothetical vehicles such as power balance, hydrogen consumption and sources degradation are comprehensively studied, and compared with the established approaches. The study is extended to the vehicle for which the specifications are matched with those of a commercial-scale FCHEV. A separate portion is also dedicated to study the behavior of studied vehicles in the driving environments with real driving data. The relevant experimental work and the associated findings are presented as a concluding remark of this chapter.

Chapter 2: State-of-the-art

This chapter presents the established development trends in the domain of hybrid vehicles technology. In particular, the positioning of FCHEV relative to the competing hybrid electric vehicles is elaborated. Thereafter, the state-of-the-art methodologies for appropriately configuring the FCHEV propulsion system are rigorously discussed together with the contemporary energy management systems.

2.1 Established development trends

The most established commercial-scale hybrid vehicles are depicted in Figure 4. From the presented types, the ICHEV topology illustrated in Figure 4a is the most popular one, which employs both the conventional ICE and battery coupled with the motor to provide the necessary traction power. An excellent example of this type of vehicle is Toyota Prius, which is considered a commercial success [24]. The distinct advantages of ICEHVs are mature technology, fast refueling time, and cost-effectiveness. However, a significant portion of traction energy is provided by ICE, which may result in GHG emissions. In contrast, the HEV illustrated in Figure 4b provides entire traction power through the electric motor, thus providing environment friendly experience. However, the larger battery in Figure 4b is charged by a comparatively smaller ICE or by external means, which can increase emissions. To mention just one, Nissan e-Note is a very popular battery-powered HEV [25]. The most recent HEV shown in Figure 4c offers purely clean and quiet operation, as well as short refueling time and extended range. Such a configuration is present in Toyota Mirai, which is a commercial-grade FCHEV [26].

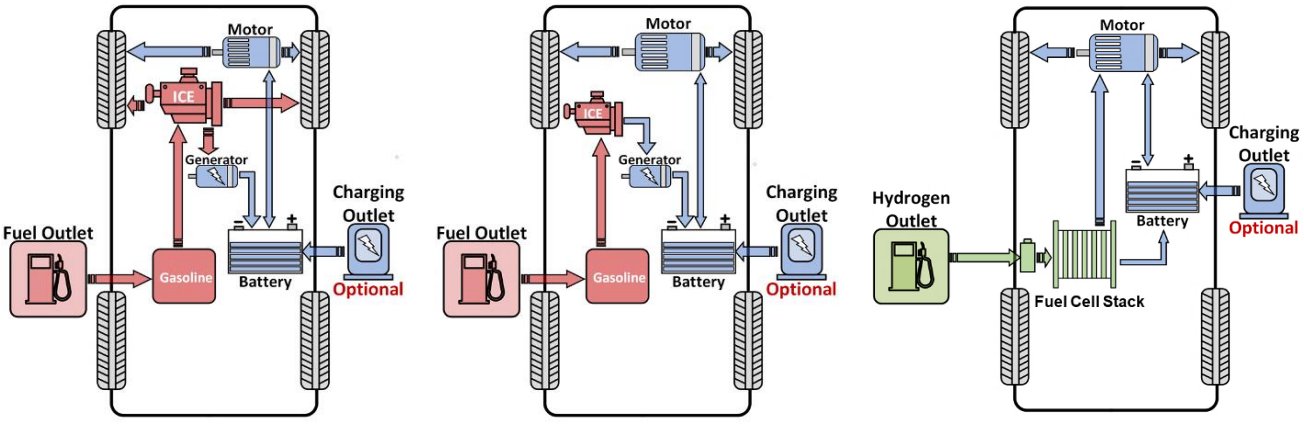

a) ICEHV topology. b) Battery-powered HEV. c) FC-powered HEV (FCHEV).

Figure 4: Established development trends in the hybrid vehicles technology.

Compared to the competitive HEVs exhibited in Figure 4(a, b), the major attributes of FCHEV are presented in Table 1. To reach the future goal of emissions free society, FCHEVs are considered

as the most promising solution. However, several techno-economic shortcomings such as higher ownership price, durability issues, and non-streamlined refueling infrastructure hinder the current acceptance rate of FCHEVs compared to the competition, and impact the future market value of FCHEVs [27]. To address these shortcomings, an effective approach is essential to systematically coordinate both the design and control aspects, in conjunction with introducing the individual-level refinements.

Table 1: Attributes and positioning of FCHEV in relation to the competition.

Hybrid vehicle type			ICEHV	Battery-powered HEV	FCHEV
Technology	Energy sources	ICE	✓	✓	×
		Battery	✓	✓	✓
		FC	×	×	✓
	Fuel outlet	Gasoline	✓	✓	×
		Electric	✓	✓	✓
		Hydrogen	×	×	✓
	Traction element	ICE	✓	×	×
		Motor	✓	✓	✓
Attributes	Maturity (technology)		+++	++	+
	Relative acceptance		+++	++	+
	Relative emissions		++	+	NA
	Fuel economy (gasoline)		+	++	NA
	Gasoline usage		++	+	NA
	Average starting torque		+	++	++
	OEMS design complexity		+++	++	+++
	Durability (sources)		++	++	+
	Refuel infrastructure (non-electric)		+++	+++	+
	Electric range		+	++	++
	Refuel time (non-electric)		+	+	+
Legends: '+' indicates improvement/de-improvement trend, 'NA' not applicable.					

2.2 The design aspects

The term 'design' covers a broad terminology ranging from the selection of propulsion sources to the arrangement of these sources in a viable topological structure, and the appropriate sizing of propulsion components to achieve certain manufacturing and operating goals. The first step is

to select both the main and auxiliary power sources of HEV in order to provide the optimal traction power in diverse operating scenarios.

Within the paradigm of FCHEV, the proton exchange membrane FC (PEMFC) stands out as the core energy source. Compared to its counterpart ICE, the PEMFC utilizes a clean chemical reaction between hydrogen and oxygen to produce electrical energy for relatively efficient traction motor [28, 29]. The PEMFC typically has slower dynamics and a slower start-up due to its chemical nature, and the existence of an air compressor [30]. Therefore, sudden variation in the load demand, frequent braking/acceleration, and stop/starts can lead to fuel starvation, membrane drying, deterioration of health, and ultimately permanent damage to the PEMFC [31]. Moreover, the PEMFC is a unidirectional power source, and cannot store regenerative energy during braking, which lowers its operational efficiency [32]. A stand-alone structure based solely on PEMFC is therefore impractical for automotive applications as it may result in higher manufacturing cost, rapid degradation, and increased hydrogen consumption [33, 34]. This attribute exhibits standalone viability of PEMFC technology as an inferior option compared to ICEHV and Battery-based HEV.

The solution to alleviate the problems related to dedicated operation of PEMFC is to adopt auxiliary energy storage devices (ESDs) with a relatively faster dynamic response. The storage devices compensate for the slower response of PEMFC as it prefers to function under relatively stable conditions and can potentially reach its maximum efficiency at partial load only. Mixing various power sources also minimizes the principal size of PEMFC stack, enhances dynamic response, improves operational efficiency, and provides reversibility during regenerative braking [35]. There are two practical options to be considered from ESDs: the batteries pack and/or supercapacitors bank [36, 37]. The selection of either or both of these storage elements can be decided based on some qualitative metrics such as energy and power density, lifespan, affordability, durability, and responsiveness, etc. The battery usually has a higher energy density (compared to supercapacitor), moderately high charge/discharge cycles in the neighborhood of 300-400, and low self-discharge [38]. Compared to battery, the supercapacitor (SC) has a higher power density, faster response and comparably much higher charge/discharge cycles, giving it a life span 10 to 100 times longer than battery [39]. The power/energy density of FCHEV energy sources are exhibited in Figure 5 using a ragone-chart. By combining hybrid storage elements, an efficient powertrain topology can be constituted with an adequate compromise between overall drivetrain power and energy density. This makes it possible to achieve higher efficiency while having a reliable system and significantly reducing the cost and weight of vehicle.

2.2.1 Layout and topologies

The choice of powertrain topology is among the key factors that impact manufacturing and operating economics of FCHEV as well as its performance. In general, the PEMFC system is always connected to the traction motor via a devoted DC-DC boost converter [22, 40]. While ESDs are

connected to load, either with or without bidirectional DC-DC converters to prioritize a particular or multiple attribute [41, 42].

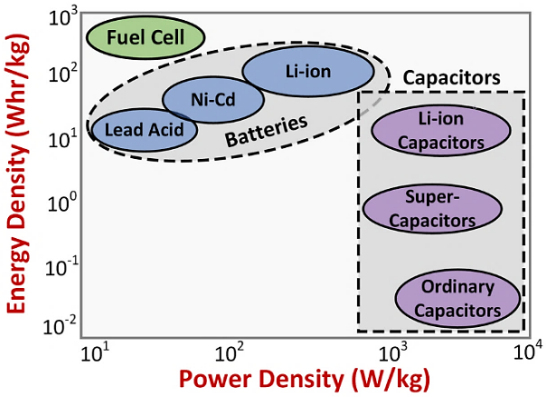

Figure 5: Ragone-chart exhibiting power/energy densities of FCHEV sources.

Based on the selection and placement of drivetrain components, the topological structures of FCHEV [43], and their attributes are comprehensively presented in Figure 6 and Table 2. Among these topologies, the configurations presented in Figure 6(a, b) are considered commercially feasible in favor of their simpler design and easier implementation of OEMS [44, 45]. However, the explicit attributes of sources cannot be fully leveraged due to a semi-active layout, which may adversely influence the operational performance in some driving scenarios. On the other hand, the topologies exhibited in Figure 6(c, d) depict a complex topological structure and thus a cumbersome design of OEMS, which initially portrays their inferiority. Nevertheless, the presence of an active topological structure opens the possibility of properly exploiting the attributes of hybrid sources, leading to a better overall operational performance [46, 47]. Furthermore, with the versatility of multi-sources, the components, particularly the PEMFC can be downsized to reduce manufacturing cost. Thus, with the prominence of goal oriented OEMS and methodical sizing methods, the topologies in Figure 6(c, d) have greater long-term advantages.

Table 2: Qualitative comparison among key attributes of FCHEV layout schemes.

Parameters	Topologies (Refer to Figure 6)			
	(a)	(b)	(c)	(d)
Design complexity	+	++	+++	++++
OEMS complexity	+	++	+++	++++
Converters losses	+	++	+++	++++
Flexibility	+	++	+++	++++
PEMFC downsizing	+	+	++	++
Reliability	+	+	++	++
Legends: '+' indicates the improvement/de-improvement trend.				

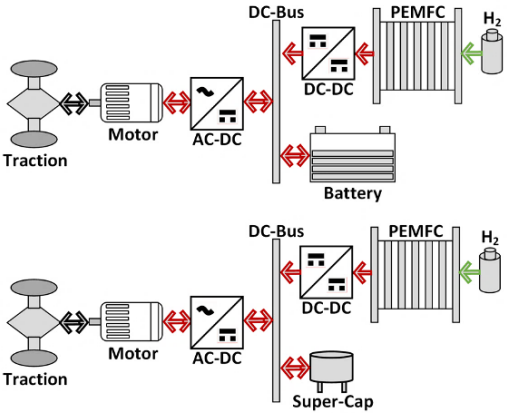

(a) Uncontrolled unitary storage.

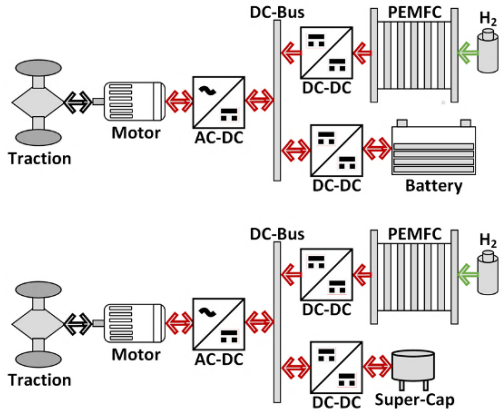

(b) Controlled unitary storage.

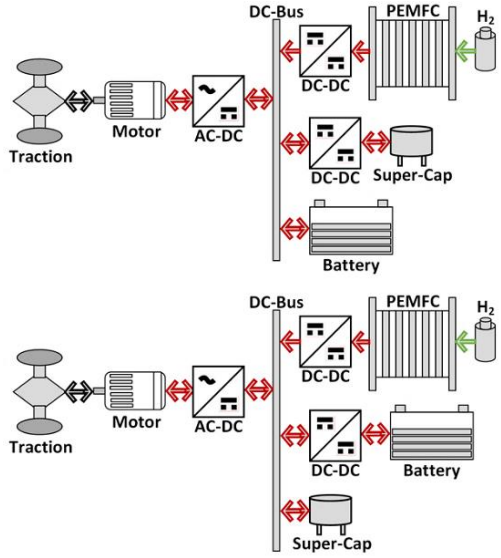

(c) Compound multi-storage.

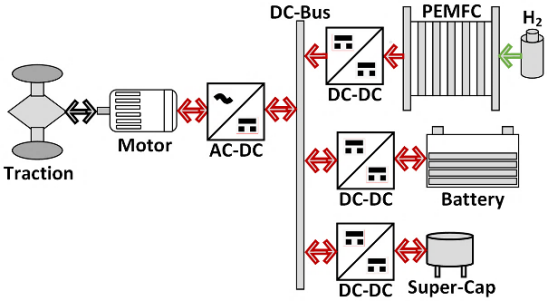

(d) Controlled multi-storage.

Figure 6: Generalized layout schemes of FCHEV powertrain system.

2.2.2 Sizing and configuration techniques

As two essential technical aspects, sizing and energy management system (EMS) have a profound effect on the manufacturing and operational economics of FCHEVs [48, 49]. In general, common aims are shared by sizing and EMS, such as fuel consumption and source degradation are equally affected. However, there are some exceptions, such as the manufacturing economy which is explicitly related to sizing procedure, and the charge sustainability as an operational aspect that can be fully realized at the EMS level. Researchers have proposed diverse approaches regarding sizing and OEMS, in order to decrease expected manufacturing price of FCHEV and enhance its operational performance. The conclusive summary of widely adopted techniques and their merits/demerits are comprehensively compared in Table 3.

2.2.2.1 Detached sizing for generic configuration

In this approach the energy sources of FCHEV are dimensioned exclusively based on the desired driving characteristics, such as maximum sustained speed and acceleration behavior. This method results in a generic configuration that facilitates consistent performance under a wide range of driving scenarios. However, oversized energy sources are typically favored and awareness of operational goals is not assured, as presented in [50]. Where, a 50 kW PEMFC is selected to cruise at a sustained speed of 100 km/h. Arguably, any driving situation characterized by lower speed cutoffs can constrain 50 kW PEMFC to operate in an unsuitable underloading zone. As a result, the degradation phenomenon of PEMFC increases and so does the fuel consumption. To address this issue, authors of [50] devised an online OEMS based on fuzzy logic (FL), where the membership functions are tuned using genetic algorithm (GA) to increase fuel economy and operating efficiency. Though, there are two prominent shortfalls as indicated by the authors of [50]. The sources degradation being an important aspect is not considered at EMS level. In addition, the tuning process is performed using an offline optimizer, which calls into question the efficacy of this approach in terms of achieving operational goals in real-time scenarios.

Table 3: The conclusive summary of already established sizing and configuration techniques.

Sizing Method	Concept	Resultant configuration			Economy realization			Implementation		Technical shortcoming	
		Generic	Near-optimal	Optimal	Operational		Ownership	Online	Offline	Oversize	Complexity
					Fuel	Degrade					
Detached	Specific vehicle param. [50]	✓	×	×	×	×	×	✓	×	++	×
	DoH [48, 51, 52]	×	✓	×	+	+	+	×	+	+	+
Coordinated optimization	Single-level [53-55]	×	×	✓	++	++	++	×	++	×	++
	Bi-level [56-58]	×	×	✓	++	++	++	×	++	×	++
Legends: '+' indicates improvement/de-improvement trend.											

2.2.2.2 Detached sizing for near-optimal configuration

This approach is indistinguishable to previous technique (Section: 2.2.2.1) in a way that sizing, and configuration are performed as independent steps. However, instead of configuring FCHEV powertrain system according to driving characteristics, the sizing procedure is performed by studying the relative sizing range on the operational criteria. These criteria can be fuel

consumption, health degradation and/or charge sustainability. Early studies explored the influence of relative size range, also known as 'degree of hybridization (DoH)', on vehicle performance. The impact of DoH on the fuel economy of FCHEV is examined by researchers from Toyota motor corporation in [59]. Likewise, the relationship between DoH and FCHEV fuel consumption is studied in [51] using ADVISOR platform. The suboptimal assortment of DoH can yield oversized components, which can increase the manufacturing price. To address this issue, optimization aspect is integrated in DoH [52], where an offline metaheuristic optimizer is built to investigate the influence of DoH on the fuel economy as well as ownership price of FCHEV. The pareto-optimization framework is regarded as an expedient tool to establish an adequate trade-off between conflicting objectives [60, 61]. Considering this, an off-line pareto-optimizer is formulated in [48] to establish a right compromise among fuel economy and manufacturing price of FCHEV. However, the higher computing complexity is a known disadvantage associated with the pareto-optimization framework [62]. In addition, health degradation is another important operational aspect that is not considered.

2.2.2.3 Coordinated single-level sizing for optimal configuration

The heuristic sizing of energy sources limits the full potential of FCHEV [53]. Therefore, the sizing and configuration procedure should be coordinated with the OEMS of FCHEV [63]. In this context, 'truly optimal operational and design economy' can only be achieved with combined sizing and EMS [57]. To simultaneously study the sizing of propulsion components with combined EMS relevance, an optimal frequency separation method is offered in [54]. Here in [54], a multi-objective offline optimizer is used to allocate the power separation rules in order to minimize the cumulative weight of sources. However, the proposed offline optimizer is only suitable for a particular driving cycle. In addition, fuel economy and source degradation are not considered during the optimization phase. Another pioneering technique is proposed in [64], where a convexified optimization (CO) framework is formulated to simultaneously reduce energy consumption and ownership price of a PEMFC powered electric bus. However, the optimality in CO framework is scarified and health degradation aspect is not considered within the CO framework. The authors of [55] extended the methodology of [50] to size the FCHEV sources according to desired driving characteristics. To reduce the probability of oversizing, a flexible range is integrated in the sizing procedure. A CO framework is then devised to solve the optimization problem consisting of components cost and energy consumption variables. However, the aspect of health degradation is not considered in the optimization framework. Furthermore, the conceivable effect of proposed flexible range on the operational performance of FCHEV is not extensively studied.

2.2.2.4 Coordinated bi-level sizing for optimal configuration

In comparison to method discussed in Section: 2.2.2.3, this technique essentially consists of two interconnected levels to coordinate the sizing aspect with the EMS of FCHEV. The outer level configures the FCHEV propulsion system, while the inner level includes the EMS variables. Due to the bi-level structure, this technique generally suffers from a higher computing complexity, particularly when the optimization aspect is considered at either or both levels. In [56], a bi-loop framework is proposed, where the outer loop features the optimal FCHEV configuration and the inner loop deals only with the EMS. Nevertheless, optimal solutions are achieved with the challenging computing complexity associated with the offline bi-loop optimizer. To ease the computing burden, the inner loop can be designed using an EMS based on an online optimizer to achieve the operational goals, as depicted in [57]. Here in [57], the inner loop consists of equivalent consumption minimization strategy with an adaptive equivalent factor to facilitate efficiency improvement and charge preservation. The outer loop, on the other hand, is designed using an offline multi-objective optimizer to find the optimum configuration of FCHEV powertrain system. The sizing procedure combined with health degradation aspect is rarely studied. In [58], a bi-loop framework is devised, where the outer loop is composed of sizing variables and inner loop is devoted to EMS of FCHEV. Subsequently, an effective compromise between fuel consumption and source degradation is achieved using a pareto-optimization framework. However, the aspect of ownership price is not explored, and as dynamic programming (DP) is used here, the findings are only valid for a specific driving cycle.

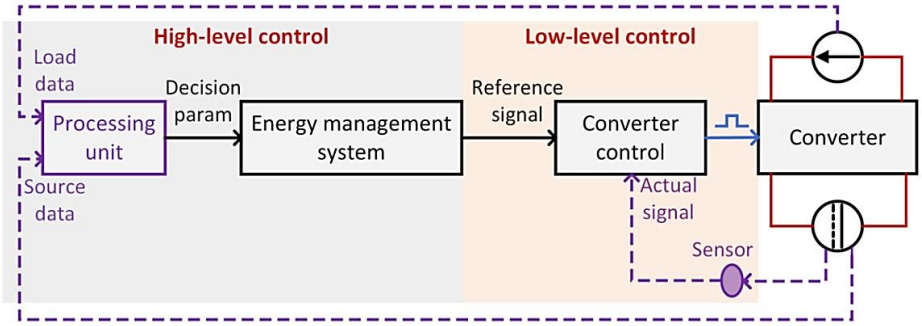

Figure 7: Abstractive control scheme of a commercial-grade FCHEV.

2.3 The control aspects

Due to electrochemical nature of power sources, the performance of FCHEV is extremely susceptible to external operating conditions [65, 66]. This is especially true for hydrogen consumption and degradation of PEMFC stack, which are reliant on the nature of driving conditions such as acceleration, braking, and start-stop [67, 68]. The introduction of decisive improvements in both high-level control (EMS) and low-level control (converter control) is the key to reduce the dependence of FCHEV performance on external operating conditions. The

abstractive layout of control scheme present in a commercial-grade FCHEV is illustrated in Figure 7. Essentially, the overall control system can be divided into two interconnected loops: the outer control loop is referred as the high-level control or energy management system (EMS) [69], and the inner loop is termed low-level control or converter control scheme [70].

2.3.1 Energy management system

The EMS of FCHEV is the core part of 'control design' problem. In essence, EMS deals with the appropriate distribution of available energy sources to ensure that the necessary load demands are entirely satisfied [71, 72]. Unlike stationary hybrid power systems, the FCHEV is exposed to time-variant traction-load with very high intermittency and variability. Furthermore, the PEMFC as main source of FCHEV is extremely fragile and sensitive to operating conditions [73, 74]. Therefore, designing an efficient and real-time EMS for FCHEV is particularly challenging due to its two-dimensional nature. An appropriate trade-off between the degree of optimality and online implementation is required. The degree of optimality is primarily concerned with the relative realization of operational objectives such as hydrogen consumption and lifespan improvement etc. A higher degree of optimality therefore improves the operational performance of FCHEV, but at the cost of greater computational complexity of EMS that may hinder its online implementation. Given its importance, the topic of EMS is rigorously studied in order to improve various operational aspects of FCHEVs. Within the vehicles domain, commonly utilized EMS can be classified as rules-driven strategies (RDS), optimization-driven strategies (ODS), and hybrid strategies [75-78]. A non-exhaustive breakdown of EMS classification is presented in Figure 8. Subsequently, the conclusive summary of these EMS is presented in Table 4.

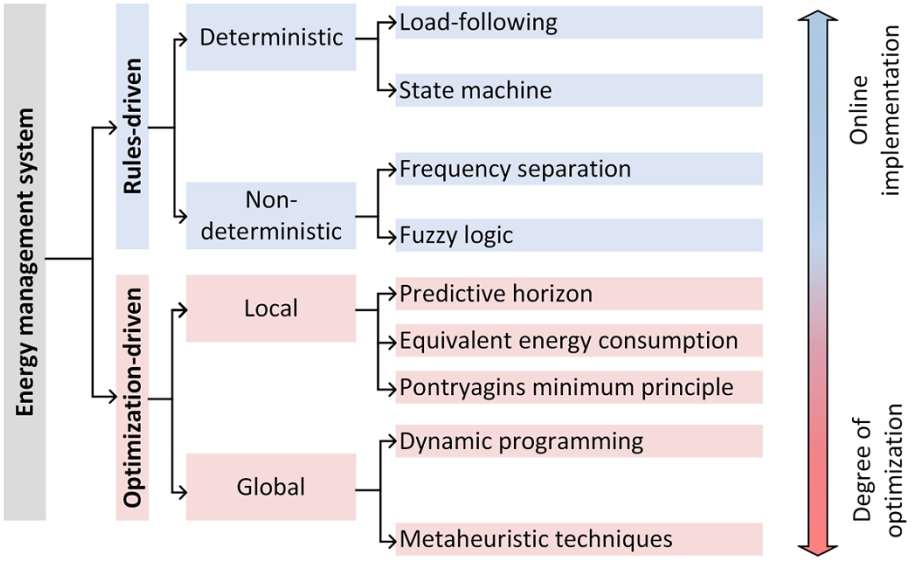

Figure 8: The non-exhaustive breakdown of broadly classified EMS from the literature.

Table 4: The conclusive summary of already established EMS methods.

	EMS methods	Computation complexity	Implementation		Optimization (Minimization)		Realization	
			Online	Offline	Hydrogen consumption	Health degradation	Storage limits	Charge sustain
Rules-driven	Load-following [79, 80]	+	++	×	×	×	×	×
	State machine [30, 36]	++	++	×	×	×	++	×
	Frequency separation [54, 81]	+	++	×	×	+	×	×
	Fuzzy logic [82, 83]	++	+	×	×	+	++	×
Optimization-driven	Predictive horizon [75, 84]	+++	+	×	++	++	+	+
	Equivalent consumption[85, 86]	+++	+	×	++	++	+	+
	Pontryagin's principle [87, 88]	+++	+	×	++	++	+	+
	Dynamic programming [89, 90]	++++	×	✓	+++	+++	++	++
Hybrid	Tuned equivalent energy consumption [83]	+++	+	×	++++	++++	+	++
	Tuned Pontryagin's [88]	+++	+	×	++++	++++	+	++
	Tuned fuzzy logic [91]	++	+	×	++	++	++	×
	Tuned frequency separation method [54]	++	++	×	++	++	×	×
	Mixed rules-driven [92]	++	+	×	+	+	++	×

Legends: '+' indicates the improvement/de-improvement trend.

2.3.1.1 Rules-driven strategies

In rules-driven strategies (RDS), the traction energy is allocated among energy sources of FCHEVs, following a set of pre-established rules. Regardless of the nature of rules, the RDS deliver consistent performance over a broad-range of driving environments and are computationally inexpensive [38]. Therefore, RDS are the most feasible candidate to implement online EMS of FCHEV. Nevertheless, there are two major limitations: difficulty in designing the rules and inadequacy to optimize the key operational objectives such as fuel economy, health degradation, and storage constraints [75]. According to the characteristics of rules, RDS can be further categorized into frequency separation methods (FSMs) [54, 81], fuzzy logic methods [82, 83], and deterministic methods [93, 94].

2.3.1.2 Optimization-driven strategies

The limitations of RDS prompted researchers to leverage optimization-driven strategies (ODS) in order to achieve the main operational goals of FCHEV. An optimization framework, consisting of one or more objective functions bounded by different operational constraints, is typically

employed in the ODS. Dynamic programming, which is an efficient mathematical tool, is often used as a global-ODS to design EMS of FCHEV. The reference [89] formulated a global EMS based on DP to minimize the fuel consumption of FCHEV. Likewise, both sources degradation and fuel consumption of FCHEV are minimized using DP in [90]. Despite the extensive use of DP to formulate optimal EMS of FCHEV, it is reported in the literature that that global-ODS are only appropriate for a specific driving cycle and vehicle routes with high repeatability [95]. The accompanying computing workload is typically blamed for the offline implementation and inconsistent performance of global-ODS across a broad range of driving cycles. Another popular global ODS exploits the convexification of optimization framework to reduce computational complexity for the online implementation. However, the convexification reduces optimality compared to DP. In this context, a convexified framework (CF) is proposed in [96], which simultaneously considers fuel economy and optimal sizing with repeated bus routes. Another application of CF is reported in [97], where a near-optimal online EMS is proposed to enhance the fuel economy of PEMFC based hybrid topology of a heavy duty truck. By utilizing explicit tuning metrics, the local-ODS such as equivalent energy consumption (EEC) [85, 86], pontryagin's minimum principle (PMP) [87] and predictive horizon (PH) [98] can approximate the performance of global-ODS. The favorable features of local-ODS are the simple framework, reduced computational burden, and weak online implementation.

Modern trends in the development of real-time EMS for FCHEVs is focused on the utilization of local-ODS by mitigating their demerits and making them competitive to realize the considered operational objectives. In [83], an adaptive EEC is formulated to design optimal EMS of FCHEV. The objectives under consideration are health degradation, fuel economy, and charge maintenance. The authors pointed out that the equivalent factors of EEC should be tuned properly to attain both fuel economy and charge maintenance when health degradation of sources is accounted for. From [83], it can be endorsed that for a specific driving environment, equivalent factors of EEC must be explicitly tuned to achieve the under consideration objectives, which may leads to re-tuning, when the driving condition is significantly altered. Likewise, the costate factors in PMP should also be appropriately configured to formulate the EMS of FCEHV, subject to the envisioned objectives as reported by [88]. Here, the costate factor is configured to maximize the regenerative power while reducing the hydrogen consumption of FCHEV. In contrast to EEC and PMP, the performance of PH based methods is typically related to selection of computing horizon. The corresponding significance is effectively investigated in [75] for health-aware PH based cost-optimal EMS of FCHEV.

2.3.1.3 Hybrid strategies

The RDS usually favor online application over poor to no optimization. Similarly, the converse is true for ODS, which typically prioritize optimization over online applicability. Hybridizing RDS and ODS can result in a potentially better EMS, with the features of both online/real-time application

and local optimization. In this context, the authors of reference [91] studied a hybrid strategy, where the membership function of fuzzy logic is tuned in an offline manner using GA to reduce fuel consumption of HEV for a given driving cycle. The health degradation aspect is investigated in [83], where prognostic enabled EMS of FCHEV is formulated using data-fusion technique applied over the FL framework. The FL controllers are tuned in an offline manner using GA for various levels of PEMFC's health deterioration. Then, the offline tuned FL controllers are fused together using dempster-shafer principle for a possible online implementation. In [92], wavelet transform based FSM is hybridized with different RDS to achieve the prolonged lifespan of plugin HEV's battery pack, while taking into account the effect of temperature uncertainty. Another effective approach consisting of a novel extremum seeking method (ESM) is formulated in [99] for an online EMS of FCHEV. The ESM methodology is essentially the combination of filters and optimal control which compels PEMFC to operate in a high efficiency region in order to achieve lower fuel consumption.

Besides overall higher ownership price, the comparatively shorter lifespan of PEMFC severely restricts the commercial acceptance of FCHEVs [100]. Therefore, appropriately assessing and quantifying the PEMFC state-of-health is an important aspect with respect to its integration in the real-time EMS. The health of PEMFC is usually linked to its operational conditions, as PEMFC performance parameters, such as power and efficiency, vary with the operating conditions [101-103]. The easiest way to prolong the life of PEMFC stack is to constrain its operation using indirect approaches; such as in [54], the FSM based EMS is proposed to assign the low frequency components of tractive load towards PEMFC stack using a low pass filter. Another pioneering approach to improve the lifespan of PEMFC stack is proposed in [104], where a robust low-level controller based on a higher-order sliding mode is conceived to reduce the chattering phenomenon, thus extending the lifespan of PEMFC stack. However, no physical assessment of PEMFC health degradation is performed in [54, 104] which obstructs the applicability and reliability of indirect approaches in the real-time scenarios. Another creative approach is to use multiple small sized PEMFC stacks instead of one larger one to minimize the related health degradation. Such an approach is conceived in [78], where a set of three small sized PEMFC stacks is coupled with the battery to realize FCHEV powertrain system. The EMS consists of heuristic rules to switch PEMFC stacks based on the power demand, so that each PEMFC stack only operates in a particular region to reduce its health degradation. A similar approach is proposed in [105], where it is reported that this method may results in a higher ownership price compared to conventional method having one large sized PEMFC stack. A physical model-based assessment of health degradation is the most robust way to incorporate the health degradation phenomenon into the EMS of FCHEV, as long as there is a compromise between the complexity of model and the accuracy of assessment [75]. The health deterioration of PEMFC stack is typically associated with the real-time operating conditions such as over/under loading, idling, and frequent start/stops. In reference [100], the semi-empirical assessment framework is proposed to quantify

the health deterioration of PEMFC stack due to dynamic operative conditions. The framework is then integrated in the EEC to reduce both the fuel and degradation costs. Similarly, the degradation process of PEMFC with varying loading conditions is empirically assessed and minimized in [84] using quadratic programming within the PH based EMS. A similar approach is proposed in [75] to mathematically quantify the health degradation of PEMFC stack based on loading conditions in relation to health-conscious predictive EMS of FCHEV.

Concluding the discussion on the state-of-the-art EMS, online implementation with consistent operation and resilience to a variety of driving conditions are the key desirable traits. With this, the rule-based methods are the obvious choice. However, this can lead to an inevitable shortcoming associated with sub-optimal operation in terms of achieving an appropriate trade-off between the relevant operational objectives. These drawbacks therefore encourage the exploitation of hybrid approaches: rules can be adjusted online through local optimizers to retain the original advantages while introducing the perception of optimization with respect to the main operational indicators.

2.3.2 Converter control schemes

The EMS is a high-level controller which ensures that the routine performance of FCHEV remains optimal in terms of fuel consumption, and/or sources degradation. Compared to EMS, the converter control (low-level control) guarantees stability and robustness of vehicle operation [106]. The low-level control enables energy sources of FCHEV to closely follow the reference signals generated by EMS. Several control schemes, ranging from conventional to contemporary ones based on nonlinear models are reported in the literature [107-111].

2.3.2.1 Conventional schemes

Due to their simple and model independent nature, the proportional-integrator (PI) compensators are rigorously used to design low-level control of HEVs [107, 108]. The general control scheme based on PI compensator is exhibited in Figure 9. The operating principle is quite simple: the error between reference source signal (generated by EMS) and measured (controllable) signal is reduced by gains-controlled pole placement method. In correspondence with the error minimization, an appropriate duty-signal is produced by PI compensator, which is then converted into a digital signal by the modulator to feed the associated power converter. Therefore, real-time performance of PI controllers is totally dependent on the selected gains ($K_{p,i}$) [112], and tuning these gains to ensure stable vehicle performance in diverse driving environments is a challenging task.

In pursuit of tuning the gains of PI compensator, several methods are proposed in the literature [113, 114]. The systematic (manual) methods explore the impact of gains on system stability metrics such as risetime, overshoot, and steady-state error [115]. In correspondence, the effect of increasing a certain gain ($K_{p,i}$) independently is presented in Table 5. The manual methods are

however time consuming, therefore not suitable for online implementation especially when the reference signal is aggressively time-variant. Moreover, the gains corresponding to linearized plant models can lead to unavoidable deviations under disturbances and uncertainties. Alternatively, trial-based (heuristic) tuning methods are an attractive option for adjusting the gains of PI compensators, such as the Nichols-Ziegler method [116]. Nevertheless, Nichols-Ziegler's method generally favors overcompensation, which results in aggressive gains and an overall less stable system [117].

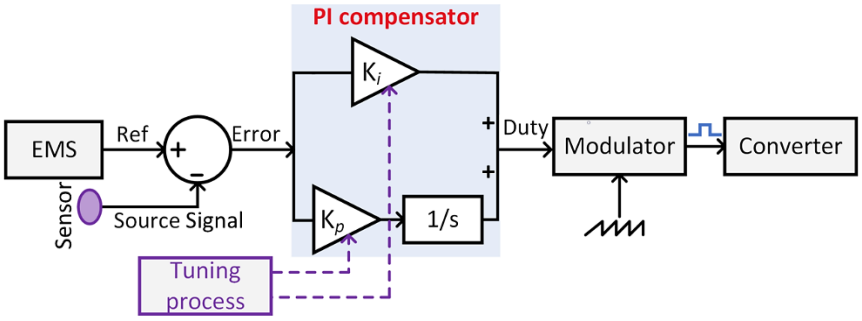

Figure 9: Generalized layout of PI compensators-based conventional control scheme.

The PI controller gains typically chosen by either manual or heuristic methods may not be optimal. Several researchers have addressed this problem by tuning gains using black-box optimization techniques, such as metaheuristics [118]. However, these computationally complex methods are only suitable for offline implementation. However, the offline tuned gains corresponding to different operating scenarios can be linked to FL and neural network-based framework to facilitate online implementation [119, 120].

Table 5: Possible effects of increasing a certain gain independently.

Gain	Stability metric				
	Rise time	Overshoot	Settle time	Steady-state error	Stability
K_p	--	++	+	-	-
K_i	--	+	+++	---	-
Legends: '+/-' indicates improvement/de-improvement trend.					

2.3.2.2 Model-dependent schemes

Compared to model-independent approach of conventional controllers, the predictive controllers typically consider discretized model of power converters [121, 122], as illustrated in Figure 10. The fundamental principle of operation involves predictive calculation of measured states over the complete switching horizon (2^n switching states; n=switches) using a discrete converter model. Then, the cost function is calculated by comparing measured (controllable)

states and reference signals (from the EMS), which allows the least expensive switching state to be selected in real time.

The predictive controller uses an optimization framework with the ability to integrate multiple operating constraints [122], thus providing robust reference tracking. In addition, there are no gains to adjust, making the predictive controller an appropriate option in a time-varying environment with an acceptable level of disturbance and uncertainty. However, the computational complexity associated with associated optimization framework can potentially impact the responsiveness of controller, and aggressive variation of digital duty cycle can degrade the controller itself [123].

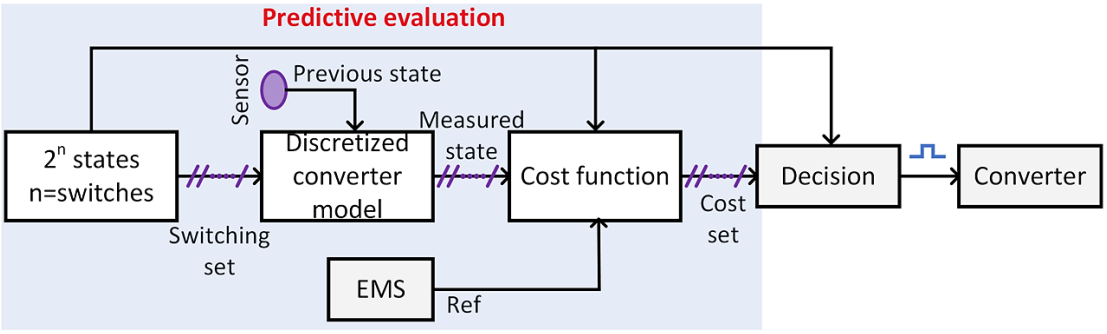

Figure 10: Generalized layout of model-based predictive control scheme.

2.3.2.3 Nonlinear schemes

The nonlinear control schemes are proficient in dealing with real world nonlinear and time-variant systems. Even if the governing system is linear (an ideal or approximated case), the nonlinear controller can facilitate competitive features such as simpler implementation, faster speed, superior accuracy, and reduced controller utilization, which justify a rigorous and mathematically complex design process [124, 125]. Several nonlinear controllers are proposed in the literature to meet specific design requirements. Among all of them, the most popular are nonlinear backstepping [126, 127], higher order sliding mode [109, 128], and passivity approaches [129, 130] with respect to their applications in the vehicle domain. Despite a totally different working philosophy, the nonlinear controllers effectively use Lyapunov theory to extract the control law subject to asymptotic stability of under consideration closed-loop system.

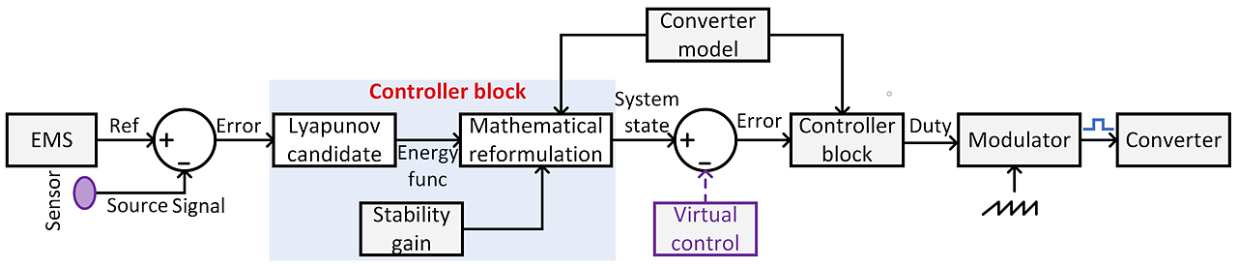

Figure 11: Generalized layout of nonlinear backstepping control scheme.

Figure 11 presents a generalized layout of backstepping based low-level controller. Specifically, a recursive strict-feedback process is exploited, which stabilizes the interconnected local controllers' step by step and consequently derives the local control laws. The process is continued until the global control law is obtained with the necessary stability proof [131]. As exhibited in Figure 11, the process starts with minimizing the error between reference signal (from EMS) and measured (controllable) state using a Lyapunov stabilized controller, which correspondingly manifests residual system state. Then, an appropriate virtual controller is selected based on the derived system state, leading to error minimization using a composite (Lyapunov stabilized) controller. The overall stabilization thus results in a feasible duty cycle, which is then converted to an equivalent digital signal using a modulator and passed to the associated converter. The schemes displayed in Figure 11 is reserved for two-steps only and can easily be extended to n-steps. The convergence rate and overall stability of backstepping control can be improved by adding integral-action, an application is depicted in the references [110, 132].

Chapter 3: The proposed approach for key design aspects

This chapter details the proposed approach to address the key design issues of FCHEV. The process starts with a justified selection of energy sources and their mathematical modeling. Next, the selected sources are arranged in a viable topological structure, which also explores an efficient power connection between the selected sources and the traction load. Finally, a generic methodology is established that exploits the desired vehicle characteristics, the vehicle dimensions, and the notion of design coefficients to size and configure the selected topology.

3.1 Selection and modelling of propulsion components

The design process initiates with an appropriate selection of energy sources based on the nature of HEV. In the case of FCHEV, fuel cell replace ICE as a viable counterpart. The proton exchange membrane fuel cell (PEMFC) is generally preferred for automotive applications thanks to its lightweight, a low operating temperature, and compact size [133]. To assist PEMFC during intermittent acceleration, start-up, and to store energy during braking, either a battery or a supercapacitor or both are hybridized [134, 135]. After an appropriate selection of propulsion sources, their mathematical modeling is carried out with an adequate compromise between accuracy and complexity.

3.1.1 Powertrain approximation

The powertrain or traction system of FCHEV is a complex multi-physics system comprised of an electric motor, a high-power inverter, and transmission circuit. The whole powertrain system can be effectively approximated by a well-documented 'kinematics (glider)' model [28, 136], which is adequate and computationally-simple. The visual perception of various forces acting on a vehicle under the paradigm of this model is illustrated in Figure 12.

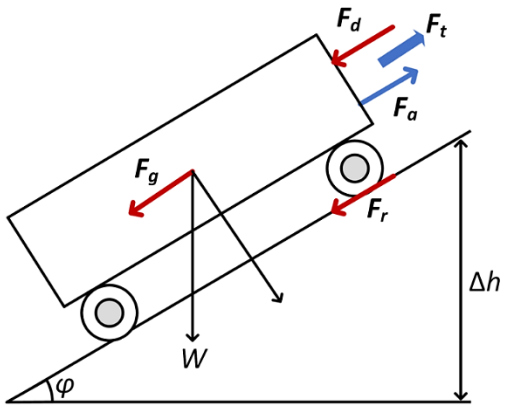

Figure 12: Visual perception of the cumulative forces acting on a vehicle.

The net tractive force (F_t) for a system of forces acting on a vehicle is calculated using (1). Here, F_t is defined as algebraic sum of accelerating force (F_a), drag force (F_d), grading force (F_g), and rolling force (F_r). The mathematical formulation of these components is presented in (1), and their description is provided in Table 6.

$$F_t = F_a + F_d + F_r + F_g$$
$$\begin{cases} F_a = M_v \dfrac{dv}{dt} \\ F_d = \dfrac{1}{2}\rho_a \mathbb{\Gamma}_d S v^2 \\ F_r = Mg\mathbb{\Gamma}_r \cos\varphi \\ F_g = Mg \sin\varphi \end{cases} \quad (1)$$

where, M_v denotes the mass of the studied vehicle. The coefficients $\mathbb{\Gamma}_{\{d,r\}}$ respectively relate to the drag and rolling effect. Finally, the earth's gravitational pull is identified by a constant g. With the knowledge of tractive force (F_t), the equivalent load power (P_d) subject to a particular driving profile signified by speed pattern (v) and slope angle (φ) is calculated by (2), given the information of global operating efficiency of the inverter and motor systems ($\eta_{\{i,m\}}$).

$$P_d = \frac{1}{\eta_i \eta_m} F_t v \quad (2)$$

Table 6: Description of the system of forces acting on a vehicle.

F_t	Total tractive force required to move the vehicle.
F_a	Accelerating force required to overcome the inertial affect.
F_d	Drag force due to aerodynamic resistance of air.
F_g	Grading force required to overcome the slopes of road.
F_r	Frictional load due to movement of tires over the road.

3.1.2 Studied powertrain systems

For illustration purpose, two distinct hypothetical vehicles (light-duty and mid-size passenger) and a commercial-grade vehicle (Toyota Mirai [137]) are respectively studied. The traction parameters of the studied vehicles are presented in Appendix A: Table 27.

Using the 'kinematics' model presented in (1), the maps between desired speed trajectory and demanded power for some of the studied driving cycles are illustrated in Figure 13. Here, Figure 13(a, b) corresponds to the traction power demanded by light-duty (small-size) hypothetical vehicle in the urban/sub-urban driving cycles. The Figure 13c depicts the power required in NEDC cycle by mid-size hypothetical vehicle. Likewise, the power map for commercial-grade passenger vehicle is respectively presented in Figure 13d for Artemis-Motorway cycle.

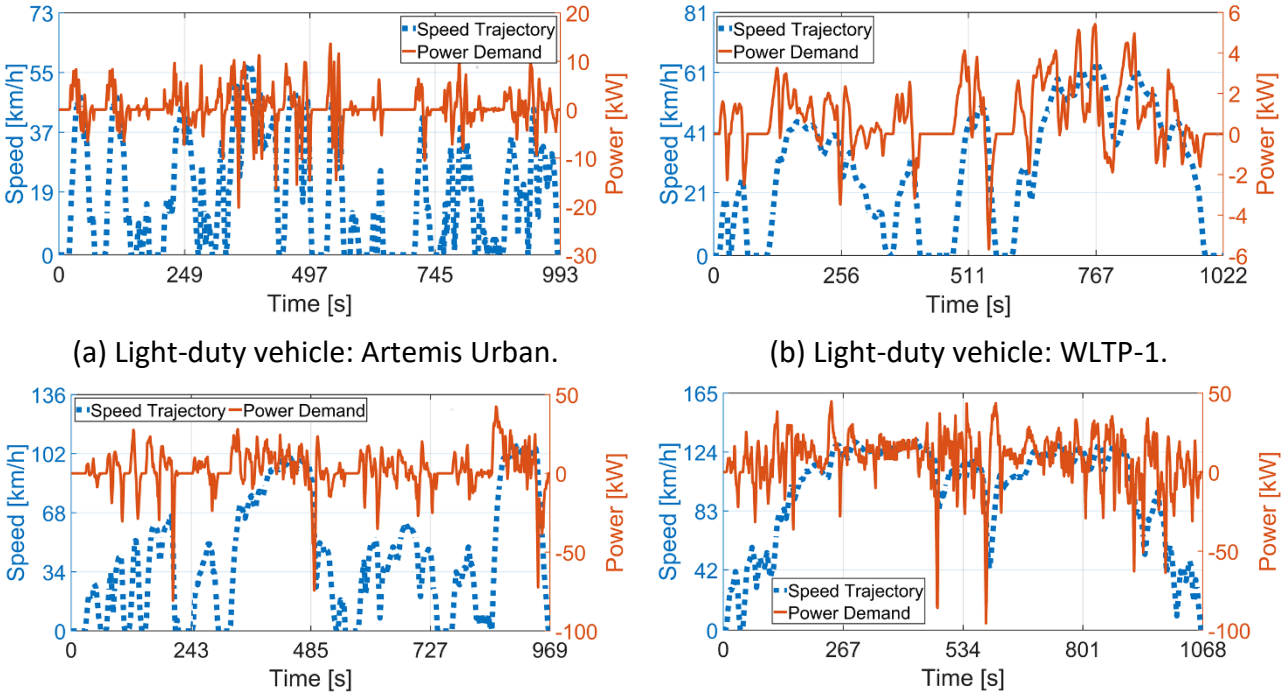

(a) Light-duty vehicle: Artemis Urban.

(b) Light-duty vehicle: WLTP-1.

(c) Mid-size vehicle: LA92.

(d) Commercial vehicle: Artemis Motorway.

Figure 13: Traction power demand and reference speed trajectory for studied driving cycles.

3.1.3 Proton exchange membrane fuel cell

3.1.3.1 Electrical behavior

The PEMFC is an electrochemical energy source which uses relatively clean chemical reaction between hydrogen and oxygen to produce electricity and heat [138]. The heat is either exhausted or recycled to assist the temperature regulator, while electrical energy is available for consumption. Practically, a single cell produces voltage in the vicinity of $1V$. So, a particular number of cells (N_{fc}) are stacked in series to meet the specified need [139]. In this dissertation, a semi-electrical model is utilized to approximate the electrical behavior of PEMFC stack [44, 140]. According to this model, the voltage across PEMFC stack (V_{fc}) relates to current being drawn (A_{fc}) by the relation stated in (3).

$$V_{fc} = E_{fc} - \Omega_{fc} A_{fc} \tag{3}$$

where, Ω_{fc} is the equivalent resistance of stack. The voltage E_{fc} is calculated by using (4).

$$E_{fc} = E_{oc} - E_{act} \tag{4}$$

$$\begin{cases} E_{oc} = K_v \left[E_N + \left(T_{fc} - 298 \right) - \dfrac{44.43}{z_e F} + \dfrac{R T_{fc}}{z_e F} \, ln\left(P_{h_2} \sqrt{P_{o_2}} \right) \right] \\ E_{act} = R_{co} \left[ln\left(\dfrac{A_{fc}}{A_{ex}} \right) \right] \end{cases}$$

where, E_{oc} and E_{act} are respectively open circuit and activation voltages. E_N is the standard notation reserved for Nernest voltage. T_{fc} is the operating temperature in Kelvin (for simplicity, assumed regulated). F and R are Faraday and universal gas constants. z_e signifies the no. of free electrons per chemical reaction. P_{h_2} and P_{o_2} are the partial pressures of reactant gases (assumed regulated). K_v corresponds to constant scaling-factor equivalent to cells in series ($\mathcal{N}_{fc}$). The notation $R_{co} = A_t(1 - e^{-t/\tau_\theta})$ is a time-dependant function, with τ_θ signifying the delay in PEMFC system response due to an air compressor and A_t corresponds to the slope of tafel line. A_{ex} is the exchange current which is constant. Using the model presented in (3)-(4), the polarization relation between V_{fc} and A_{fc} of 6kW PEMFC stack (light-duty hypothetical vehicle) is exhibited in Figure 14b. The same model is used to mimic electrical behavior of 110 kW stack (Figure 14a) present in the commercial vehicle [26, 137, 141], proving its suitability.

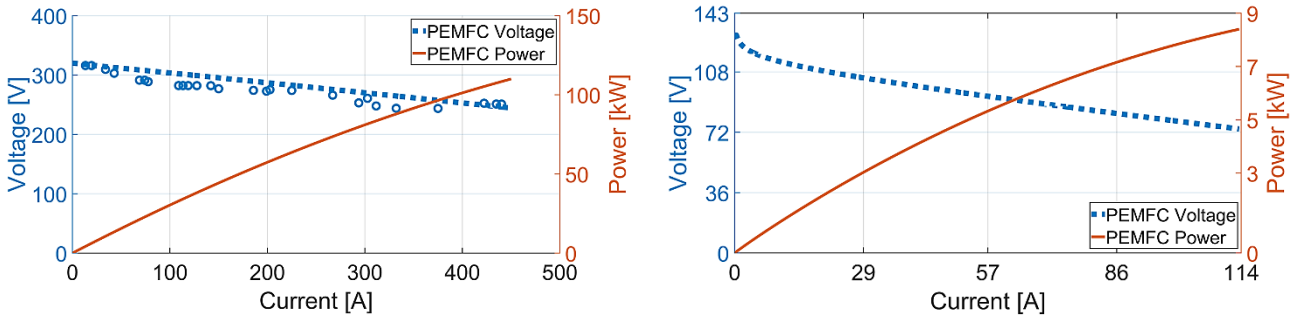

(a) 110kW PEMFC stack of Mirai [137]. (b) 6kW PEMFC stack of hypothetical vehicle.

Figure 14: Polarization relation of studied PEMFC stacks.

3.1.3.2 Efficiency and fuel consumption

The PEMFC system is typically a complicated multi-physics network, which is composed of several auxillary devices and the stack itself as exhibited in Figure 15. Among all, the major auxillary devices include the close-loop cooling circuit, the fuel/exhaust regulation valves, and the boost converter [64, 84].

Due to presence of auxillary devices, the key operational parameters such as efficiency and fuel consumption of the stack and whole system may differ significantly. Therefore, investigating the lumped impact of auxillary devices on key operational parameters of PEMFC system is necessary. In this context, the fuel consumption rate ($\dot{m}_{h_2}$) and operating efficiency of PEMFC system with/without auxillary devices are individually calculated by using (5) and (6) [55, 140]. The data for baseline 6kW PEMFC stack (light-duty hypothetical vehicle) is exhibited in Figure 16b.

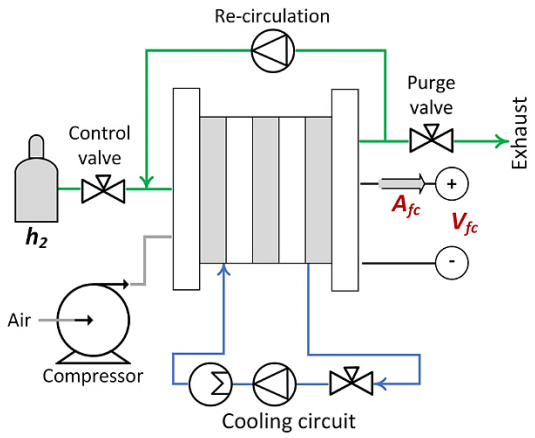

Figure 15: Abstractive layout of the PEMFC system with auxiliary devices.

$$\begin{cases} \eta_{fc} = \dfrac{V_{cell}}{1.482} \\ \dot{m}_{h_2} = \dfrac{N_{fc} A_{fc}}{F} \end{cases} \tag{5}$$

$$\begin{cases} \eta_{fcs} = \dfrac{P_{fcs}}{P_{h_2}} = \dfrac{P_{fc} - P_{aux}}{\delta_{h_2}^{+} \dot{m}_{h_2}{}^{sys}} \\ P_{h_2} = \alpha_0 + \alpha_1 P_{fcs} + \alpha_2 {P_{fcs}}^2 \end{cases} \qquad \left[\alpha_{i=0,1,2} > 0\right] \tag{6}$$

where, η_{fc} and η_{fcs} are the electrical efficiency of PEMFC stack and system. $\delta_{h_2}^{+}$ is the higher heating value of hydrogen. M_{h_2} is the molar mass of hydrogen molecule. V_{cell} is the voltage of a single cell. $P_{\{fc,fcs\}}$ correspond to the power provided by PEMFC stack/system. P_{aux} is the power consumed by auxillary system. P_{h_2} is the equivalent hydrogen power, and $\{\alpha, \gamma\}_{i=0,1,2}$ are PEMFC coefficients. A fitting model similar to (6) is used in (7) to depict the hydrogen consumption of $110kW$ stack (Figure 16a) present in a commercial vehicle [26, 137, 141], proving its adequacy.

$$\dot{m}_{h_2}{}^{sys} = \gamma_0 + \gamma_1 A_{fc} + \gamma_2 {A_{fc}}^2 \qquad \left[\gamma_{i=0,1,2} > 0\right] \tag{7}$$

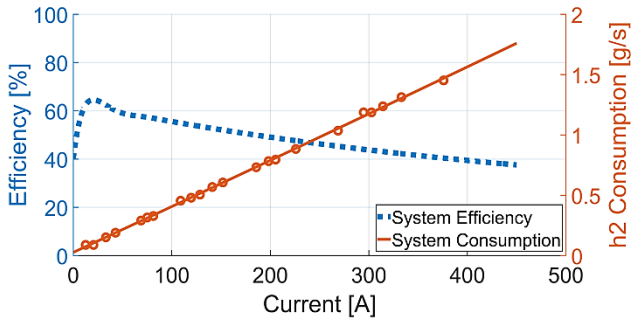

(a) $110kW$ PEMFC system of Mirai [137].

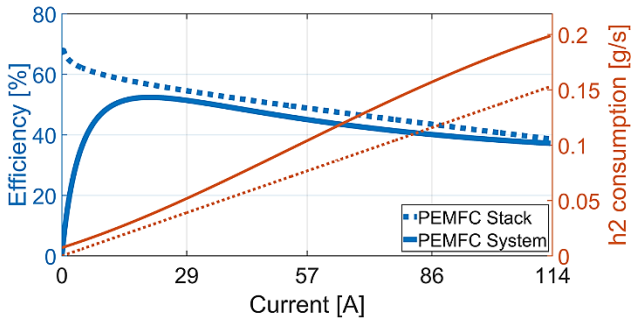

(b) $6kW$ PEMFC system of hypothetical vehicle.

Figure 16: Efficiency and fuel consumption of studied PEMFC systems.

As depicted in Figure 16, both fuel consumption and operational efficiency of studied PEMFC system are fairly dissimlar to that of the stack itself, due to the presence of auxillary devices. The coefficients $\alpha_{i=0,1,2}$ corresponding to studied vehicles are presented in Appendix B: Table 28.

3.1.3.3 Ageing and health-degradation

The limited lifetime of PEMFC compared to existing and mature counterpart ICE is a major technical obstacle in addition to the higher price [142]. In this regard, it is necessary to effectively quantify the aging phenomena under real driving conditions with an adequate trade-off between accuracy and computational burden. Given its importance, this operational aspect is extensively studied in this thesis. In relation to aging and health degradation, the state-of-health (SoH) being an operational indicator can effectively reflect the overall health degradation of PEMFC after the complete driving cycle [143, 144].

The terminology of SoH can be defined in a close relation to depreciation of its key performance parameters. For example, when the electrical power of PEMFC decreases to a certain point, it can be inferred that the end-of-life (EoL) of PEMFC stack is reached or, in other terms, that the SoH is now 0% and PEMFC is no longer usable. Inspired by [105, 145], the depreciation of a certain parameter (z) of PEMFC stack over time ($\Delta t = t_f - t_i$) is approximated by an empirical model presented in (8). In this dissertation, the parameter 'z' denotes the maximum permissible electrical power of the fuel cell stack.

$$\begin{cases} z_f = z_i - \Delta t(\beta_1 {A_{fc}}^2 + \beta_2 A_{fc} + \beta_3) + \Delta t \beta_4 e^{\beta_5 (A_{fc} - A_d)} \\ A_d = A_{fc}^{max}(1 - \beta_6 \Delta t) \end{cases} \quad (8)$$

where, z_f and z_i are respectively the electrical parameters of PEMFC at the end and start of the driving period defined by Δt. $\beta_{x=1,2,..,6} > 0$ are the fitting coefficients (presented in Appendix C: Table 29 for the studied vehicles), and A_d signifies the depreciation of maximum current (A_{fc}^{max}) provided by PEMFC stack. The model presented in (8) is flexible, and easily scalable to different PEMFC stacks by adjusting the fitting coefficients β_x according to experimental or manufacturer data. The expected evolution in the electrical parameters of $6kW$ PEMFC stack (light-duty hypothetical vehicle) at different stages of its life are exhibited in Figure 17a.

The model of (8) approximates depreciation in parameter (z) without taking into account the explicit impact of dynamic loading conditions such as under/over loading, and start-stops, etc. Therefore, it is modified to calculate the depreciation in parameter (z) with the consideration of dynamic loading conditions. In this context, the rationalized health degradation cost denoted by $\mathcal{C}_d$ is introduced in (8) to reflect the impact of over/underloading, load shifting, and frequent start-stops on overall health-degradation. The underlying reason is that the mentioned dynamic loading conditions can accelerate the process of health-degardation, which may result in reaching premature EoL. The modified expression to approximate the level of accelerated

degradation (LAD) symbolized by $\mathcal{C}_d$ is presented in (9). Using (9), the expected evolution of $6kW$ PEMFC stack (light-duty hypothetical vehicle) at MoL, while taking into account the effect of LAD, is illustrated in Figure 17b.

$$z_f = z_i - \Delta t_n(\beta_1 {A_{fc}}^2 + \beta_2 A_{fc} + \beta_3) + \Delta t_n \beta_4 e^{\beta_5 (A_{fc} - A_d)}$$
$$\Delta t_n = \Delta t \left(1 + \sigma_r \frac{1}{\Delta t} \int_{t_i}^{t_f} \mathcal{C}_d(t) dt\right) \tag{9}$$

where, $\mathcal{C}_d$ is the total health degradation cost, and $0 < \sigma_r \leq {\sigma_r}^{max}$ is the weight which dipicts the acceleration in degaradation-process. The SoH can be expressed in terms of depreciation of parameter (z) using (10), provided that the same parameter is already known at beginning-of-life (BoL→z_{BoL}) and EoL (z_{EoL}).

$$SoH_{fc}\% = \left[1 - \frac{z_{BoL} - z_f}{z_{BoL} - z_{EoL}}\right] 100 \tag{10}$$

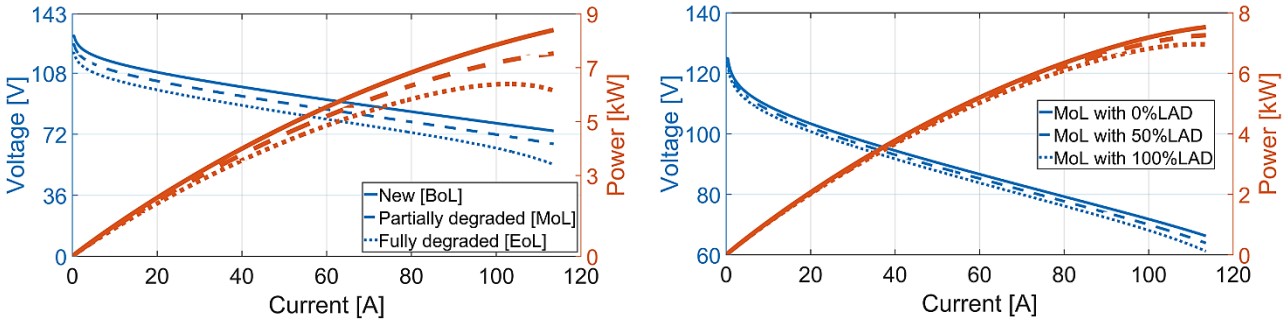

(a) Parameters evolution at different stages. (b) Parameters evolution with LAD%.

Figure 17: Expected evolution in the electrical parameters of $6kW$ PEMFC stack.

For the $110kW$ PEMFC stack of Toyota Mirai [26, 137], an empirical model with comparatively lesser computational complexity is exploited to approximate the expected trend of a certain electrical parameter denoted by z. The implemented model is assumed from the references [58, 84]. Following this model, the expected %decline in the parameter (z) is denoted by $\Delta z\%$, and subsequently calculated by using (11). Here, the parameter 'z' effectively denotes the maximum permissible electrical power of the fuel cell stack.

$$\Delta z\% = k_z(\beta_1 \Delta t_1 + \beta_4 N_s + \beta_2 \Delta t_2 + \beta_3 \Delta t_3 + \beta_5 \Delta t_5) \tag{11}$$

where, β_1 is the loss coefficient corresponding to natural deterioration of parameter (z) over time Δt_1. The parameter decline due to under/over loading specified by violation of limits $A_{\{lo,hi\}}$ over time span $\{\Delta t_2, \Delta t_3\}$ is denoted by $\beta_{\{2,3\}}$. The parameter loss due to number of start-stop cycles (N_s) is defined by β_4. Finally, the load-shifting beyond actual ramping capability (Δ_r) results in parameter loss symbolised by β_5. The description and assumed values of loss coefficients are

respectively presented in Table 7 and Appendix C: Table 29. The values for loss coefficients $\beta_{\{1,2,3,5\}}$ are defined in $\%/hr$, and subsequently coefficient β_4 is described as %/cycle.

Table 7: Power loss coefficients associated with $110kW$ PEMFC system.

Coefficient	Condition for applicability
β_4 [48]	$\left\|\langle A_{fc}(k) == 0\rangle - \langle A_{fc}(k-1) == 0\rangle\right\| > 0$
β_2 [58]	$A_{fc}(k) \leq A_{lo}$
β_3 [84]	$A_{fc}(k) \geq A_{hi}$
β_5 [84]	$\left\|A_{fc}(k) - A_{fc}(k-1)\right\| > \Delta_r$
β_1	$A_{fc}(k) > 0$

The expected SoH of $110kW$ PEMFC stack at the end of driving cycle spanned by Δt_{dc} is calculated by (12), provided that the maximum allowed parameter decline (indicated by $\Delta z_{EoL}\%$) is known. In this thesis, $\Delta z_{EoL}\%$ is set to 10%, which is suitable for vehicular applications as referred in [90].

$$SoH_{fc} \in \mathbb{R} \in [0,1] = \frac{\Delta z_{EoL}\% - \Delta z\%|_{\Delta t_{dc}}}{\Delta z_{EoL}\%} \tag{12}$$

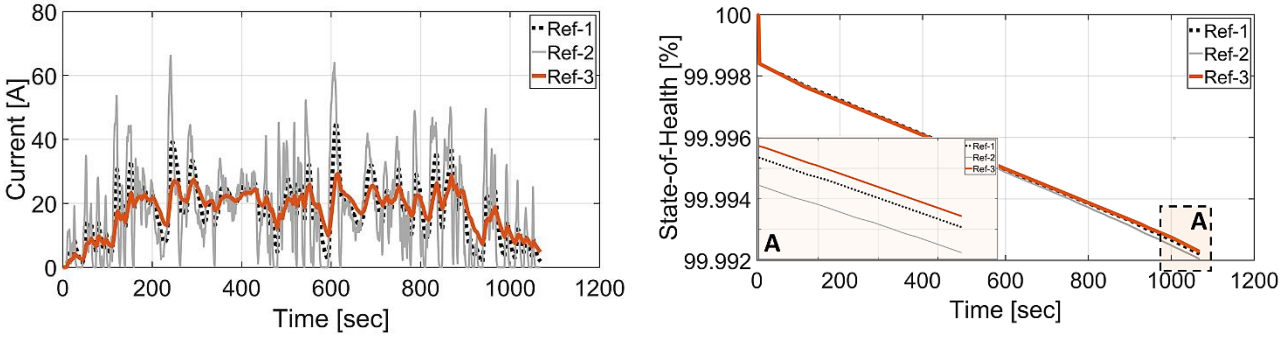

Figure 18: SoH% evolution of 110 kW PEMFC stack in three distinct reference profiles.

Implementation of the degradation model presented in (12) yeilds the SoH evolution of $110kW$ PEMFC stack in three distinct reference profiles (Ref-1→ Ref-3). These profiles are extracted from same driving cycle (Artemis-Motorway), and range from rapid (Ref-2) to comparatively sluggish one (Ref-3), as depicted in Figure 18. It can be observed that SoH% declines in a linear fashion, primarily due to the static loss coefficients, presented in Table 7.

3.1.4 Energy storage devices

3.1.4.1 Electrical behavior

The simplified electrical model of the studied batteries pack is presented in (14), which exploits a predefined relation between the state-of-charge (SoC) and open-circuit voltage (E_b). Typically, this relation is provided by manufacturer for the given battery pack [146, 147]. The SoC of battery

pack is calculated by coulomb-counting method provided in (13), subjected to the condition that initial SoC is already known. Consequently, the relation between the terminal voltage (V_b) and current (A_b) of li-ion batteries pack can be mathematically expressed by (14).

$$SoC_b(t_f) = SoC_b(t_i) - \int_{t_i}^{t_f} \frac{A_b(t)dt}{Q_b} \tag{13}$$

$$V_b = E_b - \Omega_b A_b = f(SoC) - \Omega_b A_b \tag{14}$$

where, Ω_b and Q_b are respectively the equivalent resistance and nominal capacity of the batteries pack. For the considered pack, the relation between V_b and SoC is graphically expressed in Figure 19, when the pack is discharged with the nominal current. The feasible operating range of the batteries pack is appropriately selected, based on this graphical expression, where V_b nearly stays constant as the function of SoC. The selected operating range is effectively bounded by the exponential voltage (V_{exp}) and nominal voltage (V_{nom}) of batteries pack.

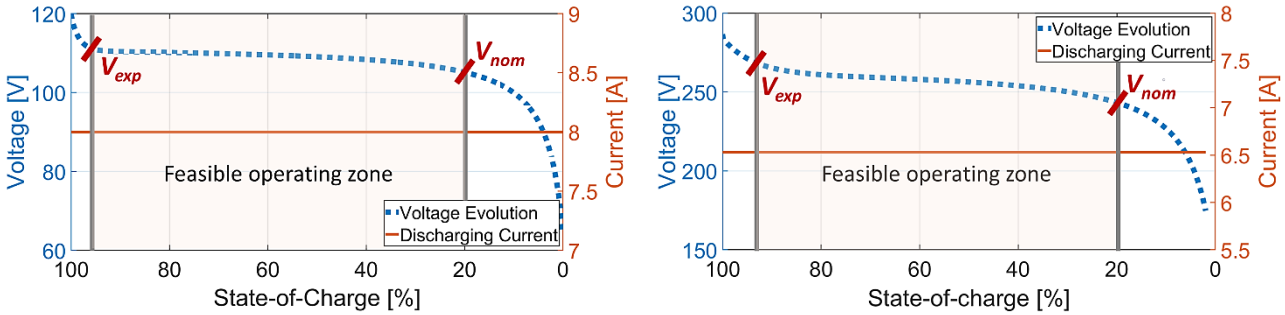

(a) 0.83kWh li-ion batteries pack of hypothetical vehicle.

(b) 1.6kWh Ni-metal-hydride batteries pack of Toyota Mirai [137].

Figure 19: Electrical behavior of the studied batteries pack.

To mathematically model the electrical behaviour of supercapacitors bank, '*Stern*' model is adopted from [148, 149]. Using this model, the supercapacitor voltage (V_{sc}) and its SoC can be expressed as a function of its current (A_{sc}) using (15).

$$\begin{cases} V_{sc} = E_{sc} - \Omega_{sc} A_{sc} \\ E_{sc} = \dfrac{\mathcal{N}_s D_p Q_{\Delta t}}{\mathcal{N}_p \mathcal{N}_t \epsilon \epsilon_o A_d} + \dfrac{2\mathcal{N}_t \mathcal{N}_s R T_{sc}}{F} \sinh^{-1}\left(\dfrac{Q_{\Delta t}}{\mathcal{N}_p \mathcal{N}_t{}^2 A_d \sqrt{8RT_{sc} x_c \epsilon \epsilon_o}}\right) \\ \{Q_{\Delta t}, SoC_{sc}\} = \left\{\int_{t_i}^{t_f} A_{sc}(t)dt\,,\ \dfrac{Q_{sc}{}^{ini} - Q_{\Delta t}}{Q_{sc} V_{sc}}\right\} \end{cases} \tag{15}$$

where, Ω_{sc} is the equivalent resistance of the bank. $\mathcal{N}_t$, $\mathcal{N}_p$ and $\mathcal{N}_s$ are respectively the total number of units in the bank, strings in parallel, and number of units in a string. ϵ_o is the relative

permeability of the insulator. A_d is the area of the plate within the capacitor. Q_{sc} is the total capcitance of bank. D_p is the distance between the plates and ${Q_{sc}}^{ini}$ is the initial charge of bank.

3.1.4.2 Ageing and health-degradation

To approximate the ageing of the studied battery packs subject to a driving cycle defined on Δt_{dc}, an empirical model is adopted from [150]. Similar model is also exploited in [75, 151] to translate the capacity loss into expected remaining SoH of battery pack. Considering that the 20% capacity loss is considered as EoL of battery pack [152], the ageing model is formulated by using (16).

$$\begin{cases} SoH_b(k+1) = SoH_b(k) - \dfrac{|A_b(k)|\delta T_s}{2N_b(c,T_b)Q_b} \\ SoH_b(k+1) \leq SoH_b(k) \end{cases} \tag{16}$$

where, $SoH_b(k+1)$ and $SoH_b(k)$ are respectively the SoH of battery pack at two consecutive samples. δT_s denotes the sample time. The maximum usuable cycles $N_b(c,T_b)$ before reaching EoL (20% capacity loss) is calculated by (17).

$$N_b(c,T_b) = \frac{3600 A_{\Delta t}(c,T_b)}{Q_b} \tag{17}$$

where, $A_{\Delta t}(c,T_b)$ is the total discharged throughput, which is calculated by (18). $M(c)$ is the pre-exponential factor, which depends on the c-rate (c). The factors T_b and z=0.55 are respectively the lumped temperature of battery pack and power-law factor.

$$\begin{cases} A_{\Delta t}(c,T_b) = \left[\dfrac{20}{M(c)e^{f(c,T_b)}}\right]^{1/z} \\ f(c,T_b) = \dfrac{-\Delta E(c)}{RT_b} \end{cases} \tag{18}$$

where, ΔE denotes the activation energy, and R signifies the universal gas constant. Based on the model presented in , the SoH% evolution of 1.6kWh Ni-metal-hydride battery of commercial vehicle [26, 137] is exhibited in Figure 20 for three distinct reference charge/discharge profiles.

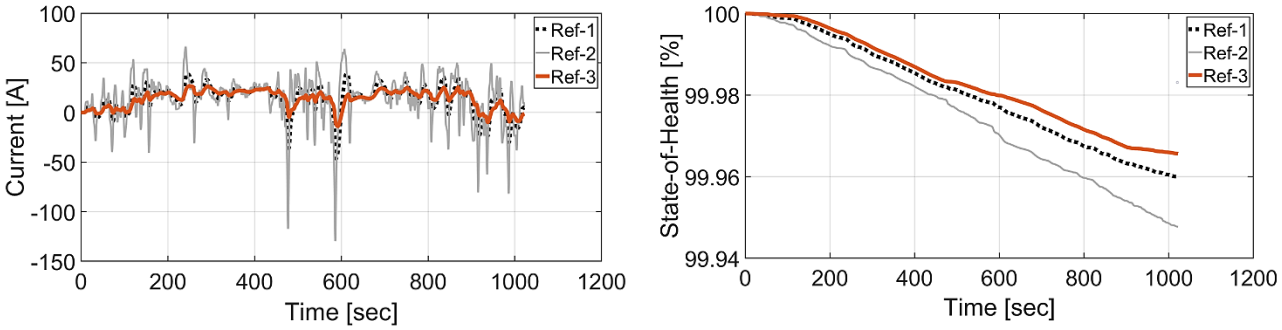

Figure 20: SoH% evolution of 1.6 kWh Ni-metal-hydride battery in three distinct profiles.

It can be observed that the battery degrades comparatively faster in profile Ref-2, which can be mainly associated to charge/discharge at a higher c-rate (typically, '1' c-rate is defined as charging/discharging at the nominal Ah-rate).

3.2 Selection and modelling of topological structure

3.2.1 Layout scheme

The layout scheme is a generic terminology, usually attributed to the arrangement and connection of propulsion components with respect to the DC-link configuration. In this context, two distinct hybrid powertrain topologies are selected and comprehensively studied. First topology (presented in Figure 21) is associated with the studied hypothetical FCHEVs (Appendix A: Table 27). Here, the compressor operation is idealized and is consequently not included in the hybrid system. Another noteworthy point is that the hypothetical hybrid powertrain constitutes three sources: the vision is to provide a balanced configuration in terms of power-energy density and sizing process can be properly exploited to reach an overall lower ownership price. The topology represents an active interface with opportunity to exploit the operational characteristics of sources via optimization based OEMS.

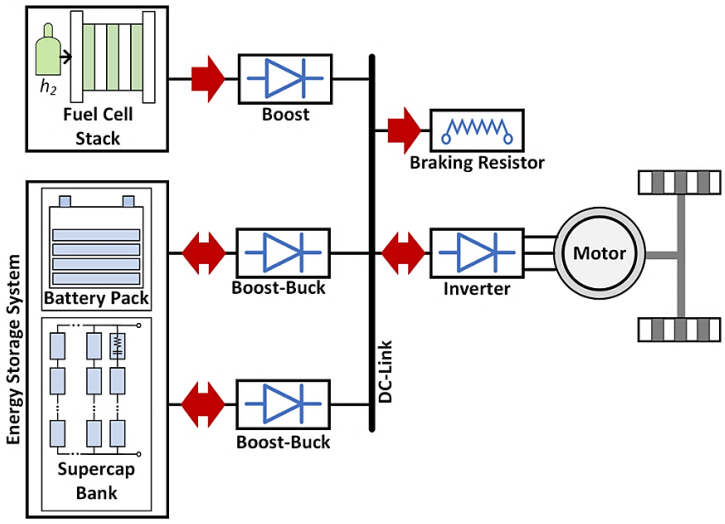

Figure 21: Layout of hybrid powertrain system for the hypothetical vehicles.

Subsequently, the second topology in Figure 22 illustrates an abstractive layout of the hybrid propulsion system of the studied commercial-grade FCHEV with the consideration of an air compressor system [26, 137]. The topology in Figure 22 differs by the presence of a Ni-metal-hydride battery pack as the only ESD, compared to composite ESDs present in the studied hypothetical vehicles (Figure 21). Another difference is about the presence of an air compressor in the hybrid powertrain system of commercial-grade FCHEV. The rest of system is essentially the same except specifications and data, which mainly differ depending on the type of vehicle.

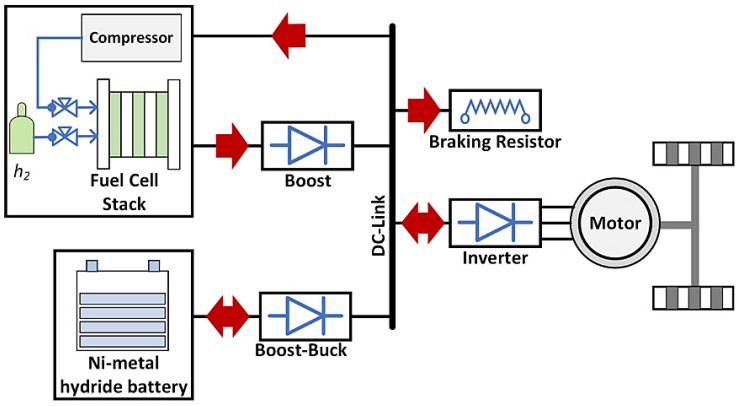

Figure 22: Layout of hybrid powertrain system for the commercial-grade vehicle [137].

3.2.2 Power conditioning stage

The power conditioning stage is one of the most important blocks of FCHEV topology. It serves various purposes such as (*i*) an appropriate way to connect low-voltage electrical sources with the traction motor via DC-link, (*ii*) an effective way to control the energy sources, and (*iii*) maintain stability of the whole system. In practice, the Boost converter is used to couple PEMFC stack with traction motor [153]. Likewise, the ESDs are coupled via dedicated bidirectional Boost-Buck converter [154]. In context, the electrical circuit diagram of the power conditioning stage devoted for FCHEV applications is depicted in Figure 23a [155, 156]. The conventional model is then replaced by an average transformer model in Figure 23b to reduce the complexity but at the acceptable cost of accuracy. The electrical operation of conventional power conversion stage exhibited in Figure 23a can be mathematically described by a set of state equations (19).

$$\begin{cases} \dot{X_{3x1}} = (\tau^{\alpha}_{3x3} + \mathrm{g}_{3x3})X_{3x1} + \tau^{\beta}_{3x3}\lambda_{3x1} \\ Y_{3x1} = \mathrm{I}_{3x3}X_{3x1} \end{cases} \tag{19}$$

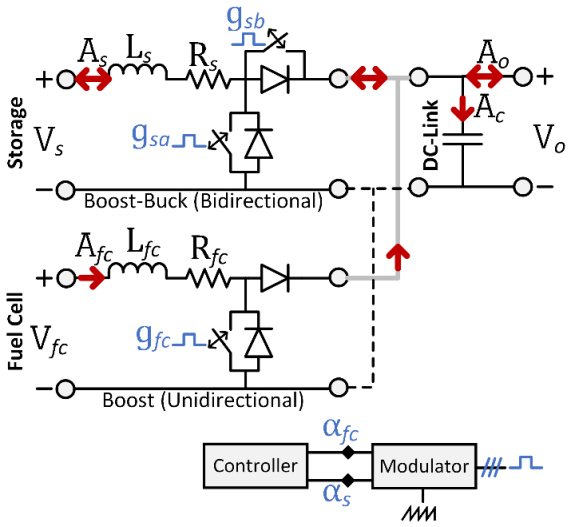

(a) Electrical circuit diagram.

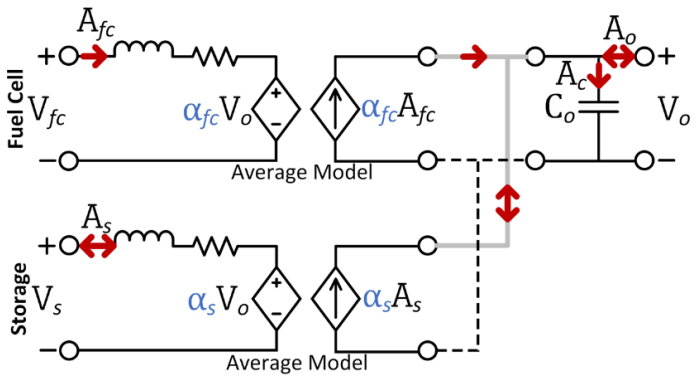

(b) Average electrical (transformer) model.

Figure 23: Schematic of conventional power conversion stage devoted for FCHEVs.

where, $X_{3x1} = [A_{fc} \quad A_s \quad V_o]^T$ identifies the controllable system states. The elements Y_{3x1} and I_{3x3} are the output and identity matrices. $\tau_{3x3}^{\{\alpha,\beta\}}$ and g_{3x3} respectively correspond to the system passive elements and switching signals, which are cumulatively presented in (20). The element λ_{3x1} is the counterpart of state vector X_{3x1}, which equates to $[V_{fc} \quad V_s \quad A_o]^T$.

$$\begin{cases} \tau_{3x3}^{\{\alpha,\beta\}} = \left\{ \begin{bmatrix} -R_{fc}/L_{fc} & 0 & -1/L_{fc} \\ 0 & -R_S/L_S & 0 \\ 1/C_o & 0 & 0 \end{bmatrix}, \begin{bmatrix} 1/L_{fc} & 0 & 0 \\ 0 & 1/L_s & 0 \\ 0 & 0 & -1/C_o \end{bmatrix} \right\} \\ \mathrm{g}_{3x3} = \begin{bmatrix} 0 & 0 & g_{fc}/L_{fc} \\ 0 & 0 & -g_{sab}/L_S \\ -g_{fc}/C_o & g_{sab}/C_o & 0 \end{bmatrix} \end{cases} \tag{20}$$

$$g_{sab} = K_{sw}[1 - g_{sa}] + [1 - K_{sw}]g_{sb}$$

where, g_{sab} represents the overall switching behavior of bi-directional converter associated with the ESD (Figure 23a). The transition between boost-buck (forward-backward) operation is defined by introducing an intermediate switching state K_{sw}, which is '0' in case of boost otherwise '1' for buck operation. The transition is typically triggered in accordance with the polarity of controllable system state, which also serves the purpose of conserving the energetics. The global state-space model of FCHEVs power conversion stage presented in (19) is dependent on the nonlinear switching action defined by $g_{\{fc,s\}}$. This nonlinear behavior can be adequately approximated by an average transformer model (Figure 23b) driven by continuous duty-cycles $\alpha_{\{fc,s\}} \in]0,1[$. This transition is usually governed by employing steady-state conditions: inductor's volt-sec balance and capacitor's charge balance, thereby converting the discrete switching states $g_{\{fc,sab\}}$ to $\alpha_{\{fc,s\}}$, and eliminating the need for a modulator. In theory, the continuous signals $\alpha_{\{fc,s\}}$ can be calculated by the relation (21). However, in practice, these signals are provided by the low-level controller associated with the respective power converters.

$$\begin{cases} \alpha_{fc} \in]0,1[= 1 - V_{fc}/V_o \\ \begin{cases} \alpha_s \in]0,1[= 1 - V_s/V_o & A_s \geq 0 \\ \alpha_s \in]0,1[= V_s/V_o & A_s < 0 \end{cases}, \quad \alpha_{\{fc,s\}} \in \mathbb{R} \end{cases} \tag{21}$$

The electrical efficiency of conventional power stage (Figure 23) is severely reduced at the upper operating range of duty-cycles. To remedy this problem, the interleaving of power conditioning stage is an effective solution [157, 158]. The idea is to split the input-side current in 'n-legs' to decrease the quadratic power losses within the parasitic resistance of input-side inductor, and therefore reduce thermal stress on the power stage along with enhancing the reliability (intrinsic redundancy). This also allows for reduced ripples, which helps to downsize passive components, thus reducing cost and weight. In context, the electrical circuit diagram and equivalent average (transformer) model of a typical interleave power stage are presented in Figure 24. Subsequently, the state-space model of 'n-legs' interleave power stage is provided in (22).

$$\begin{cases} \dot{X_{nx1}} = (\tau_{nxn}^{\alpha} + \mathrm{g}_{nxn}) X_{nx1} + \tau_{nxn}^{\beta} \lambda_{nx1} \\ \Upsilon_{nx1} = \mathrm{I}_{nxn} X_{nx1} \end{cases} \tag{22}$$

where, $X_{nx1} = [A_{fc1}\ A_{fc2}\ \cdots\ A_{fcn}\ A_{s1}\ A_{s2}\ \cdots\ A_{sn}\ V_o]^T$ identifies the controllable system states. The elements Υ_{nx1} and I_{nxn} are the output and identity matrices. $\tau_{nxn}^{\{\alpha,\beta\}}$ and g_{nxn} respectively correspond to passive elements and switching sequences, which can be determined by expanding (20) over 'n' legs. The element λ_{nx1} is the counterpart of state vector X_{nx1}, which effectively equates to $[V_{fc}\ V_{fc}\ \cdots\ V_{fc}\ V_s\ V_s\ \cdots\ V_s\ A_o]^T$.

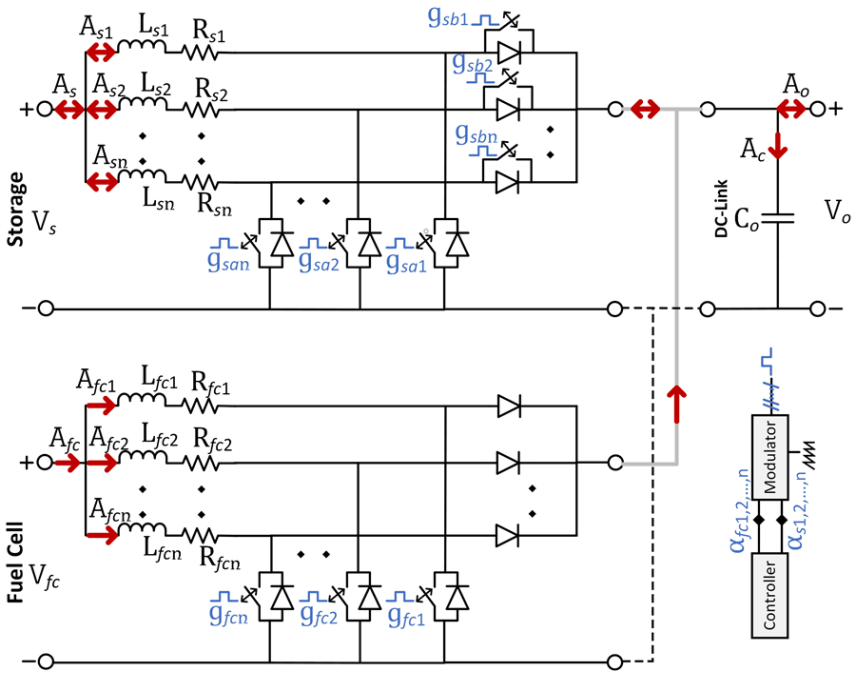

(a) Electrical circuit diagram.

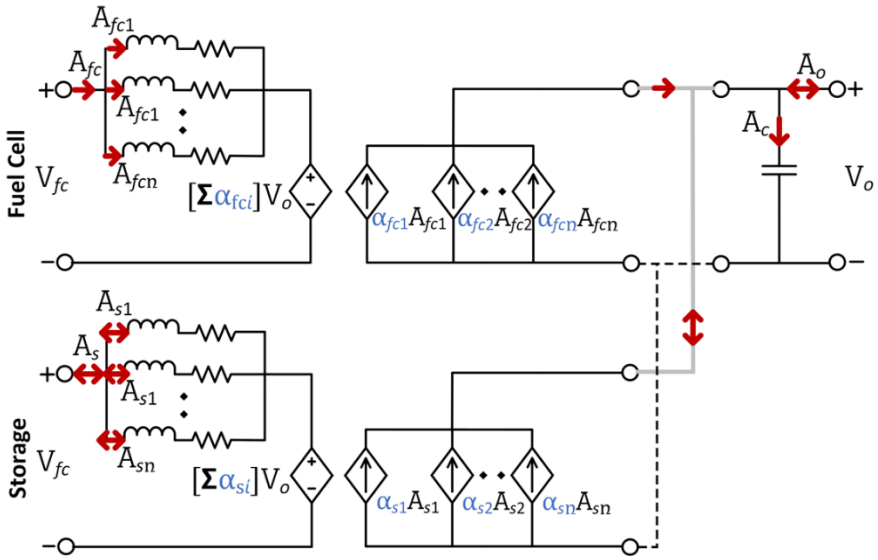

(b) Average electrical model.

Figure 24: Schematic of interleave power conversion stage devoted for FCHEVs.

3.3 Design coefficients based systematic sizing

A novel approach is proposed to size and configure the powertrain elements of FCHEV at system design level. The approach is generic and easily applicable to a range of hybrid vehicles with different profiles with minimal computational burden. The method initially exploits the specific traction parameters (Appendix A: Table 27), and the desired vehicular response (acceleration and top speed, etc.) to facilitate base propulsion configuration [50, 55]. The base configuration is expected to perform reliably in diverse driving conditions at the expense of oversized sources, which may increase the ownership price of FCHEV. To reduce the likelihood of oversizing, an innovative concept of design coefficients is integrated in the sizing procedure to produce a flexible but realistic sizing range. From the flexible sizing range, a unique/optimal configuration is selected by coordinating the sizing procedure with the EMS of FCHEV. The results of coordination step are effectively presented in Chapter 5. The schematic of the proposed sizing procedure is illustrated in Figure 25.

where, in Figure 25, V_x, P_x and Δ_x are respectively the voltage, power, and design coefficients associated with x^{th} powertrain component. The coefficients associated with the energy sources (Δ_{fc} for PEMFC stack and Δ_{doh} for hybrid energy storage) are flexible, as they have a direct impact on overall price of the system. Moreover, operational parameters of FCHEV, such as its fuel economy and health degradation of sources, are also influenced by these design coefficients. The rest of design coefficients are selected at system design level and are considered static thereafter for simplicity. For illustration purpose, the sizing process is executed for two distinct hypothetical vehicles (Figure 26).

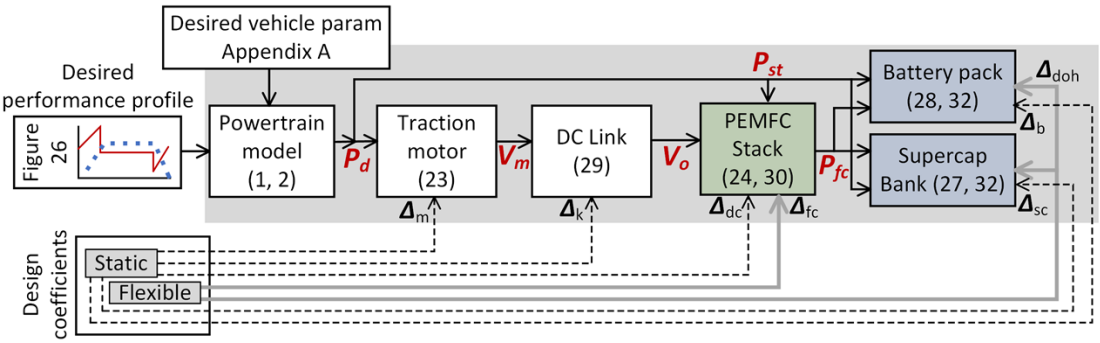

Figure 25: Schematic of the flexible design coefficients based systematic sizing.

3.3.1 Base drivetrain configuration

The base sizing process facilitates global powertrain configuration starting from traction elements such as electric motor and DC link to sources such as PEMFC and ESDs. The base configuration is expected to provide reliable performance, but at the expense of oversizing.

3.3.1.1 Traction motor

The primary purpose of traction motor is to provide the necessary propulsive force for required driving actions. In this paper, the traction motor is sized according to the requested traction power (or provided during regenerative braking) based on the desired driving parameters/profiles shown in Figure 26. These driving profiles are essentially composed of desired vehicular characteristics (notations are depicted in Table 8), such as acceleration/braking parameters, and maximum speeding limit. According to desired driving criteria/profile, the motor is configured mathematically by using (23). Unlike literature [50, 55], deceleration/braking characteristics are equally exploited to effectively size the motor. This feature enables maximum extraction of regenerative energy to enhance the operational efficiency of FCHEV [81, 159].

$$P_m^{max} = \max \langle P_d^+, \Delta_m |P_d^-|, P_{st}^+ \rangle \tag{23}$$

where, in (23), P_d^+, P_d^- and P_{st}^+ respectively signify the maximum power required/provided by traction system during acceleration, braking, and sustained cruising. Δ_m is the design coefficient to reflect the amount of regenerative energy provided by traction motor during deceleration and braking.

Table 8: Notations for the desired response of studied vehicles.

Desired response/characteristic	Corresponding power
Acceleration: $(0 - v_{max})$ in $t_{0-v_{max}}$	Max requested: P_d^+
Braking: $(v_{max} - 0)$ in $t_{v_{max}-0}$	Max regenerative: P_d^-
Sustained cruising at v_{max} for t_{st}	Sustained requested: P_{st}^+

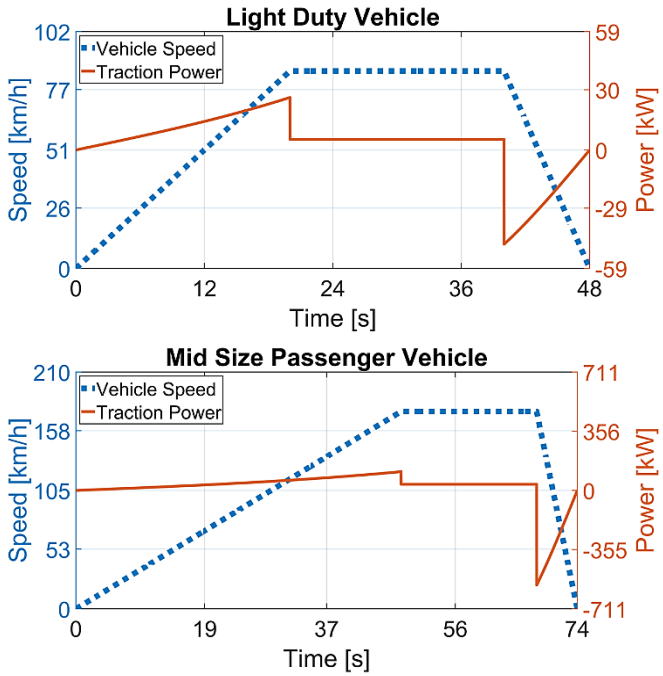

$t_{0-v_{max}}$	$t_{v_{max}-0}$	t_{st}	v_{max}
Hypothetical: light-duty vehicle.			
20 $sec.$	08 $sec.$	20 $sec.$	85 km/h
Hypothetical: mid-size passenger.			
48 $sec.$	06 $sec.$	20 $sec.$	175 km/h

Figure 26: Desired driving parameters/profile of studied vehicles.

It can be observed from Figure 26 that the maximum regenerative power provided by motor (P_d^-) can exceed maximum power requested by motor during acceleration (P_d^+). In the dissertation, Δ_m is configured at system design level, such that only 20% of the maximum regenerative energy is accessible. Through using Δ_m, the electric motor can be sized to provide more than 20% of the available regenerative energy, which will undoubtedly increase the operating efficiency; however, at the cost of increased price of regenerative circuit. It was observed that regenerative energy can be higher than the required power. Realistically, trapping this much power would only be possible with excessively large regenerative circuit. So, the prescribed value provides an adequate circuit, considering the economics and capability of ESDs.

3.3.1.2 PEMFC stack

After sizing the traction motor, next step is to adequately size the energy sources of FCHEV. For this purpose, the PEMFC, which is the primary source, is nominally sized according to (24), so that it provides a sustained cruising capability without any external assistance from the ESDs.

$$\Delta_{fc} P_{st}^{+} \leq {P_{fc}}^{nom} \leq P_{st}^{+} \qquad \{\Delta_{fc}^{-} \leq \Delta_{fc} \leq \Delta_{fc}^{+}\} \tag{24}$$

where, Δ_{fc} is the flexible design coefficient to appropriately size PEMFC stack with the compromise between its price and energy delivered to cruise at a higher speed. Selecting Δ_{fc} closer to upper limit (Δ_{fc}^{+}) ensures that there is enough energy to cruise at a higher speed; however, the price of stack also increases. Similarly, choosing Δ_{fc} near to lower limit (Δ_{fc}^{-}) has

the inverse effect. Therefore, appropriate selection of Δ_{fc} not only affects the expected manufacturing price of FCHEV, but also the fuel consumption and degradation of PEMFC stack.

3.3.1.3 Hybrid energy storage

The systematic and precise sizing of ESDs is mainly based on two factors: The energy required by traction motor during acceleration/sustained cruise, and the regenerative energy supplied by traction motor during deceleration/braking. The maximum residual energy required/provided by traction system is effectively calculated by (25) with the participation of PEMFC stack.

$$E_{res}^{Wh} = \max\langle E_d^+, \left|E_d^+ - {E_{fc}}^+\right|, |E_d^-|, \left|E_d^- - {E_{fc}}^-\right| \rangle$$
$$\begin{cases} {E_d}^+ = \int_{t=0}^{t_{0-\nu max}} \dfrac{P_d^+}{t_{0-\nu max}}\, t\, dt \\ {E_d}^- = \int_{t=0}^{t_{\nu max-0}} \dfrac{P_d^-}{t_{\nu max-0}}\, t\, dt \\ {E_{fc}}^+ = \int_{t=0}^{t_{0-\nu max}} P_{fc}\, dt \\ {E_{fc}}^- = \int_{t=0}^{t_{\nu max-0}} P_{fc}\, dt \end{cases} \tag{25}$$

where, E_{res}^{Wh} is the maximum residual energy, which is either requested or supplied by traction motor, taking into consideration the participation of PEMFC stack. The peak energy is respectively denoted by E_d^+ and E_d^- corresponding to traction power supplied or absorbed by motor. The maximum residual energy calculated in (25) is distributed between ESDs by employing a specific flexible design coefficient Δ_{doh}, as illustrated in (26). Where, Δ_{doh} represents the relative 'degree of hybridization' and facilitates a suitable sharing of residual traction energy (E_{res}^{Wh}) within ESDs. It can be observed that Δ_{doh} has a direct impact both on the size and price of ESDs.

$$\begin{cases} {E_b}^{Wh} = \Delta_{doh} E_{res}^{Wh} \\ {E_{sc}}^{Wh} = (1 - \Delta_{doh}) E_{res}^{Wh} \end{cases} \qquad \{\Delta_{doh}^- \le \Delta_{doh} \le \Delta_{doh}^+\} \tag{26}$$

where, ${E_b}^{Wh}$ and ${E_{sc}}^{Wh}$ individually denote the required energy ratings of batteries pack and supercapacitors bank in Wh. Based on the notion that contraction/dilation of energy stored in supercapacitors bank is proportional to square of voltage across it, a dilation factor λ_{sc} is introduced in (27), so that the peak variation in supercapacitor's voltage is limited to 20% of rated value [50]. Accordingly, the size of whole supercapacitors bank is calculated by using (27).

$$\begin{cases} {E_{sc}}^{bank} = {E_{sc}}^{Wh} / \eta_{sc} \lambda_{sc} \\ Q_{sc}^{bank} = \dfrac{2\sigma_J {E_{sc}}^{bank}}{{V_{sc_{rat}}}^2} \\ \dfrac{\mathcal{N}_{sc}^p}{\mathcal{N}_{sc}^s} = \dfrac{Q_{sc}^{bank}}{Q_{sc}} \end{cases} \tag{27}$$

where, η_{sc} is the average efficiency of supercapacitor bank. ${E_{sc}}^{bank}$ and Q_{sc}^{bank} are individually the capacity of bank in Wh and $Farad$. $V_{sc_{rat}}$ is the rated voltage of bank, and σ_J is the conversion factor to transform energy from Wh to $joule$. The exact configuration of supercapacitors bank (Figure 27a) can now be interpreted using (27). Where, $\mathcal{N}_{sc}^{s}$ signifies the total number of units connected in series (a string) to provide $V_{sc_{rat}}$, and $\mathcal{N}_{sc}^{p}$ is the number of strings connected in parallel to provide the required Q_{sc}^{bank}, subject to the fact that capacity of one unit Q_{sc} is already known.

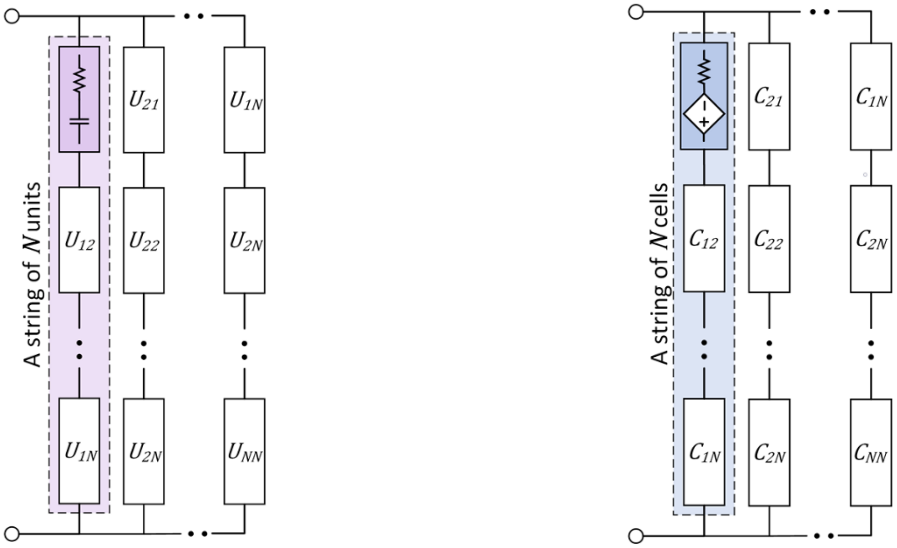

(a) Supercapacitors bank. (b) Batteries pack.

Figure 27: Schematic of the exact configuration of energy storage devices.

Likewise, the batteries pack can be precisely configured by (28), as presented in Figure 27b. where, in (28), $\mathcal{N}_b^p$ and $\mathcal{N}_b^s$ are respectively the total strings in parallel and number of cells in a string. ${V_b}^{nom}$ is the nominal voltage of battery pack. ${V_{cell}}^{b}$ and Ah_{cell} are individually the voltage and nominal capacity of a single cell. λ_{DoD} incorporates the effect of 'depth of discharge' within the sizing procedure, and λ_b limits the percentile variation in the SoC of the battery pack.

$$\begin{cases} {E_b}^{pack} = {E_b}^{Wh}/\eta_b\lambda_b\lambda_{DoD} \\ \mathcal{N}_b^p = \dfrac{{E_b}^{pack}}{{V_b}^{nom}Ah_{cell}} \\ \mathcal{N}_b^s = \dfrac{{V_b}^{nom}}{{V_{cell}}^{b}} \end{cases} \tag{28}$$

3.3.1.4 DC link

The DC link's target voltage is decided according to the range presented in (29), while adjusting the design coefficient (Δ_k). The objective is to decrease the stress on traction system consisting

of a high-power inverter and a traction motor. This would result in the reduced cost of inverter alongside enhancing its performance. However, selecting the DC link's reference solely from the perspective of inverter system is not as adequate as it can increase the price of DC bus capacitor itself. In this dissertation, Δ_k is selected at the system design level in a way to depict a reasonable compromise among performance, stability, and price. Afterwards, the exact configuration of PEMFC stack, i.e. the number of total cells in series ($\mathcal{N}_{fc}$), is evaluated based on the selected DC link's reference while taking into consideration the PEMFC converter's operating range using (30) and (31).

$$\Delta_k V_m^{rat} \leq {V_o}^{ref} \leq V_m^{rat} \tag{29}$$

$$\begin{cases} \Delta_{dc} {V_o}^{ref} \leq {V_{fc}}^{max} < {V_o}^{ref} \\ \mathcal{N}_{fc} \triangleq {V_{fc}}^{max} / {V_{cell}}^{fc} \end{cases} \tag{30}$$

$$\Delta_o{}^{-} {V_o}^{ref} \leq V_o \leq \Delta_o{}^{+} {V_o}^{ref} \tag{31}$$

where, V_m^{rat} is the rated voltage of traction motor. ${V_o}^{ref}$ denotes the reference trajectory for DC link capacitor. ${V_{fc}}^{max}$ is the voltage of PEMFC stack at no load condition. $\mathcal{N}_{fc}$ signifies the total number of cells in the stack. The parameter ${V_{cell}}^{fc}$ denotes the maximum voltage of one cell. Analogous to the relation between DC link's reference and the exact configuration of PEMFC stack, the relation to find exact configuration of ESDs is stated in (32).

$$\begin{cases} \Delta_{sc} {V_o}^{ref} \leq V_{sc_{rat}} < {V_o}^{ref} \\ \Delta_b {V_o}^{ref} \leq {V_b}^{nom} < {V_o}^{ref} \end{cases} \tag{32}$$

where, Δ_{sc} and Δ_b are respectively the static design coefficients associated with supercapacitors bank and batteries pack. It can be observed from (32) that configuring $V_{sc_{rat}}$ and ${V_b}^{nom}$ in the vicinity of ${V_o}^{ref}$ using Δ_{sc} and Δ_b results in extended operational range of bidirectional converters associated with ESDs, but at the cost increased components price.

3.3.1.5 The base configuration

By using the generic sizing procedure exhibited in (23)-(32), the base configuration of studied hypothetical vehicles corresponding to the upper range of flexile design coefficients (Δ_{doh}^{+}, Δ_{fc}^{+}) is presented in Table 9. The base configuration is expected to provide consistent performance but at the cost of oversized components. The value of design coefficients assumed in this dissertation are provided in Appendix D: Table 30. In contrast to the base configuration of hypothetical vehicles which are deduced from the sizing procedure, the base configuration of commercial-grade vehicle is adopted from the references [137].

Table 9: The base configuration of the studied hypothetical vehicles.

Component	No of cells/units		Capacity	Voltage $[V]$
	Series	Parallel		
Hypothetical: light-duty vehicle.				
PEMFC	$\mathcal{N}_{fc}$ =130	×	${P_{fc}}^{nom}$ =6kW	${V_{cell}}^{fc}$*$\mathcal{N}_{fc}$
Battery pack	$\mathcal{N}_b^s$ =28	$\mathcal{N}_b^p$ =4	${E_b}^{pack}$ ≅0.828kWh	${V_b}^{nom}$ =103.6
Supercap bank	$\mathcal{N}_{sc}^s$ =44	$\mathcal{N}_{sc}^p$ =1	Q_{sc}^{bank} ≅ 68.18F	$V_{sc_{rat}}$ =132
Motor/DC Link	×	×	P_m^{max} =27kW	${V_o}^{ref}$ =200
Hypothetical: mid-size passenger vehicle.				
PEMFC	$\mathcal{N}_{fc}$ =423	×	${P_{fc}}^{nom}$ =36kW	${V_{cell}}^{fc}$*$\mathcal{N}_{fc}$
Battery pack	$\mathcal{N}_b^s$ =88	$\mathcal{N}_b^p$ =10	${E_b}^{pack}$ ≅6.51kWh	${V_b}^{nom}$ =325.6
Supercap bank	$\mathcal{N}_{sc}^s$ =141	$\mathcal{N}_{sc}^p$ =1	Q_{sc}^{bank} ≅ 21.28F	$V_{sc_{rat}}$ =423
Motor/DC Link	×	×	P_m^{max} =113kW	${V_o}^{ref}$ =650

3.3.2 Flexible sizing range

In contrast to the base configuration, the flexible sizing range of energy sources corresponds to the complete horizon of design coefficients (Δ_{fc}, Δ_{doh}), effectively bounded by their upper/lower limits ($\Delta_{fc}^{\mp}$, $\Delta_{doh}^{\mp}$). The flexible sizing range for the studied hypothetical vehicles is exhaustively presented in Table 10. The design coefficients with adjustable range can reduce the probability of oversizing sources, while retaining reliability. From the available sizing range, an optimal configuration can then be selected by coordinating the sizing procedure with the OEMS of FCHEV. Moreover, an explicit relation is derived to express the impact of flexible design coefficients (Δ_{fc} and Δ_{doh}) on the expected price of sources. From (33), the overall price of PEMFC system (${\mathcal{C}_{fc}}^{sys}$) can be approximately expressed as a linear function of its design coefficient Δ_{fc}. Likewise, the price of ESD ($\mathcal{C}_{esd}$) can be expressed as a function of design coefficient Δ_{doh}.

$$\begin{cases} {\mathcal{C}_{fc}}^{sys} = \mathcal{C}_{fc} + \mathcal{C}_{t0} + \mathcal{C}_{h_2} = \Delta_{€,fc}{P_{fc}}^{nom} + \mathcal{C}_{t0} + \Delta_{€,h_2}\mathrm{W}_{h_2} = f(\Delta_{fc}) + \mathcal{C}_{fix} \\ \mathcal{C}_{esd} = \mathcal{C}_{sc} + \mathcal{C}_b = {\mathcal{C}_{sc}}^{u}\mathcal{N}_{sc}^p\mathcal{N}_{sc}^s + {\mathcal{C}_b}^{cell}\mathcal{N}_b^p\mathcal{N}_b^s = f(\Delta_{doh}) \end{cases} \quad (33)$$

where, $\mathcal{C}_{fc}$ and $\mathcal{C}_{fix}$ are the baseline prices of both stack and storage tank with hydrogen stored in it ($\mathcal{C}_{t0} + \mathcal{C}_{h_2}$). The coefficients $\Delta_{€,fc}$ (€/W) and $\Delta_{€,h_2}$ (€/kg) are respectively the price conversion factors [64, 75, 160].

Table 10: The flexible sizing range for the studied hypothetical vehicles.

Component	No of cells/units		Capacity	Voltage $[V]$
	Series	Parallel		
Hypothetical: small-size (light-duty) vehicle.				
PEMFC	$\mathcal{N}_{fc}$ =130	×	$4.5 \leq {P_{fc}}^{nom}[kW] \leq 6$	${V_{cell}}^{fc} * \mathcal{N}_{fc}$
Battery pack	$\mathcal{N}_b^s$ =28	$3 \leq \mathcal{N}_b^p \leq 4$	$0.621 \leq {E_b}^{pack}[kW] \leq 0.828$	${V_b}^{nom}$ =103.6
Supercap bank	$\mathcal{N}_{sc}^s$ =44	$\mathcal{N}_{sc}^p$ =1	$Q_{sc}^{bank} \cong 68.18F$	$V_{sc_{rat}}$ =132
Motor/DC Link	×	×	P_m^{max} =27kW	${V_o}^{ref}$ =200
Hypothetical: mid-size passenger vehicle.				
PEMFC	$\mathcal{N}_{fc}$ =423	×	$27 \leq {P_{fc}}^{nom}[kW] \leq 36$	${V_{cell}}^{fc} * \mathcal{N}_{fc}$
Battery pack	$\mathcal{N}_b^s$ =88	$7 \leq \mathcal{N}_b^p \leq 10$	$4.56 \leq {E_b}^{pack}[kW] \leq 6.51$	${V_b}^{nom}$ =325.6
Supercap bank	$\mathcal{N}_{sc}^s$ =141	$1 \leq \mathcal{N}_{sc}^p \leq 2$	$21.28 \leq Q_{sc}^{bank}[F] \leq 42.52$	$V_{sc_{rat}}$ =423
Motor/DC Link	×	×	P_m^{max} =113kW	${V_o}^{ref}$ =650

Chapter 4: The proposed approach for key control aspects

This chapter presents the proposed approach for the key control aspects of studied FCHEVs. The background and working philosophy of the proposed OEMS based on frequency separation method are presented alongside developed converter control schemes. The detailed mathematical formulation including the optimization and decision frameworks are jointly laid out for the proposed high/low level control schemes of the studied FCHEVs.

4.1 High-level control: Online EMS based on frequency separation method

The conventional frequency separation method (FSM) and its derivatives are frequently employed in the literature to design the OEMS of FCHEV [54, 161, 162]. A recent utilization of low pass filter based FSM is witnessed in the reference [161], where the dynamics of energy sources are exploited to define the power separation rules (PSR). A similar application of FSM is depicted in the reference [163] to size the passive configuration of FCHEV, which indirectly reduces the stress on system. However, the PSR in the references [161, 163] are essentially static, the optimal operation of FCHEV is therefore not guranteed with respect to its fuel economy and/or health degradation of sources.

To solve the issue related to the static nature of FSM, an adaptive framework is developed in the reference [164] to update the power separation rules rules in an instantaneous manner. However, EMS constituted of adaptive framework in [164] doesnot take into account the health-degradation of sources. To study the effect of power separation rules of FSM on the design aspect of FCHEV, an offline optimizer is developed in [54]. The objective considered in the reference [54] is the optimal sizing of propulsion sources for a known driving cycle, subject to the global power balance. Despite achieving global optimality with respect to the sizing procedure, the proposed framework is not suitable in the real-time conditions due to the computational burden associated with the offline optimizer. Another innovative approach consisting of ESM is proposed in the references [99] and [39] for the online energy management of FCHEV. Here, various frequency-based filters are hybridized with an optimization framework to achieve the fuel economy. Apart from fuel economy, health degradation of PEMFC is another operational aspect which is not thoroughly investigated here.

The subject of designing an adaptive framework to adjust the power separation rules of FSM in an online manner, subject to health awareness is not comprehensively investigated. Another research gap is related to inadequacy of detailed and systematic study of designing an online EMS, explicitly adapted to the urban driving environments. Urban driving cycles differentiate themselves in terms of harsh and intermittent speed requirements, as well as prolonged start-stops. These distinctive characteristics can negatively affect the health and fuel consumption of FCHEV as well as its operational efficiency. Therefore, it is necessary and challenging to design an

efficient OEMS to achieve various operational objectives, given that an efficient urban utilization is required.

To fill these research gaps, the proposed OEMS employs a novel adaptive variant of FSM, which explores the application of a search-horizon based online optimizer and an adaptive power distributor. In context, a centralized approach is presented in Figure 28: the proposed OEMS is composed of four distinct coupled subsystems. The voltage control loop is the external subsystem to realize two critical control objectives: DC link's voltage regulation and calculation of regulation current ($A_o{}^*$). The frequency-driven online optimizer and adaptive power distributor are commutatively termed as intermediate subsystem, which splits the regulation current ($A_o{}^*$) into reference signals for the associated sources denoted by ($A_{\{fc,x\}}{}^*$). The power split is subject to instantaneous minimization of hydrogen consumption, health degradation of sources, and violation of allocated SoC limits. The reference signals $A_{\{fc,x\}}{}^*$ are then adjusted by the innermost subsystem (dynamic droop procedure) in accordance with the defined soft/hard limitations of the ESDs. Finally, the adjusted reference signals ($A_{\{fc,x\}}{}^y$) are processed by the low-level converter control to generate digital duty-cycles in order to drive the respective power conditioning units.

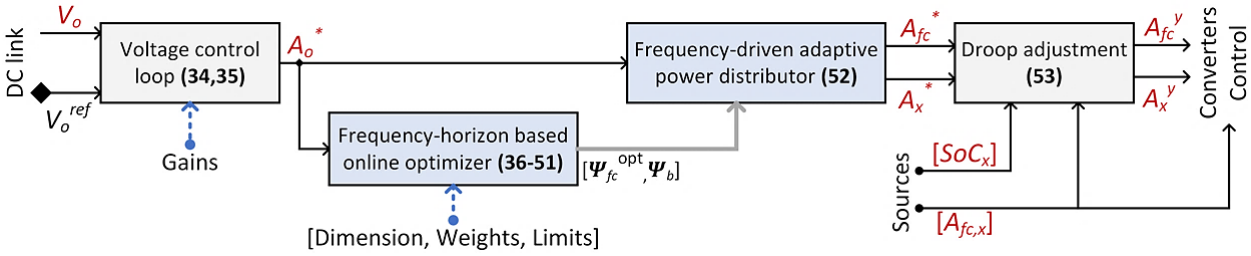

Figure 28: Schematic of the proposed OEMS based on frequency separation method.

4.1.1 Voltage control loop

The voltage control loop is the outermost subsystem of proposed OEMS (Figure 28). Preference is given to the flatness control theory due to ease of local implementation, and exploitation of fundamental energetics to regulate the DC link's voltage (V_o) and calculate the regulation current ($A_o{}^*$). The fundamentals of flatness theory are to define the state and control variables as the function of the flat output and its derivative, as stated in [165, 166]. Here, the energy stored in the DC link capacitor (π_o) is selected as the flat output, and afterwards the control variable ($A_o{}^*$) and the state variable (V_o) are defined as the relation of flat output using (34) and (35).

$$\varepsilon_\pi = \pi_o^{ref} - \pi_o = \frac{1}{2} C_o {V_o^{ref}}^2 - \frac{1}{2} C_o {V_o}^2 \tag{34}$$

$$A_o{}^* = \zeta_\alpha \varepsilon_\pi + \zeta_\beta \int \varepsilon_\pi dt \tag{35}$$

where, π_o signifies the energy within the DC link capacitor (C_o). V_o^{ref} represents the reference voltage trajectory for DC link's capacitor. ε_π is the tracking error between reference trajectory and actual measurement (V_o). $\zeta_{\{\alpha,\beta\}} > 0$ are the gains of controller to minimize the tracking error.

4.1.2 Frequency-horizon based online optimizer

The intermediate subsystem of the proposed OEMS is comprised of both the frequency-horizon based online optimizer, and the adaptive power distributor. The online optimizer introduces the terminology of rationalized-cost calculated over the frequency-horizon ($\Psi_{m=1,2,..,M}$) to tune the PEMFC power separation rule (Ψ_{fc}^{opt}) in an instantaneous manner. The overall rationalized-cost (Υ_t) is infact the weighted sum of the consituent costs associated with fuel consumption (Υ_{h_2}), health degradation of sources ($\Upsilon_{\{fc,b\}}$), and SoC violation ($\Upsilon_{SoC}{}^{x=\{b,sc\}}$). The schematic diagram of frequency-horizon based online optimizer is comprehensively presented in Figure 29.

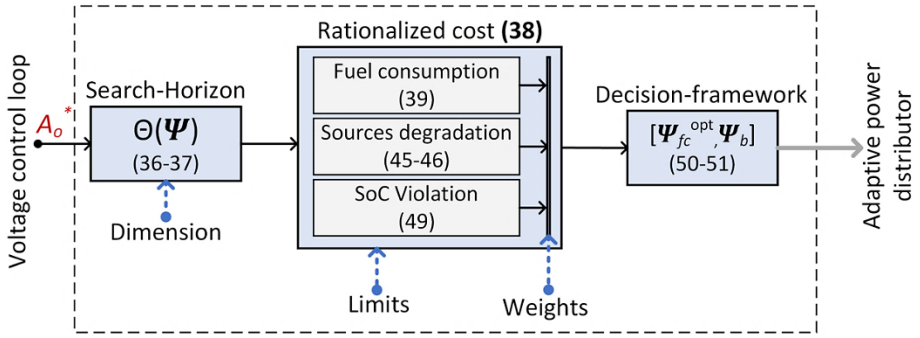

Figure 29: Schematic diagram of the frequency-horizon based online optimizer.

4.1.2.1 Search-horizon set

A search-horizon denoted by $\varphi(\Psi_m)$ is initially defined in (36) with the randomly oriented frequency members ($\Psi_{m=1,2,..,M}$) individually bounded by the upper/lower bounds ($\Psi^{\pm}$). The dimensions of search-horizon namely the range (M) and the extreme bounds ($\Psi^{\pm}$) dictate general performance and online applicability. The compromise between degree of optimization and computational burden (online implementation) is established via the range (M). While the value of extreme bounds ($\Psi^{\pm}$) indicates a contradictory relation between degree of optimization and controller's stability. Given the importance of dimensional parameters, they must be properly selected/adjusted at the system design level and should not be implicitly sensitive to external driving conditions. In this dissertation, these parameters are adjusted according to the nature of topology (with/without supercapacitor), the aggressiveness of load-following mode, and the sample (calculation) step. Accordingly, for more details, Appendix G: Table 32, Section 5.2.4.2, and Report [137] can be consulted.

The horizon members are explicitly utilized to extract PEMFC's reference signal $A_{fc}{}^*$ from the regulation current $A_o{}^*$ using frequency-driven power splitter defined in (37). Subsequently, the

reference signals associated with battery storage (${A_b}^*$) are also calculated by (37), which are not directly influenced by the frequency members.

$$\varphi(\Psi_m) = \{\Psi_1, \Psi_2, \dots., \Psi_M\} \qquad \Psi^- \leq \Psi_{m=1,2,..,M} \leq \Psi^+ \tag{36}$$

$$\begin{cases} {A_{fc}}^*\big|_{m=1,2,..,M} = \left\{{A_{fc}}^*\big|_{m=1}, \dots, {A_{fc}}^*\big|_{m=M}\right\} = \dfrac{\varphi(\Psi_m)}{s+\varphi(\Psi_m)}{A_o}^* \\ {A_b}^*\big|_{m=1,2,..,M} = \dfrac{\Psi_b}{s+\Psi_b}\left\{{A_o}^* - {A_{fc}}^*\big|_{m=1,2,..,M}\right\} \end{cases} \tag{37}$$

where, Ψ_b denotes the static power separation rule associated with the battery pack, which is essentially constant, and defined at the system design level.

4.1.2.2 Overall rationalized cost

The instantaneous overall rationalized cost Υ_t (at each dicretized sample k) against each element of horizon set $\varphi(\Psi_m)$ and reference currents ${A_{\{fc,b\}}}^*\big|_{m=1,2,..,M}$ is calculated by using (38).

$$\Upsilon_t(k) \in \mathbb{R} \in [0,1] = \sigma_{h_2}\Upsilon_{h_2}(k) + \sigma_{fc}\Upsilon_{fc}(k) + \sigma_b\Upsilon_b(k) + \sigma_{SoC}{\Upsilon_{SoC}}^{x=\{b,sc\}}(k) \tag{38}$$

where, $0 < \sigma_{\{h_2,fc,b,SoC\}} < 1$ are the consituent weighting coefficients to prioritize the effect of a certain rationalized cost over other, and to saturate the overall cost denoted by Υ_t. In this dissertation, the weighting coefficients are selected such that exactly equal importance is given to each operational indicator.

4.1.2.3 Rationalized fuel consumption cost

The instantaneous rationalized fuel cost denoted by (Υ_{h_2}) is evaluated by using (39). The rationalized fuel cost can be easily integrated in the optimization process without any explicit need of price coefficients.

$$\Upsilon_{h_2}(k) \in \mathbb{R} \in [0,1] = \frac{\dot{m}_{h_2}(k)\big|_{{A_{fc}}^*(k)}}{\dot{m}_{h_2}\big|_{{A_{fc}}^{max}}} \tag{39}$$

where, ${A_{fc}}^{max}$ corresponds to the max. permissible PEMFC's current, and $\dot{m}_{h_2}$ is the fuel consumption rate.

4.1.2.4 Rationalized PEMFC degradation cost

The health degradation of PEMFC on whole is a sophisticated process manifesting due to a wide range of electrical, mechanical, and thermal operating conditions [100]. Appropriately assessing and integrating the health degradation in the real-time EMS is a challenging task in context of finding a trade-off between the computational complexity and accuracy of the assessment. The empirical methods are rigourously utilized in the literature to assess and quantify the degradation

of PEMFC [48, 84]. The degradation of PEMFC is empirically related to its operating conditions such as over/underloading, frequent start-stop and load shifting. The overall degradation pehonemena, as exhibited in Figure 30 can be generalized as followings:

- *Catalyst layer degradation*: Electrical operating conditions such as overloading, frequent start-stop and shifting the load beyond the ramping capability of PEMFC results in the problem of fuel starvation. The fuel starvation causes reduction in the electrochemical surface area (ECSA), which contributes directly to the catalyst layer degradation [100, 167].

- *Membrane degradation*: Prolonged thermal stress due to electrical overloading and various mechanical stresses, generally accelerate the deterioration of the membrane within PEMFC [168].

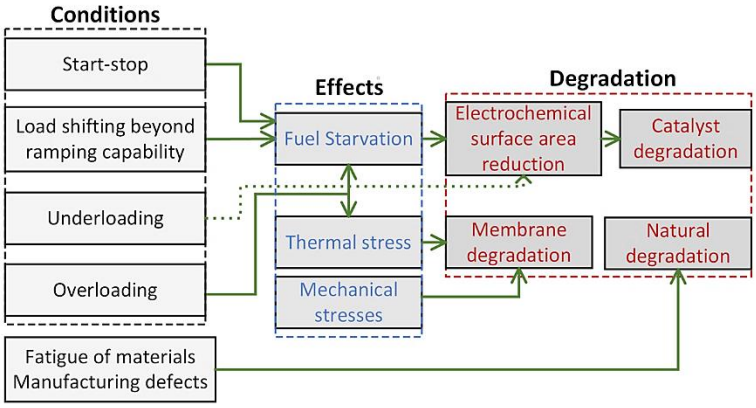

Figure 30: Generalized PEMFC's degradation process.

- *Natural degradation*: Due to the physical fatigue of materials used and defects in the manufacturing process, there is always a natural degradation rate associated to the PEMFC stack [90]. The typical parameter to gauge and effectively quantify the natural degradation is the EoL of the PEMFC stack, usually specified in hrs.

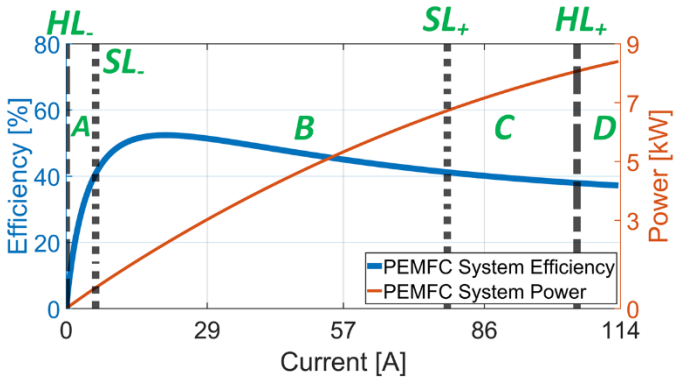

(a): Graphical illustration.

Name	From	To	Description
A	HL_-	SL_-	Underloading zone
B	SL_-	SL_+	Suitable zone
C	SL_+	HL_+	Overloading zone
D	HL_+	-	Prohibited zone

(b): Tabulated description.

Figure 31: Concept of PEMFC operating zones based on soft/hard limiters.

In this dissertation, the empirical degradation model used in [48, 75, 84] is initially adopted, and later modified with the joint relevance of the operating efficiency of PEMFC system. A concept of operating zones bounded by soft/hard limiters ($SHL_{\pm}$) is introduced to quantify the operating conditions-based health degradation of PEMFC with simultaneous consideration of its operating efficiency. The concept of bounded operating zones is illustrated in Figure 31 for $6kW$ PEMFC system of hypothetical vehicle, where complete operating range is divided in the four discrete zones. The zone-B provides higher operating efficiency and only accounts for the health degradation due to load shifting, provided that load shifting exceeds the physical ramping capability of PEMFC. Similarly, the zone-A and zone-C individually reflect lower efficiency regions accounting for the health degradation due to under and overloading. In this manner, the overall health degradation of PEMFC due to various operating conditions is comprehensively assessed and quantified as rationalized structure using (40)-(44). The rationalized cost structure enables flexible integration of quantified health degradation in the optimization formulation without finding the suitable equivalent factors and price coefficients.

- *Overloading*: The instantaneous rationalized overloading cost (Υ_{ol}) is calculated by using (40). Here, ${A_{fc}}^{*}$ is the PEMFC reference current generated within the search horizon.

$$\Upsilon_{ol}(k) \in \mathbb{R} \in [0,1] = \frac{{A_{fc}}^{*}(k) - SL_{+}}{HL_{+} - SL_{+}} \qquad \{SL_{+} \leq {A_{fc}}^{*}(k) \leq HL_{+}\} \tag{40}$$

- *Underloading*: The instantaneous rationalized underloading cost (Υ_{ul}) is calculated by (41).

$$\Upsilon_{ul}(k) \in \mathbb{R} \in [0,1] = \frac{SL_{-} - {A_{fc}}^{*}(k)}{SL_{-} - HL_{-}} \qquad \{HL_{-} \leq {A_{fc}}^{*}(k) \leq SL_{-}\} \tag{41}$$

- *Load shifting:* The instantaneous rationalized load shifting cost (Υ_{ls}) beyond the ramping capability of PEMFC (defined by hard/soft ramping rates ${\Delta_r}^{HL}/{\Delta_r}^{SL}$) is calculated by using (42).

$$\Upsilon_{ls}(k) \in \mathbb{R} \in [0,1] = \frac{\left|{A_{fc}}^{*}(k) - {A_{fc}}^{*}(k-1)\right| - {\Delta_r}^{SL}}{{\Delta_r}^{HL} - {\Delta_r}^{SL}} \qquad \begin{Bmatrix} HL_{-} \leq {A_{fc}}^{*}(k) \leq HL_{+} \\ {\Delta_r}^{SL} \leq \left|{A_{fc}}^{*}(k) - {A_{fc}}^{*}(k-1)\right| \leq {\Delta_r}^{HL} \end{Bmatrix} \tag{42}$$

- *Start-stop:* The instantaneous start-stop cost (Υ_{ss}) is calculated by (43). Since, Υ_{ss} is already logically bounded, no rationalization is performed.

$$\Upsilon_{ss}(k) = \left|\langle {A_{fc}}^{*}(k) == 0\rangle - \langle {A_{fc}}^{*}(k-1) == 0\rangle\right| \tag{43}$$

- *Natural degradation:* The instantaneous natural health degradation (Υ_{n}) of PEMFC stack is calculated by using (44). Here, EoL_{hrs} is the specified life span of PEMFC in hrs before reaching end-of-life (EoL). Where, δt is the fixed sampling time.

$$\Upsilon_n(k) \in \mathbb{R} \in [0,1] = \Upsilon_n(k-1) + \frac{\delta t}{3600 EoL_{hrs}} \tag{44}$$

- *Overall health degradation:* The overall instantaneous health degradation cost (Υ_{fc}) of PEMFC stack is mathematically expressed in (45). Here, σ_{fcx} are the bounded weighting coefficient to saturate the overall PEMFC health degradation within the rationalized limits. The proposed rationalized health degradation quantification presented mathematically in (40)-(45) is fexible in terms of its integration in the optimizer. The underlying justification is that the explicit information about the price coefficients and appropriate configuration of equivalent factors is not required in the proposed quantification.

$$\begin{aligned} \Upsilon_{fc}(k) \in \mathbb{R} \in [0,1] \\ = \sigma_{fc1}\Upsilon_{ol}(k) + \sigma_{fc2}\Upsilon_{ul}(k) + \sigma_{fc3}\Upsilon_{ls}(k) + \sigma_{fc4}\Upsilon_{ss}(k) \\ + \sigma_{fc5}\Upsilon_n(k) \quad \{1 > \sigma_{fcx} > 0\} \end{aligned} \tag{45}$$

4.1.2.5 Rationalized battery degradation cost

The instantaneous rationalized battery degradation cost identified by Υ_b is calculated by using (46).

$$\begin{cases} \Upsilon_b(k) \in [0,1] = \dfrac{\Delta \mathrm{b}^-(k)|_{A_b{}^*(k)}}{\Delta \mathrm{b}^-(k)|_{A_b{}^{max}}} \\ \Delta \mathrm{b}^-(k) = \dfrac{|A_b{}^*(k)|}{2N_b(c,T_b)Q_b} \end{cases} \tag{46}$$

where, $A_b{}^*$ and $A_b{}^{max}$ are respectively the reference battery current generated within search horizon (37) and max. permissible current. Subsequently, $\Delta \mathrm{b}^-$ depicts the instantaneous loss in the remaining capacity of the battery pack.

4.1.2.6 Rationalized SoC violation cost

Analogous to the operating zones based quantification of PEMFC health degradation, the instantaneous SoC violation of the storage devices ($x = \{b, sc\}$) beyond the allocated thresholds is quantified in a rationalized manner. These thresholds and the associated operating regions are commutatively elaborated in Figure 32 and Table 11. It can be observed that the penalty cost is only accounted for upper/lower violation regions only. Depending on the violation zone, dictated by soft limiters ($SoC_{SL}{}^{\pm}$) and hard limiters ($SoC_{HL}{}^{\pm}$), the SoC penalties are rationalized according to (47)-(49) for their flexible augmentation in the online optimizer.

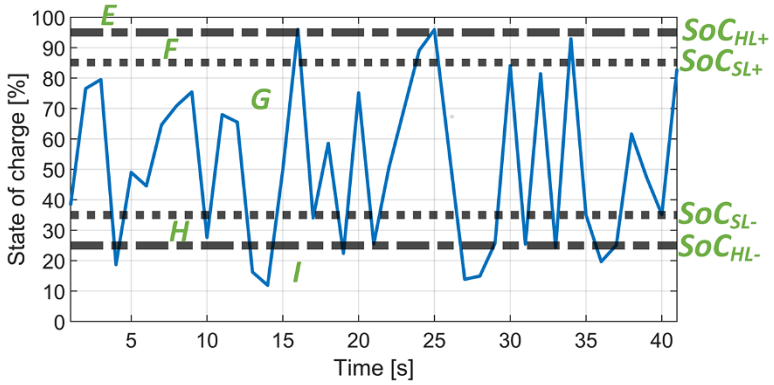

Figure 32: Concept of SoC violation zones based on soft/hard limiters.

- *Upper violation*: The instantaneous rationalized penalty (${\Upsilon_{SoC}}^{up}$) corresponding to upper violation of SoC is calculated by using (47) at sample k. Here, the discretization of (13) is performed using forward/backward Euler computaion method (built-in functionality of MATLAB/Simulink) [169].

$$ {\Upsilon_{SoC}}^{up}(k) \in \mathbb{R} \in [0,1] = \frac{SoC_x(k) - {SoC_{SL}}^{+}}{{SoC_{HL}}^{+} - {SoC_{SL}}^{+}} \qquad \left\{ {SoC_{SL}}^{+} \leq SoC_x(k) \leq {SoC_{HL}}^{+} \right\} \quad (47) $$

- *Lower violation*: The instantaneous rationalized penalty (${\Upsilon_{SoC}}^{lo}$) corresponding to the lower violation of SoC is calculated by using (48).

$$ {\Upsilon_{SoC}}^{lo}(k) \in \mathbb{R} \in [0,1] = \frac{{SoC_{SL}}^{-} - SoC_x(k)}{{SoC_{SL}}^{-} - {SoC_{HL}}^{-}} \qquad \{ {SoC_{HL}}^{-} \leq SoC_x(k) \leq {SoC_{SL}}^{-} \} \quad (48) $$

- *Total violation*: The penalty (Υ_{SoC}) corresponding to the instantaneous overall violation of SoC is calculated by using (49).

$$ {\Upsilon_{SoC}}^{x}(k) \in [0,1] = {\Upsilon_{SoC}}^{up}(k) + {\Upsilon_{SoC}}^{lo}(k) \qquad \left\{ {SoC_{HL}}^{-} \leq SoC_x(k) \leq {SoC_{HL}}^{+} \right\} \quad (49) $$

where, $x = \{b, sc\}$ corresponds to the composite ESS consisting of both supercapcitors bank and li-ion batteries pack.

Table 11: Description of SoC violation zones based on soft/hard limiters

Name	From	To	Description	Violation cost
E	100%	${SoC_{HL}}^{+}$	Upper prohibited	×
F	${SoC_{HL}}^{+}$	${SoC_{SL}}^{+}$	Upper violation	✓
G	${SoC_{SL}}^{+}$	${SoC_{SL}}^{-}$	Allowable	×
H	${SoC_{SL}}^{-}$	${SoC_{HL}}^{-}$	Lower violation	✓
I	${SoC_{HL}}^{-}$	0%	Lower prohibited	×

4.1.2.7 Decision framework

Within the proposed OEMS, the power separation rule associated with the PEMFC stack is optimally updated in an online (instantaneous) manner using a distinct decision framework expressed in (50). The optimal power separation rule dictated by Ψ_{fc}^{opt} is subject to a set of equality and non-equality constraints presented in (51). The constraints include power balance, PEMFC power limits and ramping capability, ESS power limits, traction motor power limits, SoC violation limits and DC link limits respectively.

$$\Psi_{fc}^{opt}(k) = \arg min_{\varphi(\Psi_m)} \ \langle Y_t|_m(k)\rangle \tag{50}$$

$$s.t. \begin{cases} P_{fc}(k) + P_{x=\{b,sc\}}(k) = P_o(k) + P_r(k) \\ P_{fc}^{max} \geq P_{fc}(k) \geq 0 \\ P_{x_{max}}^{-} \leq P_{x=\{b,sc\}}(k) \leq P_{x}^{+}{}_{max} \\ P_{max}^{-} \leq P_o(k) \leq P_{max}^{+} \\ SoC_{HL}{}^{-} \leq SoC_{x=\{b,sc\}}(k) \leq SoC_{HL}{}^{+} \\ \Delta_{bus}{}^{-}V_o^{ref} \leq V_o(k) \leq \Delta_{bus}{}^{+}V_o^{ref} \end{cases} \tag{51}$$

where, $x = \{b, sc\}$ denotes the composite ESS. P_o and P_r respectively are the traction and braking power. The notations $P_{x_{max}}^{\pm}$ and $P_{max}^{\pm}$ are respectively reserved for denoting the upper/lower limits of storage devices and traction motor. $\Delta_{bus}{}^{\pm}$ corresponds to the permissible instantaneous %violation in the DC link's voltage in comparison to the reference V_o^{ref}.

Its worth mentioning here that the instantaneous optimization formulation presented in (50) is solved as an un-constrained problem by decoupling the associated constraints: the equality constraint (power balance) is satisfied via intrinsic characteristics of the local frequency-driven power distributor, the inequality power limitations are met by introducing local saturation blocks, the inequality constraint related to SoC is satisfied via droop based adjustment criteria, and finally the DC bus profile is bounded within its allocated range subject to satisfactory performance of the outermost (voltage compensation) control loop. Moreover, the optimization direction is dictated by introducing the memory retension feature, which randomizes the search-horizon members at sample k based on the best of previous sample $(k-1)$.

4.1.3 Frequency-driven adaptive power distributor

After the onine allocation of the optimal power separation rule (Ψ_{fc}^{opt}), the demanded traction power is distributed among the PEMFC stack, and hybrid ESDs using a frequency-driven power separator presented in (52). However unlike most of the litearture, an adaptive variant is established, which splits the power according to online-tuned power separation rule, subject to simultaneous minimization of fuel consumption cost, sources degardation cost, and SoC violation cost. The schematic of proposed power distributor is illustrated in Figure 33.

$$
\begin{aligned}
A_{fc}{}^{*} &= \frac{\Psi_{fc}^{opt}}{s+\Psi_{fc}^{opt}} A_o{}^{*} \\
A_b{}^{*} &= \frac{\Psi_b}{s+\Psi_b}\left\{A_o{}^{*} - A_{fc}{}^{*}\right\} \\
A_{sc}{}^{*} &= A_o{}^{*} - \left\{A_{fc}{}^{*} + A_b{}^{*}\right\}
\end{aligned}
\tag{52}
$$

where, Ψ_b denotes the static power separation rule associated with the battery pack, which is essentially constant, and defined at the system design level.

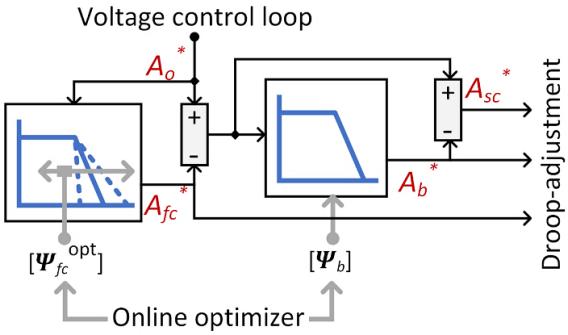

Figure 33: Schematic diagram of the proposed adaptive frequency-driven power distributor.

4.1.4 Dynamic droop adjustment

A droop adjustment procedure is proposed, and consecutively integrated in the proposed OEMS to restrict the SoC of the storage devices well within the allocated design thresholds. The fundamental concept is illustrated in Figure 34. Here, depending on the direction of power flow, the current of $x^{th} = \{b, sc\}$ storage device ($A_{x=\{b,sc\}}{}^{*}$) is adaptively adjusted as $A_{x=\{b,sc\}}{}^{y}$ within the upper/lower voilation zones (indicated distinctly by F/H regions) by using the droop functions ($\Theta^{\pm}$). The corresponding measures are mathematically expressed in Table 12.

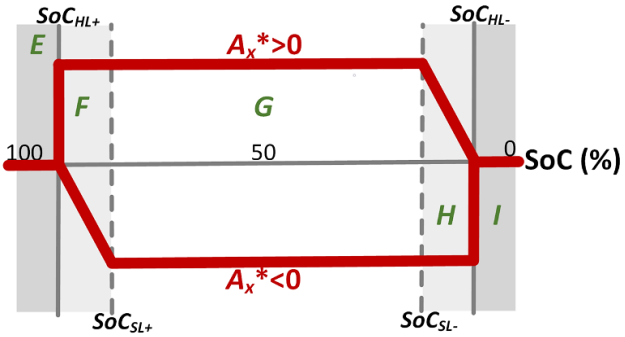

Figure 34: Graphical concept of dynamic droop adjustment.

Mathematically, the droop functions ($\Theta^{\pm}$) are expressed by (53). The proposed adjustment procedure is universally applicable, as it doesnot require any offline tuning for a particular driving environment.

$$\Theta^{+} = 1 - \frac{SoC_x - {SoC_{SL}}^{+}}{{SoC_{HL}}^{+} - {SoC_{SL}}^{+}}$$
$$\Theta^{-} = 1 - \frac{{SoC_{SL}}^{-} - SoC_x}{{SoC_{SL}}^{-} - {SoC_{HL}}^{-}} \quad (53)$$

Table 12: Measures introduced by the dynamic droop adjustment

Zone	Adjust	Retain	Halt	Braking	Expression
G	×	✓	×	×	${A_x}^{y} = {A_x}^{*}$
F	✓	×	×	✓	${A_x}^{y} = \Theta^{+}{A_x}^{*}\ ({A_x}^{*} < 0)$ ${A_x}^{y} = {A_x}^{*}\ ({A_x}^{*} > 0)$
H					${A_x}^{y} = \Theta^{-}{A_x}^{*}\ ({A_x}^{*} > 0)$ ${A_x}^{y} = {A_x}^{*}\ ({A_x}^{*} < 0)$
E	×	×	✓	✓	${A_x}^{y} = 0$
I					

4.2 Comparative EMS based on frequency separation

To validate the performance of the proposed Online EMS, a fair comparative background is developed. Two distinct and well-established EMS based on frequency-separation method are adopted from the literature. The details are presented in the subsequent sections.

4.2.1 Conventional (static) approach

The conventional FSM represents the most established approach, where the power separation/splitting rules are essentially static in nature. With the static rules, the performance of vehicle, though the optimality with respect to key operational objectives such as hydrogen consumption and/or sources degradation is not guaranteed. The frequency-based power separation rules are generally selected by the designer expertise and may vary significantly depending on the application and the nature/dimensions of studied vehicle. The theme of conventional/static FSM is employed from the references [161, 162], where the conventional FSM is utilized to develop online EMS of two different hybrid powertrains.

4.2.2 Off-line tuned approach

The offline-tuned FSM is influence by the reference [54], where the frequency splitting rule associated with the PEMFC stack is tuned in an offline manner using a multi-objective metaheuristic optimizer. The metaheuristics have found countless applications in a diverse range

of applications [170, 171]. The optimization framework is developed to minimize the cumulative weight of the hybrid powertrain system. In this dissertation, the same multi-objective metaheuristic optimizer is used as of [54]. However, instead of minimizing the overall weight of the hybrid system, the decision framework prioritizes the minimization of overall rationalized cost (Υ_t). The offline decision framework is presented in (54).

$$\Psi_{fc}^{opt} = \arg min_{\varphi(\Psi_m)} \langle \Upsilon_t |_m \rangle \tag{54}$$

4.3 Low-level control: Converters control schemes

4.3.1 Conventional proportional-integral compensator

Because of the relative ease of implementation, the increased popularity, the lower computational complexity, and general adequacy in the tracking performance (subject to the tuning of gains $\{K_q^{p,i}\}$), the conventional PI compensator is a preferred choice to design the low-level control of studied FCHEVs. The implementation is graphically exhibited in Figure 35.

The working principle is well established: the compensator minimizes the error (ε_q) between the reference signals generated by proposed OEMS (${A_q}^{y}$) and the measured (controllable) signals denoted by A_q. The measured signals (A_q) are effectively logged using the appropriate sensing units attached to the sources. A properly tuned PI compensator produces a continuous signal α_q in relation to the minimization of compensation error (ε_q), as presented in (55)-(56).

$$\varepsilon_q = {A_q}^{y} - A_q \tag{55}$$

$$\alpha_q \in \mathbb{R} \in]0,1[= K_q^p \varepsilon_q + K_q^i \int \varepsilon_q dt \tag{56}$$

where, the gains $K_q^{p,i}$ correspond individually to the proportional and integral action. The notation $q = \{fc, x\}$ is reserved to represent the sources i.e., the PEMFC, and $x = \{b, sc\}$ for the composite ESDs. The continuous signal α_q is either directly fed to the average-model power conversion stage, or to the switching-model conversion stage after converting to a digital signal (g_q) via PWM modulator, mathematically expressed by (57).

$$\begin{cases} \alpha_q \geq s & g_q = hi \\ else & g_q = lo \end{cases} \tag{57}$$

where, s represents the reference modulation waveform generated externally by a saw-tooth generator. In Figure 35, the subsystem 'transport delay system' introduces the appropriate phase-delay in the signals α_q and/or g_q in case of interleave power stage. It is strictly observed that the gains $\left(K_q^{p,i}\right)$ largely impact the performance of PI controllers, and the presence of modulator effects the distribution of current among the participant legs of interleave power converters.

In this dissertation, to tune the gains $\left(K_q^{p,i}\right)$ of the controller, the experience based heuristic approach is adopted, which expedites the adjustment of gains based on observing the system performance in a recursive manner under the subjected operating conditions. The gains are understandingly sub-optimal in this manner, though tracking performance and overall stability are found to be satisfactory in the studied driving conditions. It is worth mentioning here that the conventional PI controller is extensively used in this dissertation, especially with the utilization of average transformer power stage Figure 23b and with the ease of integration in the whole methodology (coordination of sizing and OEMS).

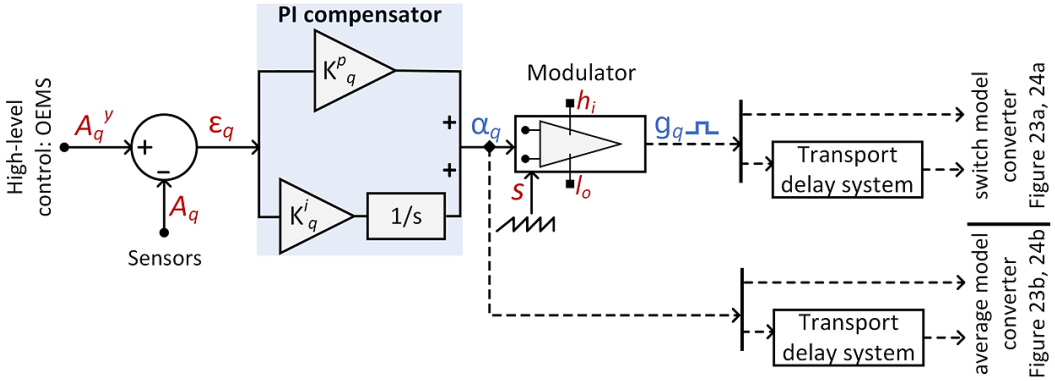

Figure 35: Layout scheme of the low-level control based on conventional PI compensator.

4.3.2 State-horizon predictive controller

The state-horizon predictive controller is studied and implemented as an alternate to conventional PI compensator to facilitate several advantages such as elimination of the modulation block and enhanced overall stability. However, it suffers from a higher computation complexity especially in case of interleave power stage with no. of legs $n \geq 3$, and applicability is also limited to the real converter with actual switches only. The schematic layout of the proposed state-horizon predictive controller is presented in Figure 36. Subsequently, the working principle is divided in two steps, which are comprehensively presented in the subsequent section.

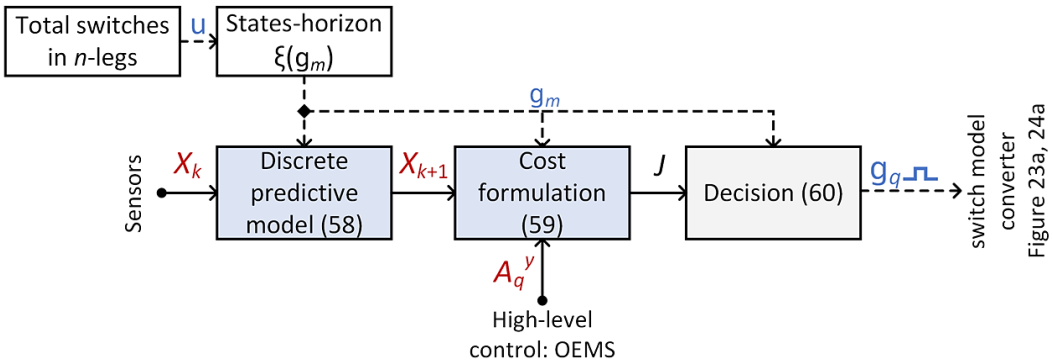

Figure 36: Schematic of the state-horizon predictive controller for FCHEV applications.

4.3.2.1 Discrete predictive model

First step in the design of state-horzon predictive controller is to develop a computationally simple yet effective discrete-time predictive model of the plant. In the case of switch-model power stage, the predictive model is presented in (58), which is effectively extracted from the state-model provided in (22). Since, the voltage-loop is decoupled, the subjected states represented by $\dot{X_{nx1}}$ only include the information about the currents of 'n-legs' interleave power stage.

$$\begin{cases} X_{nx1}[k+1] = I_{nxn}X_{nx1}[k] + \emptyset_{nx1}[k] \\ \emptyset_{nx1}[k] = \left\{(\tau^{\alpha}_{nxn} + \mathrm{g}_{nxn}[k])X_{nx1}[k] + \tau^{\beta}_{nxn}\lambda_{nx1}[k]\right\}\Delta T_s \end{cases} \tag{58}$$

where, I_{nxn} is the identity matrix. The notations k and ΔT_s denote the sample at which computation is performed and the sampling time respectively.

4.3.2.2 Cost function and decision

After the definition of discretized state model (58), next step is to define an adequate cost function model. The cost-function formulated in this dissertation is presented in (59). Within the optimization model, the cost ($\mathbb{J}$) of each possible switching combination (g_m) from the state-horizon set defined by $\xi(\mathrm{g}_{m=1,2,..,2^{\cup}})$ is predicted at the sample $(k+1)$ using (59). The switching combination which bears the minimum cost (g_q), is then applied in real-time to the switching devices of switch-model power stage in order to optimally track the reference current ${A_q}^{y}$, as mathematically expressed in (60).

$$\mathbb{J}[k+1] = \sum_{i=1}^{n_{fc}} \left\| \frac{{A_{q=fc}}^{y}}{n_{fc}} - X_i[k+1] \right\|_1 + \sum_{j=1}^{n_x} \left\| \frac{{A_{q=x}}^{y}}{n_x} - X_{n_{fc}+j}[k+1] \right\|_1 \tag{59}$$

$$\mathrm{g}_q[k+1] = min_{\xi(\mathrm{g}_m)} \langle \mathbb{J}[k+1] \rangle \tag{60}$$

where, U are the total number of active switches in the 'n-leg' interleave power stage, such that U= n_{fc}+2*n_x. The notation $n_{\mu=\{fc,x\}}$ expresses the no. of legs reserved for PEMFC and storage devices. It's worth mentioning that the cost function formulated in (59) doesn't consider the controller effort, as all the possible switching states are exploited to reach the best possible. The tracking performance is expected to be superior, but at the compromise of extensive computational burden, highlighting the major limitation of this approach. Another important point is that, in this dissertation, the predictive controller is implemented as a separate part (therefore not integrated in the coordination approach). Moreover, application wise, it is also limited to the switching model power stage Figure 24, existing in the commercial vehicles.

Chapter 5: Results and discussion

This chapter is dedicated for the critical evaluation of developed methods to address the key design and control aspects of studied FCHEVs. The vital operational aspects of the considered hypothetical vehicles such as power balance, hydrogen consumption, and sources degradation are comprehensively studied, and results are compared to those of the established approaches in order to highlight the efficacy of the developed methods. The study is extended to the vehicle with specifications and parameters matched with those of a commercial-scale FCHEV. The behavior of studied vehicles is also studied in the driving cycle with real driving data to reflect what to expect performance-wise in real driving environment. The relevant experimental work, practical validation, and the associated findings are presented as the concluding remark of this chapter.

5.1 Numerical simulations

To highlight the conceptual effectiveness of the developed methods, a comprehensive numerical validation framework is built in MATLAB/Simulink (parameters presented in Appendix G: Table 32). The framework is composed of several case-studies with the diverse range of driving environments, while giving special attention to urban/suburban driving cycles due to their distinct challenging nature such as intermittent acceleration/deceleration and prolonged start-stops. The validation framework and associated details are presented in Table 13.

Table 13: The simulations-based validation framework and associated case-studies.

Case-study	Studied vehicle		Driving cycles				
	Hypothetical	Commercial-grade	Urban	Urban Suburban	Urban Highway	Highway	Real data
A	Light-duty	×	Artemis-u	WLTP-c1	×	×	×
B	Mid-size	×	×	×	LA92	×	×
C	×	Mirai [137]	×	×	×	Artemis-m	×
D	Light-duty	×	×	×	×	×	ETC-FIGE 4

5.1.1 Case-study A: *Light-duty hypothetical vehicle*

Two popular urban/suburban driving cycles (Artemis-urban and WLTP-class 1) are throughly studied to investigate the performance of hypothetical light-duty vehicle Appendix A: Table 27. The characteristic waveform of these driving cycles are presented in Figure 37. The Artemis urban cycle is classified as a harsh driving cycle with intermittent acceleration/braking and prolonged start/stops. Therefore, Artemis cycle presents a compelling challenge for the online EMS in

context of minimizing hydrogen [h_2] consumption and sources degradation. On the other hand, WLTP-class 1 is a sub-urban driving environment with higher speed but less challenging nature.

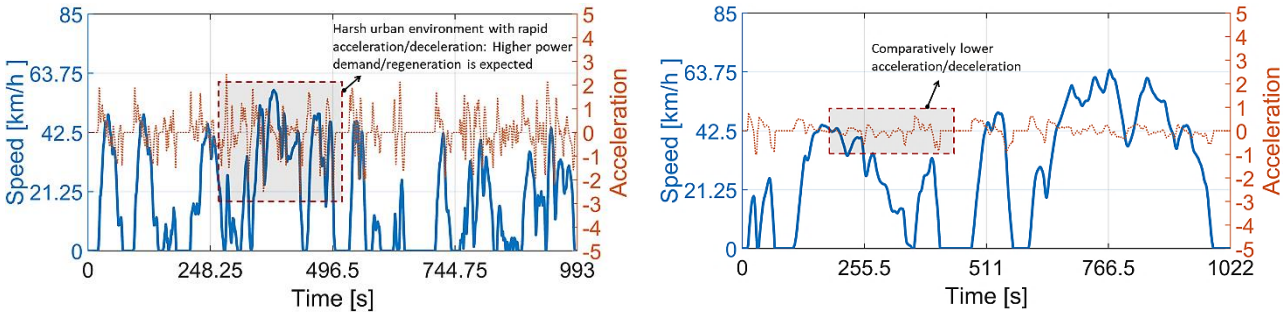

(a) Artemis-urban. (b) WLTP class-1.

Figure 37: Profiles of studied driving cycles for the hypothetical light-duty vehicle.

5.1.1.1 Optimal configuration of power sources

By exploiting the flexible design coefficients, energy sources of the hypothetical light-duty FCHEV are optimally configured from their flexible range, with a fair compromise among relative realization of the operational criteria (hydrogen consumption and sources degradation), and the associated price. The PEMFC being the main power source is sized by reflecting the impact of design coefficient Δ_{fc} on its hydrogen consumption, its degradation, and the associated price. In this context, Figure 38 depicts three choices to size the PEMFC stack from its flexible range: (i) comprise between the expected price and the hydrogen consumption, (ii) compromise between the price and the health degradation, and (iii) compromise between all the mentioned criteria. For that purpose, the expected price, and operational parameters (p) corresponding to the i^{th} design coefficient (${\Delta_{fc}}^{i}$) are rationalized (r) according to (61). Where, $p|_{\Delta_{fc}}$ corresponds to the non-rationalized parameter over the complete horizon of Δ_{fc}.

$$r|_{{\Delta_{fc}}^{i}} \in \mathbb{R} \in [0,1] = \frac{p|_{{\Delta_{fc}}^{i}}}{\max\langle p|_{\Delta_{fc}}\rangle} \tag{61}$$

In this dissertation, all three parameters (price, degradation, and hydrogen consumption) are equally exploited to configure PEMFC stack. Accordingly, the optimal size exists at the lower spectrum of the design coefficient Δ_{fc}, which equates to Δ_{fc}=0.75 in the case of WLTP-class 1 cycle. It was expected as the lowest value of Δ_{fc} corresponds linearly to a PEMFC stack with lowest possible nominal capacity, and thus lowest expected price. Though, a significant deviation is observed in Artemis cycle (Figure 38a), where instead of choosing Δ_{fc}=0.75, the optimal selected value is present at the upper spectrum (Δ_{fc}=1.0) due to adverse effect of Artemis-urban cycle on the health degradation of candidate PEMFC stacks. Subsequently, the final PEMFC configuration due to the selected values of Δ_{fc} is collectively tabulated in Table 14 for the studied driving cycles.

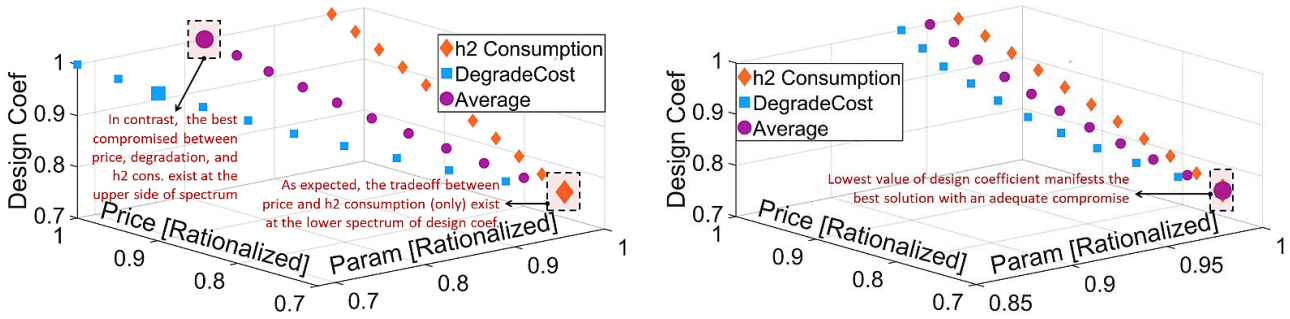

(a) Artemis-urban. (b) WLTP class-1.

Figure 38: Sizing the PEMFC stack: the candidate solutions, and the best compromise.

After selecting the optimal size of PEMFC stack from its allocated sizing range, hybrid ESD is configured by manipulating the associated coefficient Δ_{doh}. The operational criteria considered here is the rationalized degradation of battery pack, which is compared to the expected cumulative price of ESD devices (supercapacitors bank and batteries pack) to appropriately select Δ_{doh} from its flexible range ($0.5 \leq \Delta_{doh} \leq 0.75$). Following this, Figure 39 proposes the design coefficient in its lower range (Δ_{doh}=0.5) to size ESD components for the studied driving cycles. The selected design coefficients reflect a suitable compromise among expected price of ESD and degradation of battery pack.

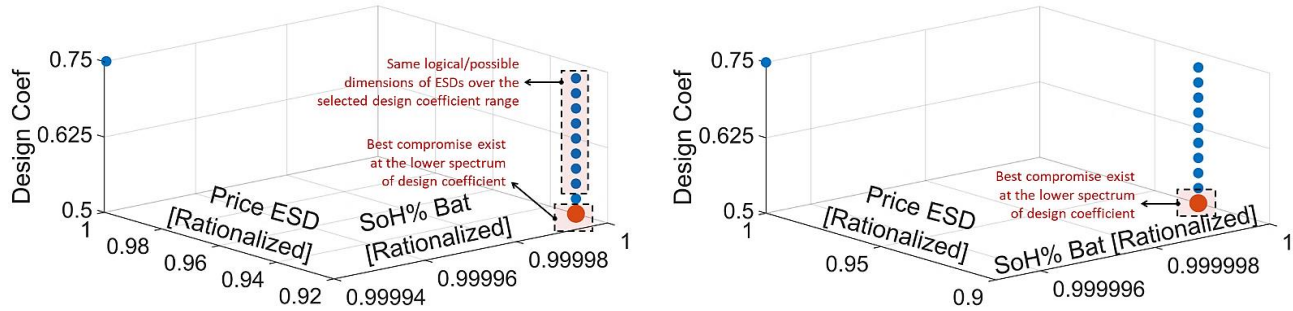

(a) Artemis-urban. (b) WLTP class-1.

Figure 39: Sizing the ESD system: the candidate solutions, and the best compromise.

It is observed that a specific range of coefficient Δ_{doh} in Figure 39 manifests the same configuration (only a logical combination of series/parallel cells is possible for storage devices), therefore producing the same solution. Finally, the optimal config is tabulated in Table 14.

Table 14: Final configuration for the power sources of hypothetical light-duty vehicle.

Driving cycle	Coefficients		Energy source		
	Δ_{fc}	Δ_{doh}	PEMFC $[kW]$	Battery $[kWh]$	Supercap $[F]$
WLTP class-1	0.75	0.5	4.5	0.62	68.18
Artemis-urban	1.0	0.5	6.0	0.62	68.18

5.1.1.2 Operational parameters of the vehicle

To reach global power balance under the influence of uncertain driving action and environment is one of the most important operational criteria. In this context, the power distribution among energy sources of hypothetical light-duty FCHEV is exhibited in Figure 40 for the studied driving cycles. Conclusively, the low frequency components of traction power are appropriately allocated to PEMFC, to match its slower dynamics. While, the residual load is balanced by the composite ESD. Due to the harsh nature of Artemis-urban cycle in terms of intermittent acceleration and braking, the power being demanded/provided by the traction system is much higher than that of WLTP cycle, as illustrated in Figure 40 (a, b).

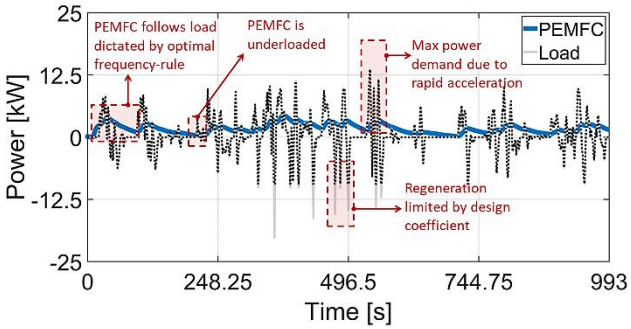

(a) Artemis-urban: Load and PEMFC.

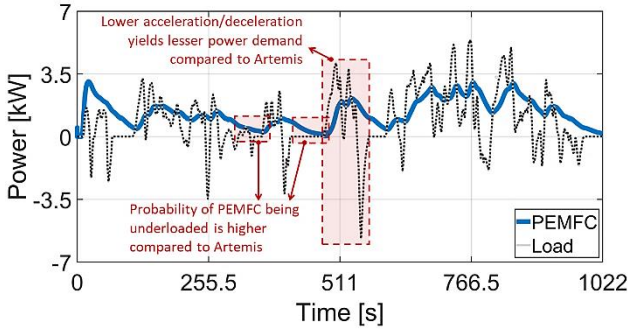

(b) WLTP-class 1: Load and PEMFC.

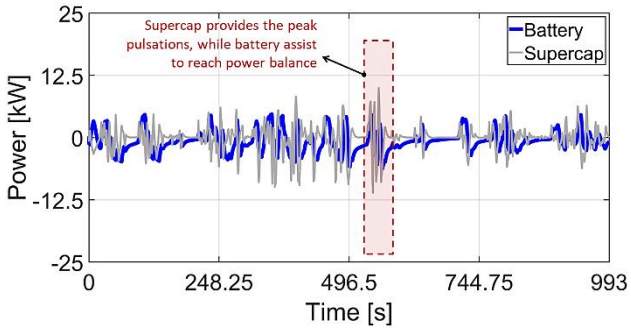

(c) Artemis-urban: Battery and supercap.

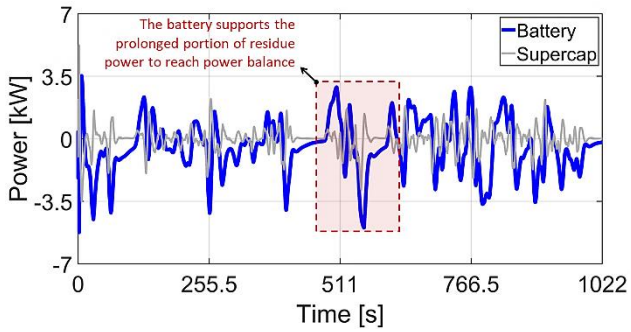

(d) WLTP-class 1: Battery and supercap.

Figure 40: Power balance waveforms for the hypothetical light-duty vehicle.

A similar influence is witnessed on the power profiles of storage devices, where they are stressed more in Artemis-urban cycle (Figure 40c). Therefore, the health of ESDs is expected to degrade faster in Artemis-cycle, which is especially true for the battery pack due to increment in the charging/discharging cycles, and that is at a much higher c-rate compared to the nominal one.

The SoC% of the storage devices and SoH% of the battery pack are among the most crictical operational parameters in relation to the vehicular applications. Mathematically, to represent the effectiveness of EMS in terms of reducing the SoC violation, a parameter 'degree of violation' denoted by Δ_d is introduced, which is calculated by (62).

$$\begin{cases} {\Delta_d}^{+} = \dfrac{1}{T_{dc}} \displaystyle\int_{t_i}^{t_f} \dfrac{\left|SoC_x(\tau) - {SoC_{SL}}^{+}\right|}{{SoC_{HL}}^{+} - {SoC_{SL}}^{+}} d\tau & A_x(\tau) < 0 \\ {\Delta_d}^{-} = \dfrac{1}{T_{dc}} \displaystyle\int_{t_i}^{t_f} \dfrac{\left|{SoC_{SL}}^{-} - SoC_x(\tau)\right|}{{SoC_{SL}}^{-} - {SoC_{HL}}^{-}} d\tau & A_x(\tau) \geq 0 \end{cases} \tag{62}$$

$$\Delta_d \in [0,1] = {\Delta_d}^{+} + {\Delta_d}^{-}$$

For the driving cycle defined over $T_{dc} = t_f - t_i$, the parameter Δ_d is defined for x^{th} storage device according to violation from the soft permissible violation limits.

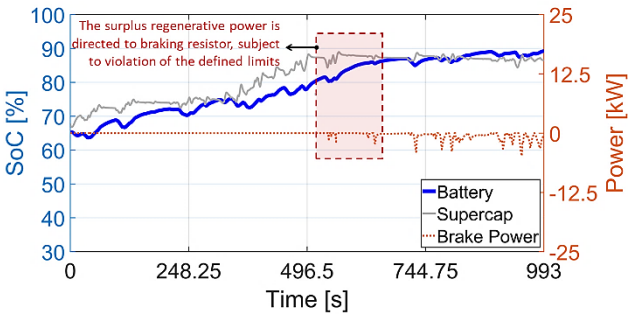

(a) Artemis-urban: SoC% of ESDs.

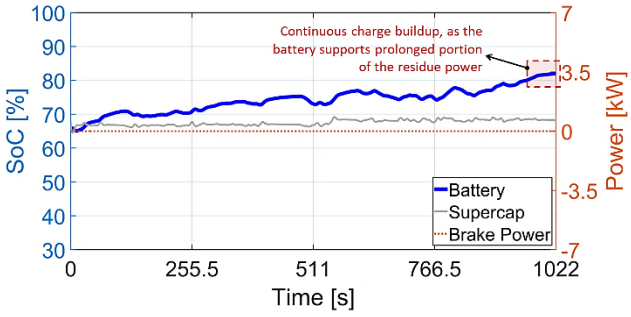

(b) WLTP-class 1: SoC% of ESDs.

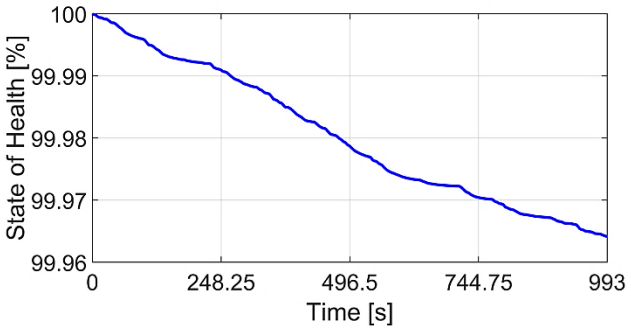

(c) Artemis-urban: SoH% of battery pack.

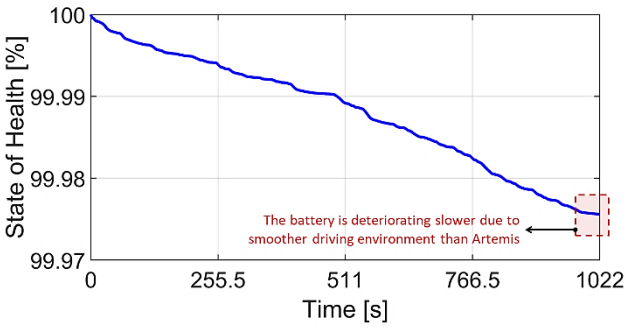

(d) WLTP-class 1: SoH% of battery pack.

Figure 41: Operational parameters of the storage devices for light-duty hypothetical vehicle.

Due to excessive regenerative energy in Artemis-urban cycle, the storage devices are expected to overcharge, as exhibited in Figure 41. To remedy this problem, a dedicated adjustment procedure is proposed, which adjusts the reference power of storage devices. This adjustment is exhibited in Figure 41a ($t > 560$), where the surplus regenerative energy is directed to the braking resistor according to relative violation from the allocated permissible range. However, in case of WLTP-class 1 cycle (Figure 41b), the SoC violation represented by Δ_d is zero as is the braking power, which is non-existent.

From Figure 41c, the battery ends up deteriorating faster in Artemis cycle compared to WLTP (Figure 41d). This can be attributed to the fact that Artemis-cycle is much harsh in terms of intermittent acceleration/deceleration, which impacts the battery much more than WLTP class-1 driving cycle. The overall results are presented in Table 15.

Table 15: The operational parameters of power sources for hypothetical light-duty vehicle.

Driving cycle	Sources	Remaining SoH%		Violation	SoC%		Efficiency Mean%	h_2 consumption [g]	
		SoH_i	SoH_f	(Δ_d)	SoC_i	SoC_f		/km	Total
WLTP class-1	Supercap		-	0.0	67.7	68.29	-		-
	Battery	100	99.9756		65	81.93			
	PEMFC		-	-		-	42.87	3.182	25.75
Artemis-urban	Supercap		-	0.1	67.7	86.52	-		-
	Battery	100	99.964		65	89.29			
	PEMFC		-	-		-	47.36	6.23	30.35

The major operational parameters of PEMFC stack: the hydrogen (h_2) consumption and operational efficiency are comulatively presented in Figure 42. Subsequently, the average operating efficiency and h_2 consumption/km are provided in Table 15.

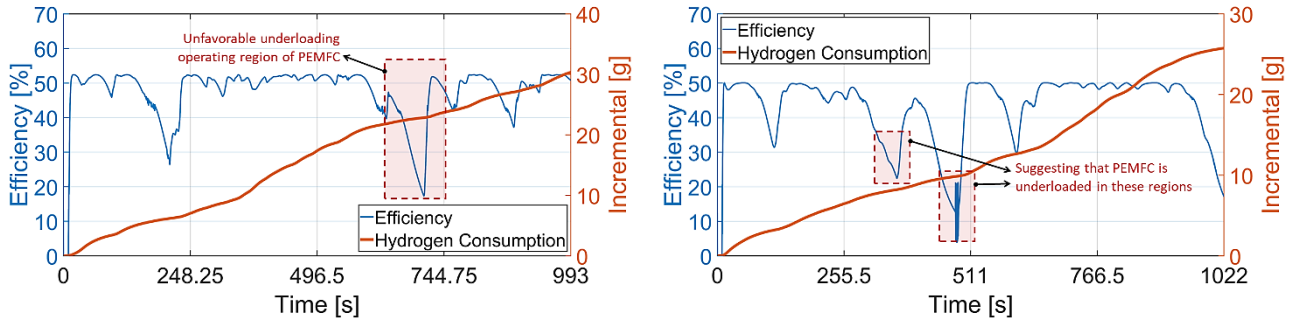

(a) Artemis-urban. (b) WLTP class-1.

Figure 42: Operational parameters of PEMFC system for light-duty hypothetical vehicle.

5.1.1.3 Stability Metrics

The state of DC link voltage is a direct indicator of the overall system's stability. In general, the greater the deviation of DC link voltage (V_o) from its designated reference (V_o^{ref}), the worse the stability is. In this context the DC link voltage profile is exhibited in Figure 43 for the studied driving cycles. It is observed that the DC link deviates more from its reference in Artemis cycle compared to WLTP-class 1, which can be attributed to a higher power demand/supply from the traction system.

$$\Delta_e{}^{dc} = \int_{t_i}^{t_f} \frac{\left|V_o^{ref} - V_o(\tau)\right|}{V_o^{ref}} d\tau \tag{63}$$

To quantize the overall violation at the end of driving cycle defined over $T_{dc} = t_f - t_i$, a statistical parameter ($\Delta_e{}^{dc}$) is introduced in (63). The obtained value of $\Delta_e{}^{dc}$ for Artemis-urban cycle is higher than that for WLTP-class 1 cycle, which is consistent with earlier observations that DC link deviates more than its reference in Artemis cycle.

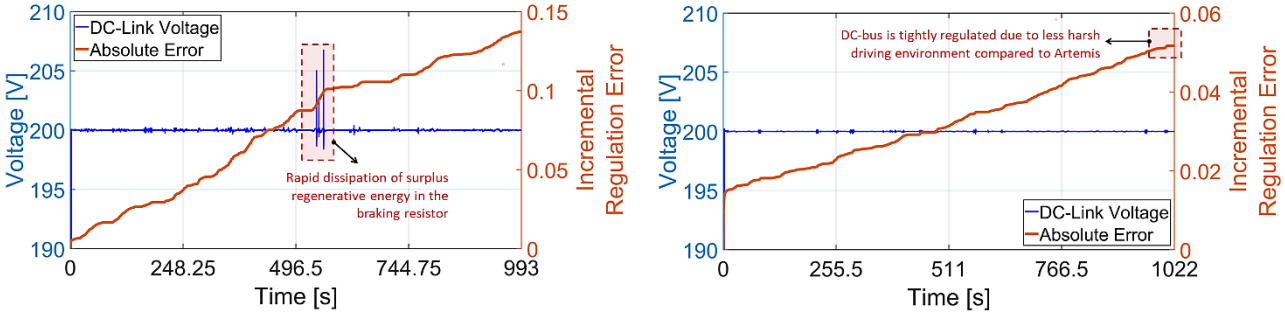

(a) Artemis-urban. (b) WLTP class-1.

Figure 43: DC bus profile and incremental regulation error for light-duty vehicle.

5.1.1.4 Optimization results

Instead of employing the static power separation rule (PSR) of conventional FSM [161, 162] and offline-tuned rule of FSM [54], the frequency-driven PSR is tuned in an online manner, which is denoted by (Ψ_{fc}^{opt}). The tuning decision is based on the instantaneous minimization of overall rationalized cost. The overall cost is the weighted sum of individual operational cost such as hydrogen consumption, health degaradtion, and SoC violation. So, the online-tuned rule PSR should theoretically provide an adequate and controlled trade-off between the considered objectives. In this context, the frequency-map of online-tuned PSR is presented in Figure 44 (a, b) for the studied driving cycles. Subsequently, the map of overall rationalized cost corresponding to online-tuned PSR is provided in Figure 44 (c, d). In comparison with the established approaches (static and offline-tuned), the online-tuned rule facilitates online minimization of overall-cost, which inturn results in reduced hydrogen conumption and sources degradation. Insequence, Figure 44 (e, f) exhibits the frequency-map of PSR with minimization preference given to individual operational objectives ($\Upsilon_{\{h_2,fc,b,SoC\}}$), in addition to overall rationalized cost (Υ_t).

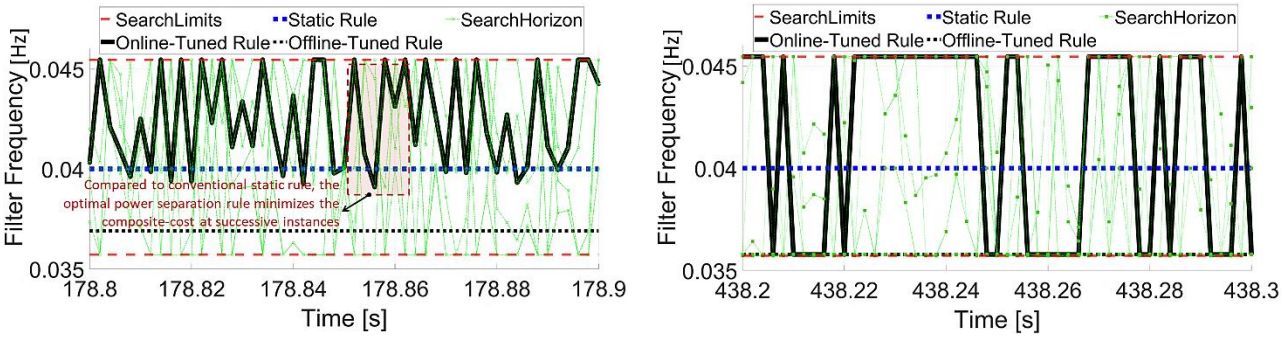

(a) Artemis-urban: Power separation rule. (b) WLTP-class 1: Power separation rules.

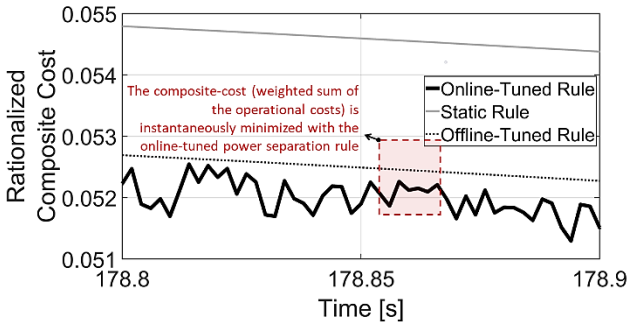

(c) Artemis-urban: Overall rationalized cost.

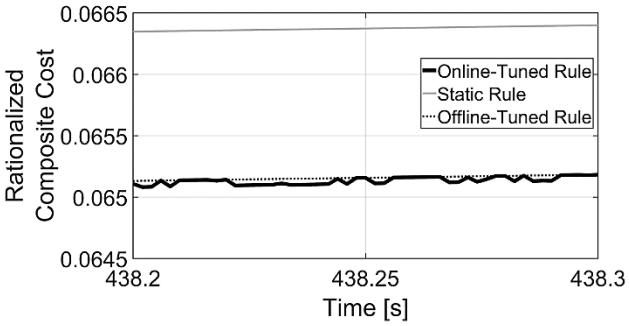

(d) WLTP-class 1: Overall rationalized cost.

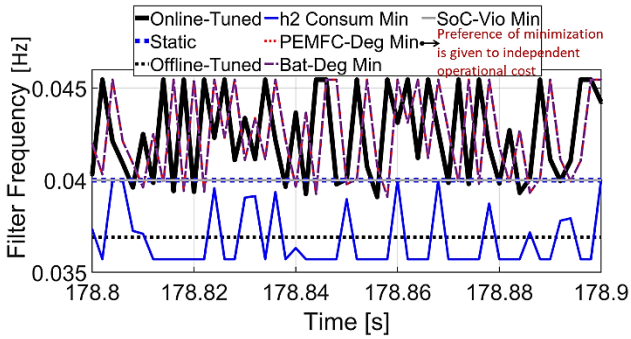

(e) Artemis-urban: Rule with minimization of distinct operational criterion.

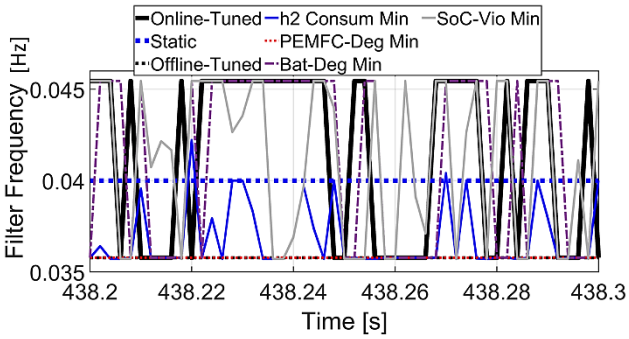

(f) WLTP-class 1: Rule with minimization of distinct operational criterion.

Figure 44: Optimization results for hypothetical light-duty FCHEV.

The total rationalized cost and the associated objectives against the online-tuned rule are depicted in Figure 45. These elements respectively include the hydrogen consumption cost (Υ_{h_2}), sources degradation costs ($\Upsilon_{\{fc,b\}}$), and SoC violation cost (Υ_{SoC}) associated with the optimal-filter. Conclusively, the overall rationalized cost is higher in Artemis-urban cycle than that for WLTP-class 1 driving cycle. Another important factor is the absence of SoC violation cost in WLTP cycle compared to Artemis, which matches with the corresponding SoC profiles.

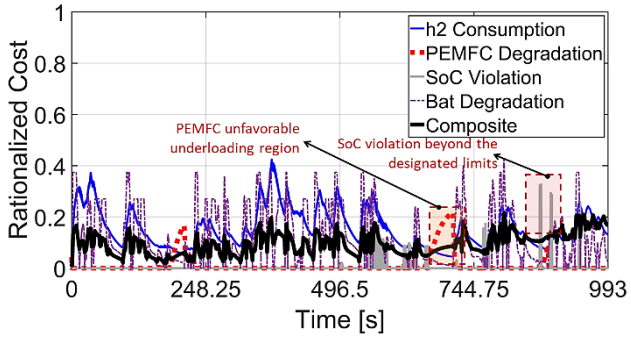

(a) Artemis-urban.

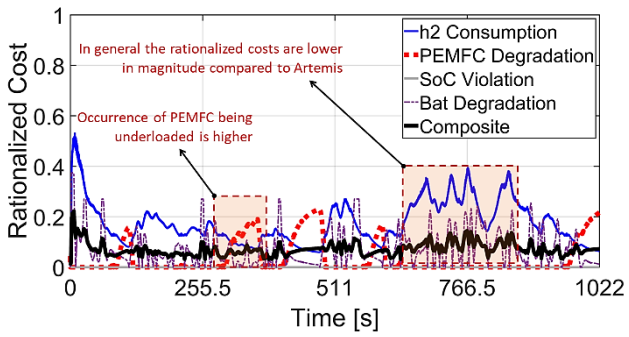

(b) WLTP class-1.

Figure 45: Individual rationalized costs for light-duty hypothetical vehicle.

The statistical analysis of the optimization results with respect to individual operational costs is conducted and associated results are presented in Table 16 (for Artemis-cycle). As expected, the online-tuned rule with minimization preference given to a particular operational parameter provides the best results in terms of optimization (for that particular objective only [green] and may be worse [red] or suboptimal for others).

Table 16: Statistics related to the operational parameters of light-duty hypothetical vehicle.

Competing PSR for Artemis-cycle [Hz]		Operation parameters (Mean rationalized costs)				
		Overall rationalized Υ_t	h_2 consumption Υ_{h_2}	PEMFC degradation Υ_{fc}	Battery degradation Υ_b	SoC violation Υ_{SoC}
Minimization preference	Overall rationalized cost	0.0973	0.158	0.0113	0.1331	0.0028
	h_2 consumption cost	0.1008	0.1531	0.0178	0.1331	0.099
	PEMFC degradation cost	0.0999	0.1675	0.011	0.134	0.0044
	SoC violation cost	0.0999	0.1674	0.0115	0.134	0.0011
	Battery degradation cost	0.1018	0.1667	0.0151	0.1312	0.0522
Offline-tuned FSM [54]		0.1017	0.1677	0.0135	0.1339	0.0918
Conventional/static FSM [161, 162]		0.1045	0.1683	0.0154	0.1332	0.101

The minimization preference given to the overall rationalized cost seems the best compromise [highlighted grey] to provide overall satisfactory optimization performance (at least in the studied driving environments). These statistical findings facilitate a crude trend toward the improvements, which can be expected from the proposed optimal filter in terms of achieving the vehicle operational objectives.

5.1.2 Case-study B*: Mid-size hypothetical vehicle*

To increase the diversity and in order to prove the general adequacy of the proposed methods, a mid-size hypothetical vehicle (parameters given in Appendix A: Table 27) is added as the candidate test system. The selective results corresponding to mid-size hypothetical vehicle are presented in the subsequent sections. To match with the characteristics of the mid-size passenger vehicle, a challenging driving cycle with mixed characteristics is selected, and subsequently examined in detail. The profile of the LA92 driving cycle is presented in Figure 46. Pattern-wise the studied cycle can be essentially classified as an inter-city/urban driving environment with harsh acceleration/deceleration behavior. However, unlike Artemis-urban cycle previously studied for light-duty vehicle, the LA92 cycle requires a higher cruising speed ($\geq$ $100 km/h$) which mimics the suburban/highway nature, but within the city. These distinct characteristics portray LA92 as a driving cycle worth considering, particularly for the passenger vehicles (like a taxicab).

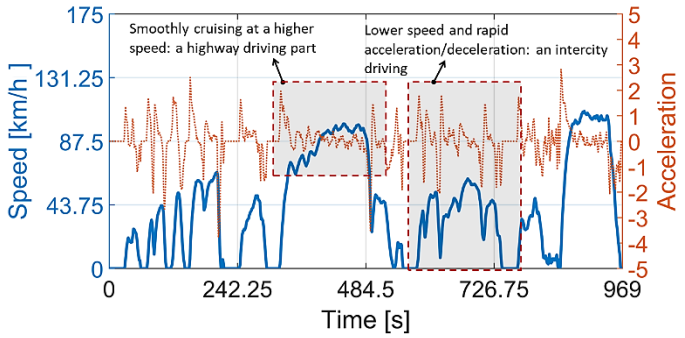

Figure 46: Profile of LA92 driving cycle.

5.1.2.1 Operational parameters with optimally selected configuration

After the application of the proposed sizing procedure, the optimal configuration for the energy sources of mid-size hypothetical vehicle is presented in Table 17. The selected powertrain config is expected to facilitate an adequate compromise among key operational objectives and the associated price, especially for the driving cycles similar to LA92. The power distribution/balance among optimaly selected energy sources of hypothetical mid-size FCHEV is exhibited in Figure 47 for the LA92 driving cycle. Conclusively, the low frequency components of traction power are appropriately allocated to PEMFC stack, dictated by the online-tuned rule Ψ_{fc}^{opt}.

Table 17: Final configuration of the power sources of hypothetical mid-size vehicle.

Driving cycle	Coefficients		Energy source		
	Δ_{fc}	Δ_{doh}	PEMFC $[kW]$	Battery $[kWh]$	Supercap $[F]$
LA92	0.75	0.75	27 kW	6.51	21.28

The residual load is essentially balanced by the composite ESD, as the highest frequency components of residual load (peaks) are met by supercap, matching its intrinsic response. The battery, thereafter facilitates the global power balance by supporting moderate frequency components of the traction load.

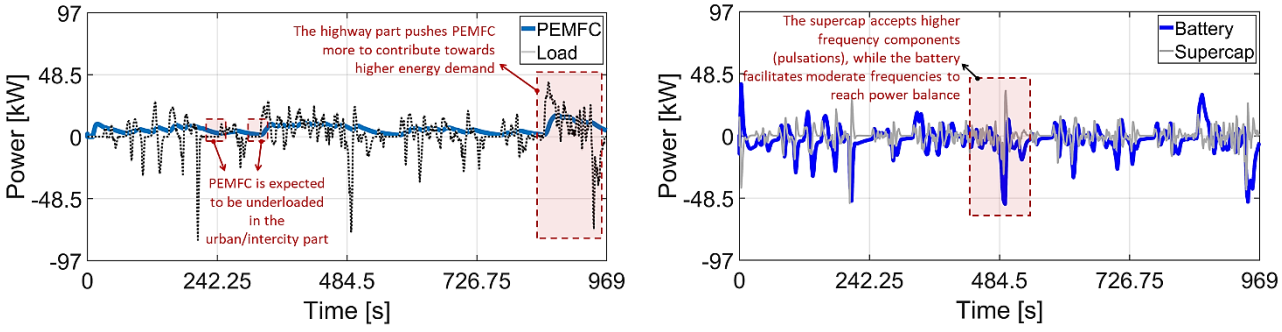

(a) Load and PEMFC.

(b) Battery and supercap.

Figure 47: Power balance for the hypothetical mid-size vehicle.

Since, the battery supports moderate frequency elements of the traction load, the probability of overcharging inturn is expectedly higher, as depicted in Figure 48a. However, the SoC of battery pack is not exceeded beyond its soft violation limits, therefore the proposed droop adjustment procedure is not triggered.

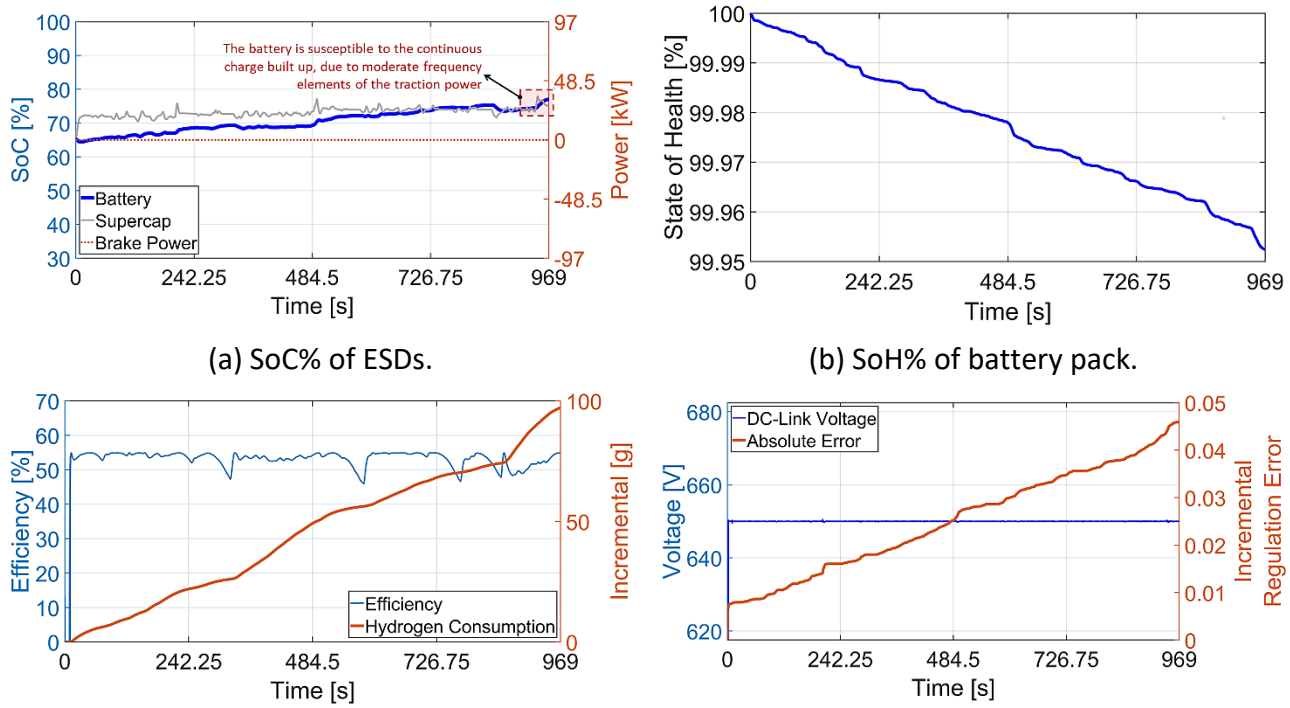

(a) SoC% of ESDs.

(b) SoH% of battery pack.

(c) PEMFC system.

(d) DC-bus profile.

Figure 48: Operational parameters of the mid-size hypothetical vehicle.

Accordingly, the power directed towards braking resistor is non-existent and the SoC violation represented by Δ_d is zero. The SoH% profile of the battery pack subject to LA92 driving cycle is presented in Figure 48b. Subsequently, the statistics related to operational parameters of storage devices are presented in Table 18. The waveforms of hydrogen (h_2) consumption and operational efficiency of PEMFC system are comulatively presented in Figure 48c. Subsequently, the average operating efficiency and h_2 consumption/km are provided in Table 18.

Table 18: The operational parameters of power sources for hypothetical mid-size vehicle.

Driving cycle	Sources	Remaining SoH%		Violation	SoC%		Efficiency Mean%	h_2 consumption [g]	
		SoH_i	SoH_f	(Δ_d)	SoC_i	SoC_f		/km	Total
LA92	Supercap	-		0.0	67.7	74.94	-	-	
	Battery	100	99.952		65	77.02			
	PEMFC	-		-	-		52.71	8.635	97.14

The DC link's voltage profile being the essential stability parameter is exhibited in Figure 48d for LA92 cycle. For the driving cycles (nature and requirements-wise), the proposed control scheme provides satisfactory performance in terms of overall system stability and DC link's regulation.

5.1.2.2 Optimization results

The frequency-map of the online-tuned PSR (Ψ_{fc}^{opt}) by giving minimization preference to the overall-rationalized cost (Υ_t) is presented in Figure 49a for LA92 cycle. For the purpose of comparative study, the conventional variant of FSM with static rule [161, 162] and offline-tuned FSM [54] are adopted. Consequently, the map of overall rationalized cost corresponding to the competetive PSR is provided in Figure 49b. It can be observed that in comparison with the established approaches, the online-tuned rule facilitates online minimization of overall-cost, which inturn results in reduced hydrogen conumption and sources degradation.

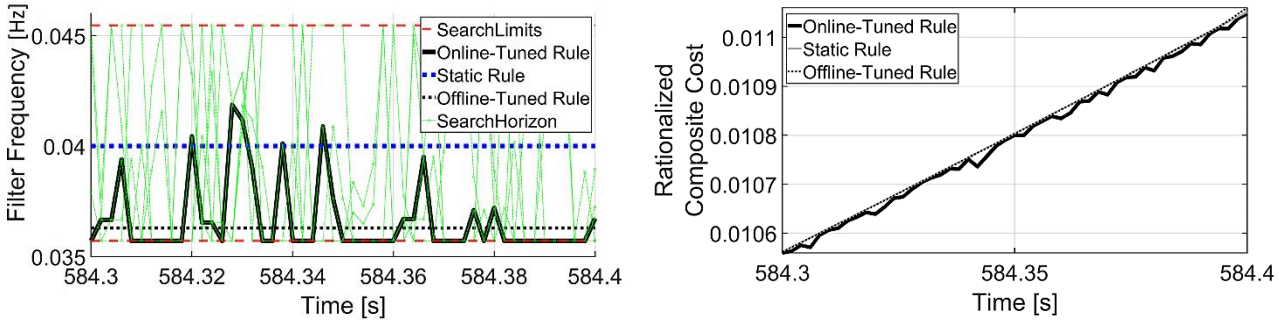

(a) Power separation rules. (b) Overall rationalized cost.

Figure 49: Optimization results for the hypothetical mid-size FCHEV.

The statistical analysis of the optimization results with respect to competitive methods are presented in Table 19. The optimal rule with minimization preference given to overall rationalized cost [highlight grey] provides the most appropriate compromise in terms of optimization (improvements indicated by [green] and worse/suboptimal solutions indicated by [red]). These statistical findings facilitate a crude trend toward the improvements, which can be expected from the proposed approach, in comparison to the conventional and offline-tuned methods.

Table 19: Statistics related to the optimization parameters of mid-size hypothetical vehicle.

LA92 driving cycle	Operation parameters (Mean rationalized costs)				
	Overall rationalized Υ_t	h_2 consumption Υ_{h_2}	PEMFC degradation Υ_{fc}	Battery degradation Υ_b	SoC violation Υ_{SoC}
Online-tuned FSM [proposed]	0.0392	0.1104	0.0	0.0465	0.0
Offline-tuned FSM [54]	0.0420	0.1220	0.0	0.0463	0.0
Conventional/static FSM [161, 162]	0.0423	0.1226	0.0001	0.0464	0.0

5.1.3 Case-study C: *Commercial-scale passenger vehicle*

A commercial-scale FCHEV (parameters and specifications matched with those of a commercial vehicle-Toyota Mirai [137]) is analyzed to validate the applicability of the proposed methods.

5.1.3.1 Standard config and powertrain topology

The powertrain topology and system configuration being considered are the standard ones, which are rigorously presented in the literature as well [137]. Therefore, no dedicated sizing procedure is conducted for the commercial-scale vehicle. The studied power-layout and the system configuration are respectively presented in Figure 50 and Appendix E: Table 31.

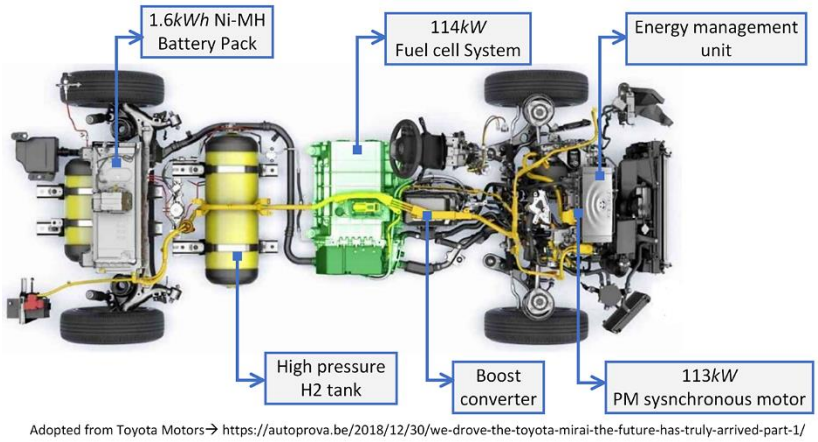

Figure 50: Power-layout of the studied commercial-scale FCHEV [137].

To study the possible impacts and applicability of the proposed OEMS for the case of commercial-scale vehicle, a classical highway/motorway driving cycle is considered, and the driving profile is presented in Figure 51. Even the small changes in the acceleration/braking at a higher cruising speed cause large spikes in the power being demanded/provided by traction system: indeed, a challenging scenario for an online optimization-based EMS. Therefore, the Artemis-motorway driving cycle is an adequate candidate to analyze the performance of commercial-scale vehicle under the influence of the proposed OEMS.

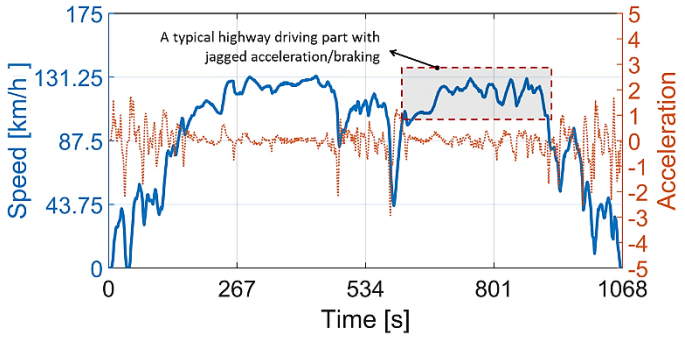

Figure 51: Profile of Artemis-motorway driving cycle.

5.1.3.2 Operational parameters

The power distribution waveforms for the commercial-scale FCHEV are exhibited in Figure 52 (a, b). Initially, the load profile and PEMFC power profile are comulatively presented in Figure 52a. It can be observed that the PEMFC system tightly follows the traction load, as dictated by the frequency-driven PSR. Unlike, the previous case studies of hypothetical vehicles, the PSR is tuned to provide the maximum portion of traction power via PEMFC, whereas the comparatively smaller battery system participates only to reach global power balance. In context, the battery profile alongwith braking (power loss) are jointly presented in Figure 52b. The proposed power distribution scheme matches with the load-following control present in the Toyota Mirai [137].

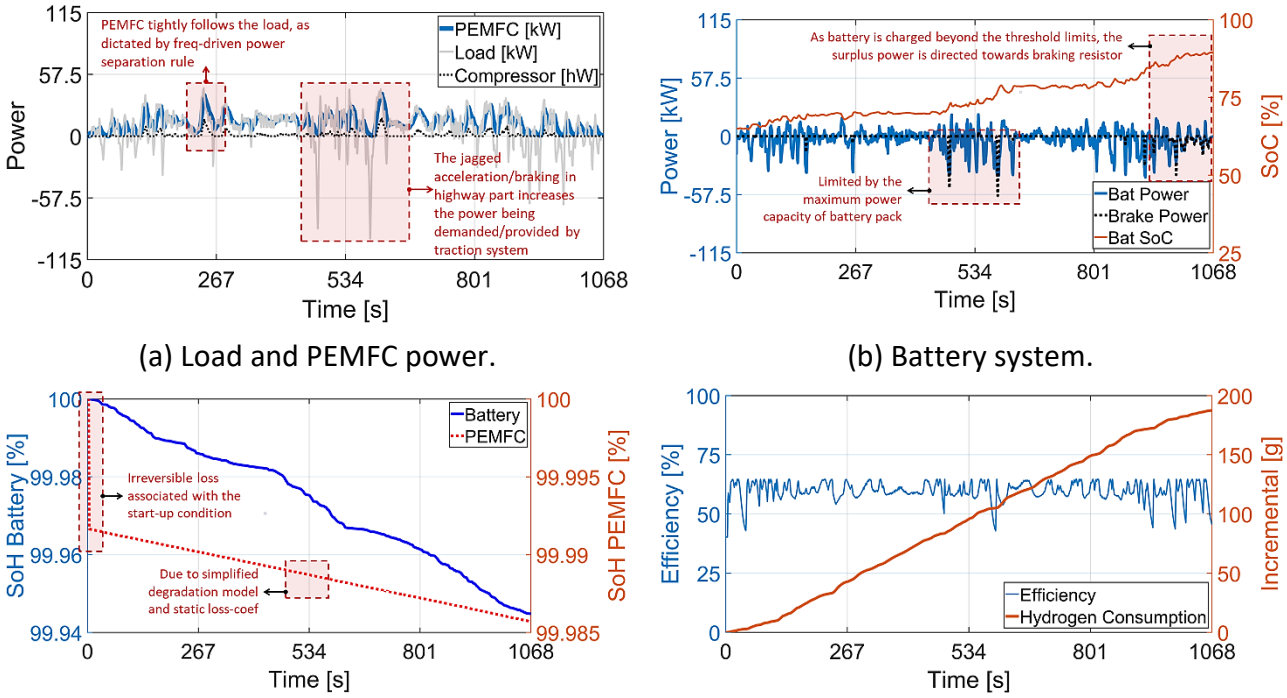

(a) Load and PEMFC power.

(b) Battery system.

(c) SoH% of power sources.

(d) PEMFC system.

Figure 52: Power balance and operational param for the commercial-scale passenger vehicle.

The expected remaining SoH% of power sources is presented in Figure 52c. Due to the static (and computationally simple) degradation model of PEMFC stack, the expected lifespan decreases in a linear fashion, which was expected due to the simplicity of assumed model. The batteries lifespan decreases in a nonlinear fashion as exhibited in Figure 52c. Finally, the operating efficiency and hydrogen consumption are presented in Figure 52d.

The statistics related to the key operational parameters of energy sources are respectively presented in Table 20 for the battery pack and the PEMFC system. The net statistics depict the general feasibility and adequacy of the proposed OEMS for vehicles with parameters and specifications similar to a commercial vehicle.

Table 20: Power sources parameters for the commercial-scale vehicle.

Driving cycle	Sources	Remaining SoH%		Violation	SoC%		Efficiency	h_2 consum. [g]	
		SoH_i	SoH_f	(Δ_d)	SoC_i	SoC_f	Mean%	/km	Total
Artemis-Motorway	Battery	100	99.945	0.0340	65	89.47	-	-	
	PEMFC	100	99.985	-	-		59.65	6.52	187.43

5.1.3.3 Online-tuned power separation rule

The frequency-map of the online-tuned rule (Ψ_{fc}^{opt}) by giving minimization preference to overall-rationalized cost (Υ_t) is presented in Figure 53a. The frequency-driven rule adapts in a way to keep the overall rationalized cost as minimum as possible. In sequence, the constituent operational costs corresponding to adaptive rule are presented in Figure 53b.

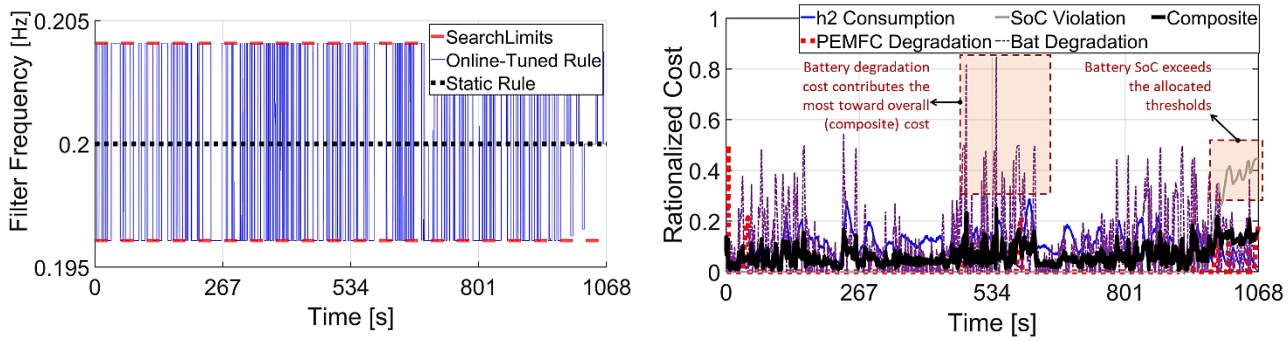

(a) Online-tuned power separation rule. (b) Overall rationalized costs.

Figure 53: Adaption of power separation rule for the commercial-scale FCHEV.

5.1.4 Case-study D: *Assessment in the real driving data*

To evaluate the performance of hypthetical FCHEVs in the actual scenarios, the European Transient Cycle (ETC) based on the real road driving measurments (Figure 54) is adopted. The ETC driving cycle is collected by the FIGE Institute, Aachen Germany [172]. It contains there different parts (urban, rural and highway), equally divided over the span of 1800*s*.

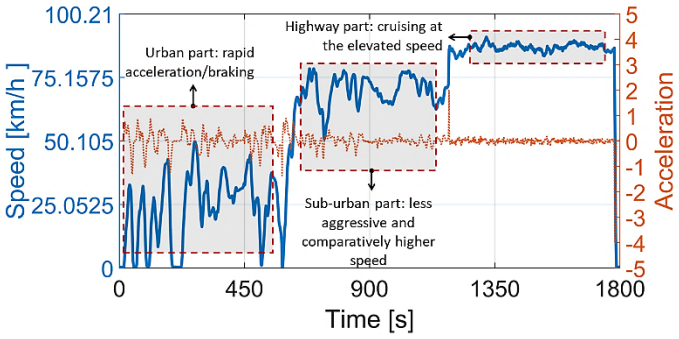

Figure 54: ETC FIGE-4 driving cycle [172].

5.1.4.1 Operational parameters and performance analysis

To investigate the performance under the influence of ETC driving cycle, the light-duty hypothetical vehicle is studied as the candidate platform (the characteristics and specification match with each other). The corresponding power waveforms are presented in Figure 55 (a, b). It can be observed that for the sub-urban interval (600<t<=1200) and highway interval (1200<t<=1800), the PEMFC provides the low frequency component of the traction power, which corresponds to the continuous and steady power (and operation) of PEMFC system.

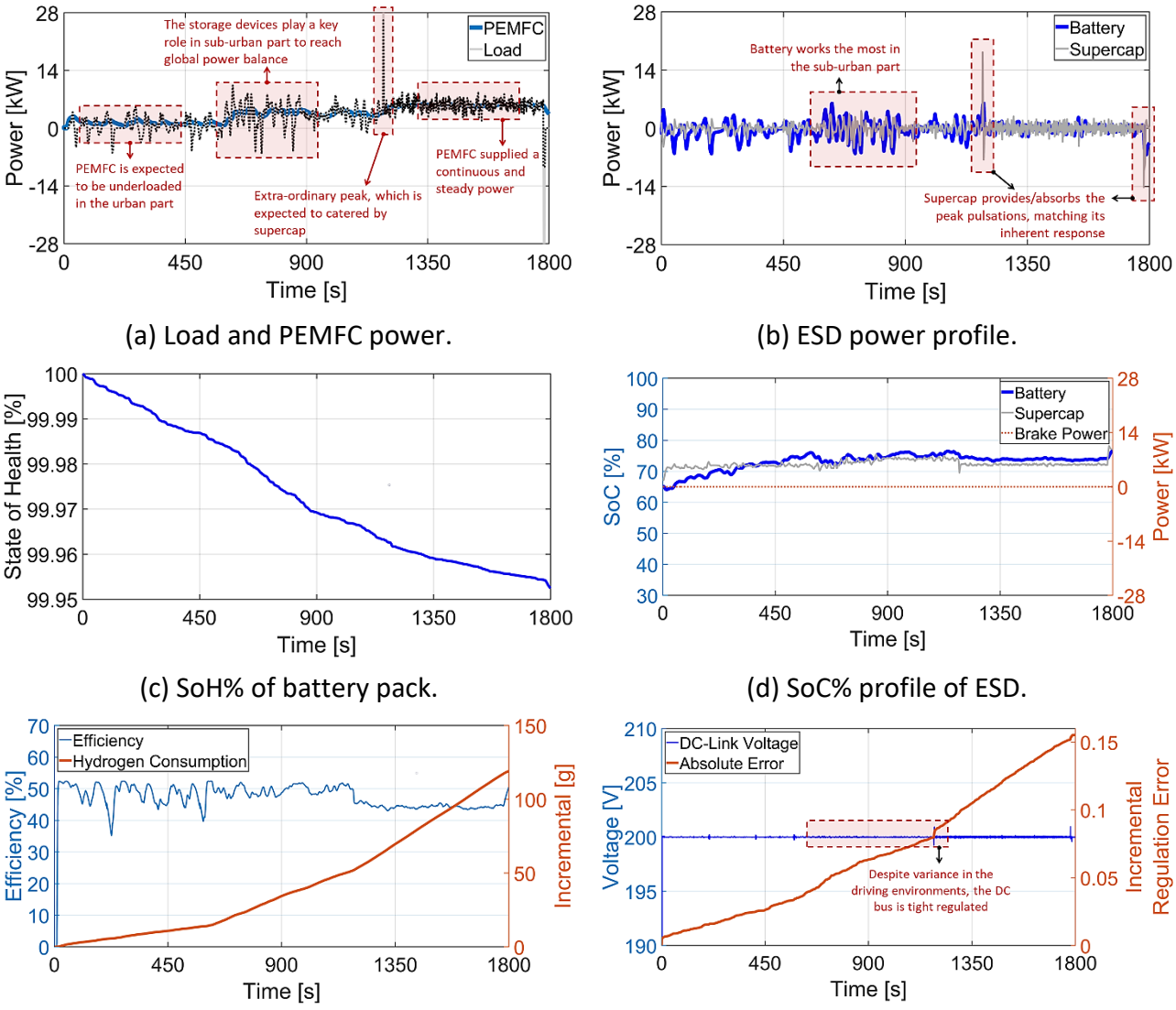

(a) Load and PEMFC power.

(b) ESD power profile.

(c) SoH% of battery pack.

(d) SoC% profile of ESD.

(e) PEMFC system

(f) DC-bus profile stabilization

Figure 55: Performance parameters of light-duty vehicle in ETC FIGE-4.

Subsequently, the storage devices assist to reach the global power balance. Particularly, two major attributes are witnessed: the supercap facilitates highest frequency component (especially the peak pulsations), and the battery in turn supports moderate frequency component (delayed

peaks) to meet the residual power demand. Therefore, with this strategy, it is expected that the battery pack will reach its overcharging limits with time, though the proposed droop-scheme is expected to trigger in this scenario by directing the surplus regenerative power towards braking resistor. From the urban driving interval (0<t<=600), the probability of PEMFC being underloaded is higher, which would expectedly degrade the PEMFC at a comparatively faster rate.

Figure 55 (c, d) correspond to the key operational parameters of storage devices such as SoH% of the battery pack and SoC% of the storage devices. From Figure 55d, the storage devices contribute equally during the highway interval (1200<t<=1800), therefore no persistent charge buildup is present in the highway part.

Finally, the time-based operational parameters of PEMFC system (incremental hydrogen consumption and operating efficiency) are jointly presented in Figure 55e, and subsequently the Figure 55f depicts the effectiveness of the proposed control techniques in terms of maintaining the DC link's voltage within its intended regulation range.

The net statistics related to the power sources of light-duty hypothetical FCHEV under the influence of ETC cycle are tabulated in Table 21. In this context, initially the expected remaining SoH% of battery pack, the net violation in SoC% of the storage devices in relation to the soft thresholds, and SoC% at the end of driving cycle are presented. It can be observed that, as no surplus charge buildup is present in ETC driving cycle, therefore the net violation (Δ_d) is zero. In the follow up, the key operational parameters such as its mean operating efficiency, and the hydrogen consumption (summed up over whole ETC cycle and translated to /km) are also tabulated in Table 21.

Table 21: Operational parameters of light-duty vehicle in ETC FIGE-4 cycle.

Driving cycle	Sources	Remaining SoH%		Violation	SoC%		Efficiency Mean%	h_2 consumption [g]	
		SoH_i	SoH_f	(Δ_d)	SoC_i	SoC_f		/km	Total
ETC FIGE-4	Supercap	-		0.0	67.7	77.1	-	-	
	Battery	100	99.951		65	76.73			
	PEMFC	-		-	-		47.16	4.037	119.06

5.1.5 Summary of numerical simulations

The overall expected %reductions obtained with the proposed OEMS based on online-tuned FSM (compared to offline-tuned FSM[54] and static FSM[161, 162]) are commutatively presented in Figure 56. Here, the results are only exhibited for hypothetical Light-duty and Mid-size vehicles, just to reflect the expectancy of the %improvements at the proposed OEMS side. It can be observed that the proposed OEMS based on online-tuned FSM can provide reasonable %reductions in the rationalized overall cost. For the comparison purpose, the conventional OEMS based on static FSM is used as a baseline. The proposed online-tuned FSM can provide up to 4.33% and 7.33% reductions (in the studied driving cycles) in minimizing the overall rationalized cost, when

compared with the baseline. These %reductions are equally reflected towards individual operational costs as well, as exhibited in Figure 56. Moreover, the %improvements also present a crude trend towards actual fuel savings and sources lifespan improvements in the real-time scenarios, as well as other driving conditions/environments.

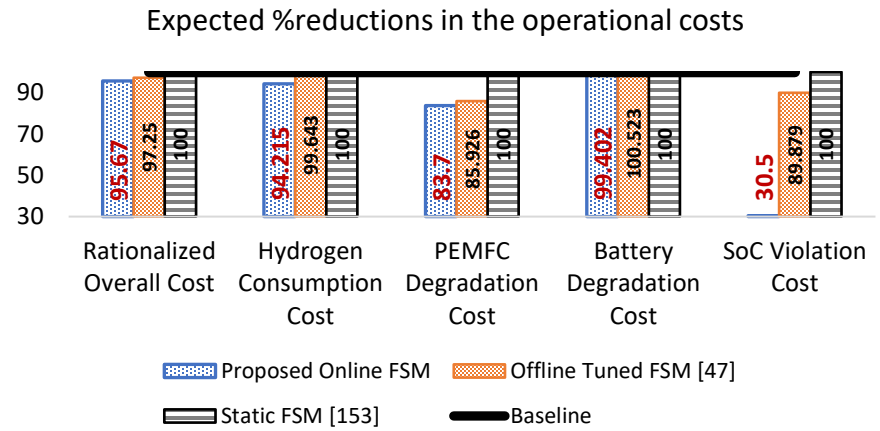

(a) Light-duty hypothetical vehicle (Artemis-urban cycle).

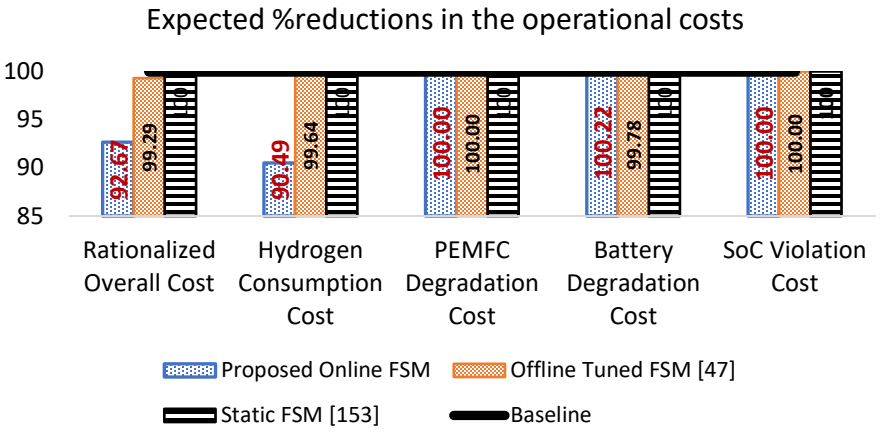

(b) Mid-size hypothetical vehicle (LA92 cycle).

Figure 56: Expected %reductions in the operational costs with the proposed OEMS.

5.2 Experimental work

Several small-scale experimental studies are conducted using the test-benches provided by FCLab and Segula Technologies. The experimental findings give critical insight towards the expected behavior of several power components (such as PEMFC and battery-packs, which are suitable for HEVs), especially under the influence of real-time conditions. Moreover, a small-scale hybrid power system is built for vehicular applications, with the aim to validate the practical applicability of the proposed OEMS. This is in context to studying various design and control related aspect of FCHEVs. The details of these experimental work and corresponding results are presented in the subsequent sections.

5.2.1 Parallel connected converters for fuel cell based vehicular applications

The PEMFC stack is usually termed as a low voltage and high-power device with nonlinear soft characteristics i.e., the voltage across the stack decreases in a nonlinear fashion with the current being drawn from it. Due to the soft nature of PEMFC stack, it is essential to interface the stack with the traction load (inverter system connected with an electric motor) via Boost converter. This is especially true for the vehicular applications, where the tight regulation of DC-bus via Boost converter can facilitate smooth and reliable operation of the inverter-motor subsystem.

Given the importance of this design related topic, an experimentally validated power conversion stage based on parallel connected Boost converters is proposed. An effective physical-components-assisted approach is suggested, which essentially consists of a passive equalization filter to facilitate equal and safe power sharing between the parallel connected Boost converters. The whole study is divided in the two steps: first with the emulation of programmable sources [22], and second with the real components.

5.2.1.1 Emulation with programmable components

The first part of the experimental study is performed with the programmable source and an electronic load. The proposed topology based on emulation components is presented in Figure 57. In essence, the topology contains: (i) a low-voltage (LV) and high-power (HP) source to mimic the operation of PEMFC stack, (ii) the parallel connected boost converters (PCBR), (iii) the passive equalization filter with passive components (LCEF), (iv) and an electronic load. Here, the control signals [UVP; DC; OCP] respectively correspond to under-voltage protection, tempering port for the duty-cycle, and over-current protection.

The description and specifications of the test-bench components are tabulated in Table 22. The component 'passive equalization filter (LCEF)' is subdivided in the passive components (inductors/capacitors), and the power diodes to provide functionality of free-wheeling (FWD) and reverse blocking (RBD).

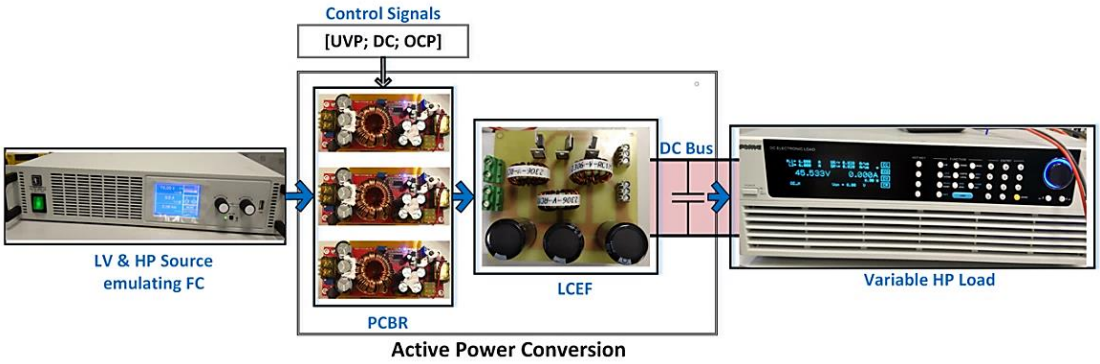

Figure 57: The proposed PCBR topology with the emulation components.

Table 22: Description and specifications of the emulation setup.

Stage	Components	Rating/Model
LV and HP Source	Programmable power supply	EA-PSI 9080 (80V-120A)
Power Processing	Boost converters	1800W, 40A
Filter circuit	Power diodes (FWD and RBD)	RHRP 3060D
	Self-inductors	2700uH
	Filter capacitors and DC bus	4700uF
Variable HP Load	Electronic load	Chroma 63203A

To explore the performance of the proposed power conversion stage and LCEF, two separate test conditions are extensively explored (presented in Table 23). The Test-1 conditions are set to validate the performance at a constant load but variable input conditions (variable power source). In contrast, the Test-2 examines a variable loading condition, while keeping the source at a constant value. The proposed Test conditions provide a better understanding of the proposed solution, in terms of real-time application.

Table 23: Description and composition of the tests being performed.

		LV programmable source	HP electronic load
Test-1 conditions	State	Variable	Constant
	Variation/Value	16V→8V	6A
Test-2 conditions	State	Constant	Variable
	Variation/Value	16V	2A→12A

The pictorial diagram of the complete test-bench is depicted in Figure 58. Subsequently, the results of Test-1 are presented in Figure 59a, which associate with the variable source voltage.

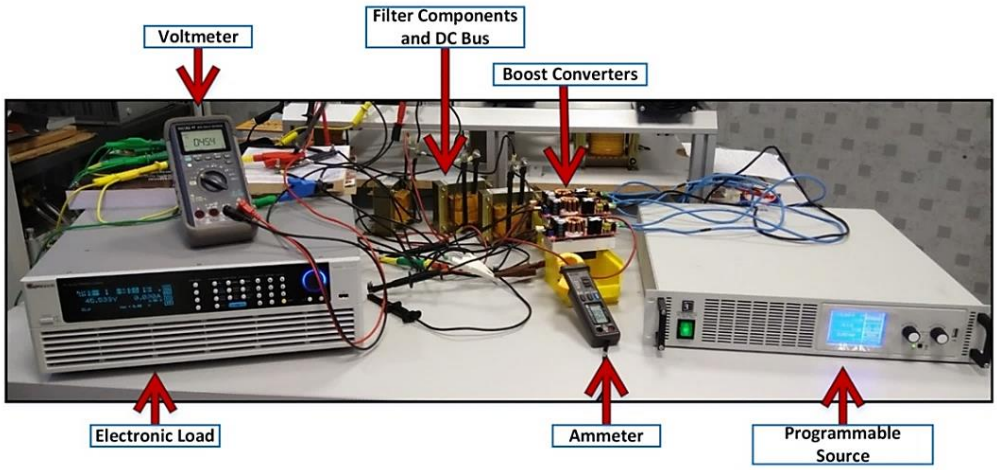

Figure 58: The emulation-based test-bench.

From Figure 59a, the proposed power conversion stage is efficacious in terms of equal power sharing among parallel connected converters (the load current is equally shared among the

parallel connected converters). It can also be clarified that with the stepwise decline in the source voltage (16V→8V), and the constant load current (6A), the source side current monotonically increases in the same manner (16A→36A). However, this does not significantly impact the global electrical efficiency of the proposed power stage on whole, which is reduced only by 11% over the whole testing range, especially operating at a very low source voltage (8V). Overall higher operating efficiency can be attributed to the lesser electrical losses (W), due to nearly equal load-power sharing among PCBR. The proposed power stage base on PCBR and LCEF facilitates equivalent power sharing strategy, thereby depicting its feasibility and applicability for PEMFC based LV-HP applications.

The Figure 59b depicts the readings for Test-2 with the variable load (2A→12A) and fixed source voltage (16V). Here, a stepwise increasing load results in similar increase for source side current (8A→38A), which is mutually shared by PCBR due to the proposed control strategy and LCEF. The mutual sharing of load power reduces electrical and thermal stress on the system, thus reducing the resistive losses and enhancing the global electrical operating efficiency of the power stage.

From the obtained results, the proposed power stage and power splitting strategy based on LCEF provides nearly equal load/power sharing among the parallel connected Boost converters resulting in a higher overall electrical operating efficiency. Therefore, the proposed power stage is evidently suitable for PEMFC based stationary and mobile applications.

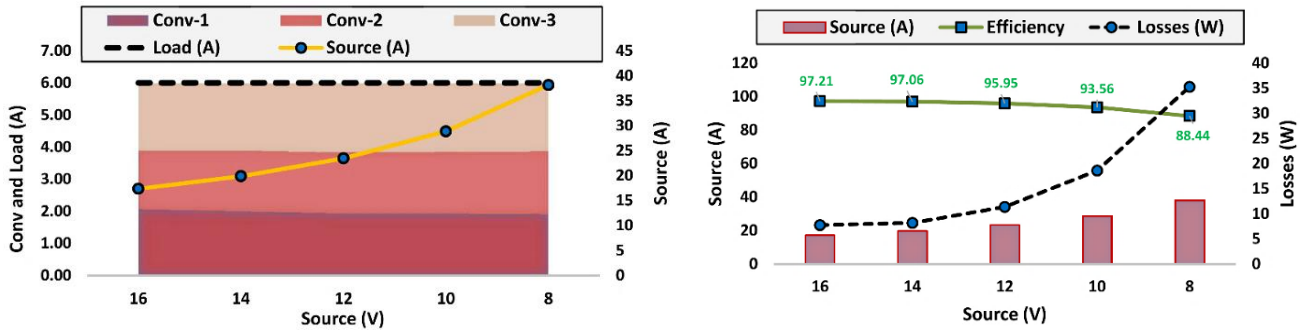

(a) Statistical readings for Test-1.

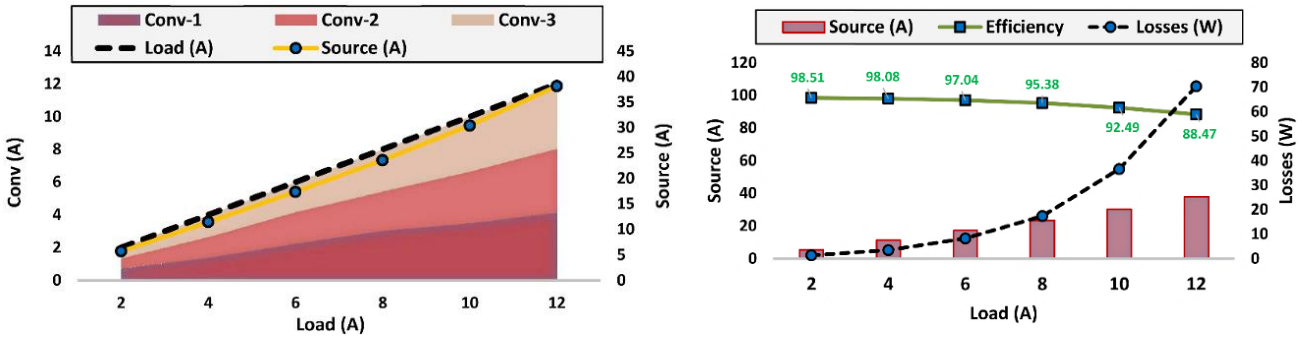

(b) Statistical readings for Test-2.

Figure 59: Reading obtained with the emulation-based test-bench.

5.2.1.2 Testing with actual components

The second part of the testing is expanded by replacing the programmable source with an open-cathode PEMFC stack (810W manufactured by Ballard) to depict the effectiveness of the passive equalization filter (LCEF) assisted load-power sharing strategy. Compared to the other types, the open-cathode stack is the simplest PEMFC system, processing air directly without the need for an air compressor or any other air conditioning unit. It reduces system cost and increases overall operating efficiency, although the power output of an open cathode unit is practically limited. In context, the studied topology is presented in Figure 60.

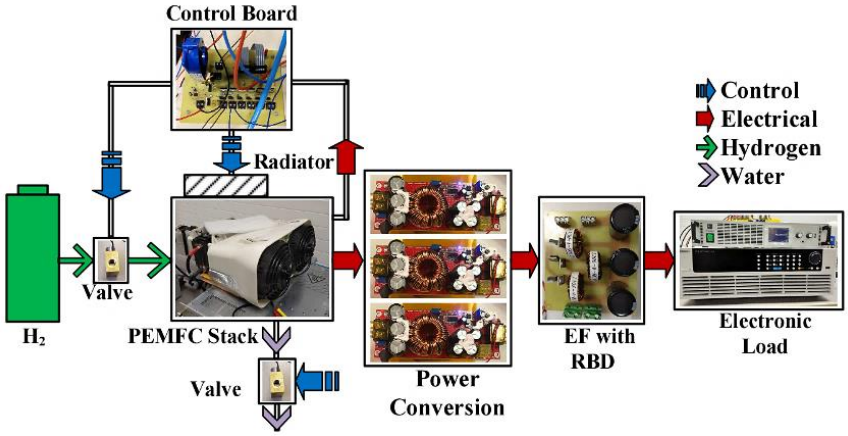

Figure 60: The proposed topology for PEMFC based high power applications.

The studied topology contains the stack itself (with cooler, electronic valves, and a control board), the power stage, the ECEF, and the electronic load. The control board serves three purposes by monitoring the demanded load power, the temperature of PEMFC stack, and the output current of PEMFC stack: (*i*) control the power supply of fuel-regulation electronic valve, (*ii*) control the power of purge-regulation valve, and (*iii*) control the power of cooling fan. The polarization relation for the tested 810W open-cathode PEMFC stack, and the overall experimental bench are commutatively presented in Figure 61.

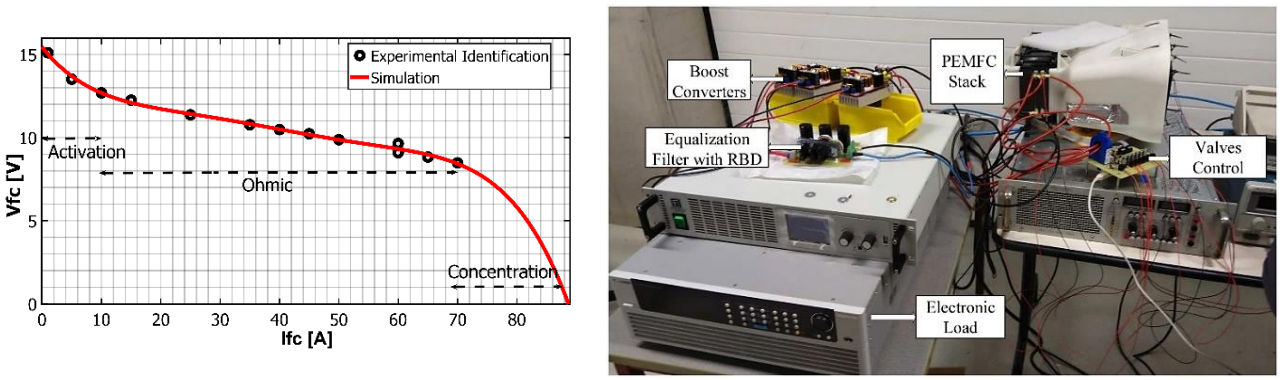

Figure 61: The polarization behavior of 810W PEMFC stack, and overall test bench.

From Figure 62, the overall electrical efficiency effectively stays between 92%-80% for the full testing range (1A→9A). The obtained electrical efficiency is expected to be higher than that of conventional power stage consisting of a unique Boost converter, particularly at the higher value of load current. The higher global efficiency is attributed to the mutual sharing of load power among parallel connected converters, which results in lower conduction losses per converter.

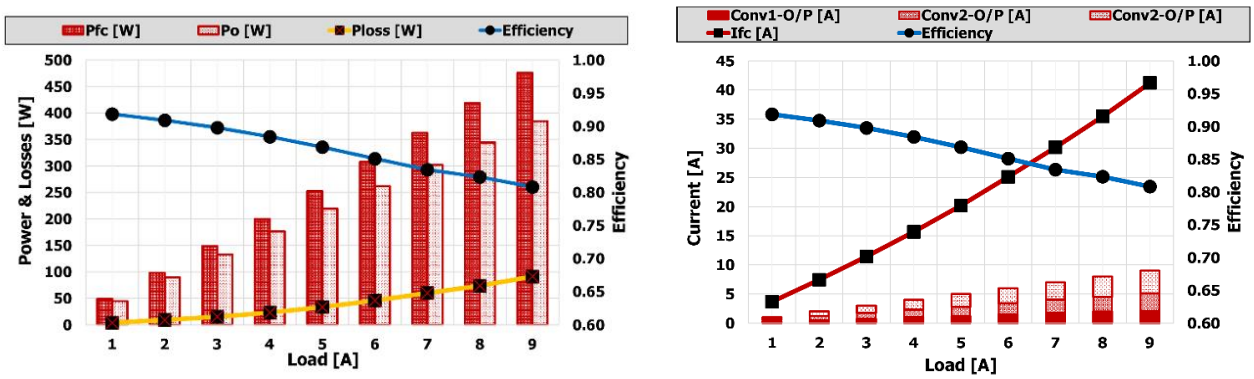

(a) Losses and efficiency (b) Current sharing

Figure 62: Reading of the test-bench obtained during exhaustive study.

5.2.2 Battery-pack characterization for vehicular applications

With the resources provided by FCLab and Segula technologies, a 48V/25Ah li-ion battery-pack is characterized in order to estimate how much driving cycles (one D-cycle presented in Figure 63) can be extracted from the given battery. This D-cycle is collected by Segula company as a representative of an actual power required by an electrified tuk-tuk vehicle. The D-cycle corresponds to 1.41 km in total (approx.) with an average speed of 24.24 km/h. The developed test-bench can be utilized under any hypothetical/real driving cycle to estimate the electrical mileage of a particular battery-pack, or to precisely size the battery-pack for intended purpose. To mimic the electrical power/current demand of the given driving cycle (Figure 63), an electronic load is effectively employed (high-power Chroma unit).

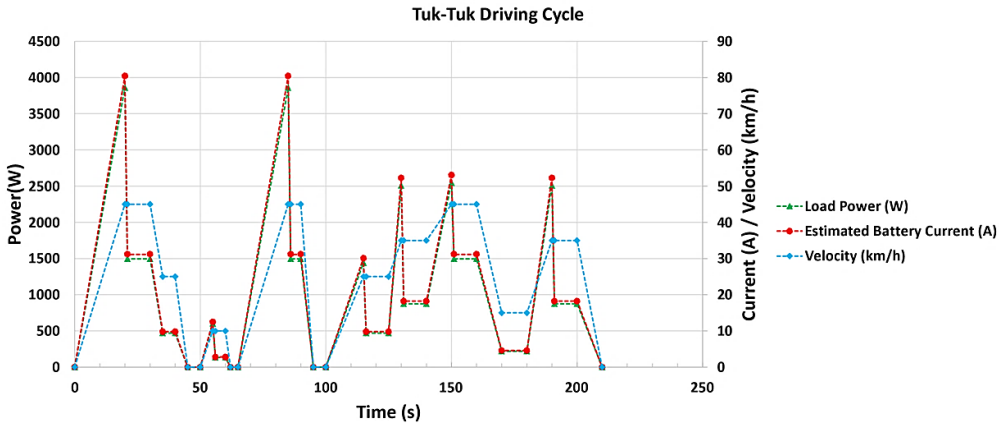

Figure 63: The Tuk-Tuk driving cycle collected by Segula technologies.

5.2.2.1 Standard characterization protocol

The provided li-ion type battery-pack is first tested with the standard charging/discharging test at different c-rates. The test is limited to maximum 1c charging/discharging due to safety reasons and limitation of the load unit used dedicatedly for this reason (RBL232-50/150/800 A/V/W max). In context, the discharging test at 0.25c and 0.5c-rates are presented in Figure 64a. Subsequently, the charging tests are provided in Figure 64b at 1c and via the provided charger (in the vicinity <=0.5c). The obtained results respectively match with that provided by the manufacturer, and therefore depict the stable operation of the examined battery-pack.

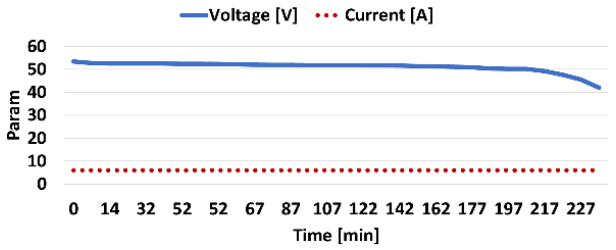

(a) Discharging at 0.25c

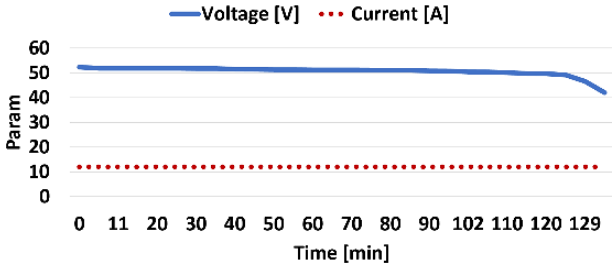

(b) Discharging at 0.5c

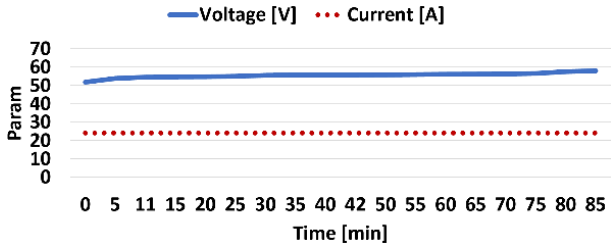

(c) Charging at 1c

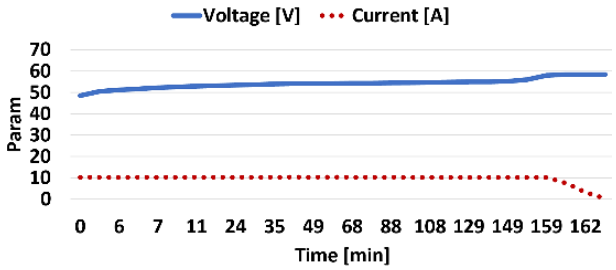

(d) Charging via the provided charger

Figure 64: Characterization of the power brick 48V/25Ah li-ion battery.

5.2.2.2 Expected electrical mileage

The driving cycle (exhibited in Figure 63) is applied over the provided battery-pack for an infinite iterative loop, until the battery-pack is fully discharged (built-in protection triggers and cutoff the battery pack at or below 40V) to estimate a rough figure of how many driving cycles can be expected from the battery-pack. However, the results are only provided for one D-cycle in Figure 65. For approximating the SoC [%], a simple linear formula was employed: at the Nominal voltage, 80% SoC was assumed; while at the cutoff voltage (triggers as the internal protection at or below 40V), 20% SoC was approximated. With the recursive testing, it was found that the given battery pack can approximately provide 29-31 continuous driving cycles, which roughly equates to an electrical mileage of 41-44 km for the given D-cycle. Alternatively, the calculations can be made to size the battery-pack according to the target mileage. The same test can further be extended for any driving cycle to estimate the net electrical mileage of a specific battery-pack.

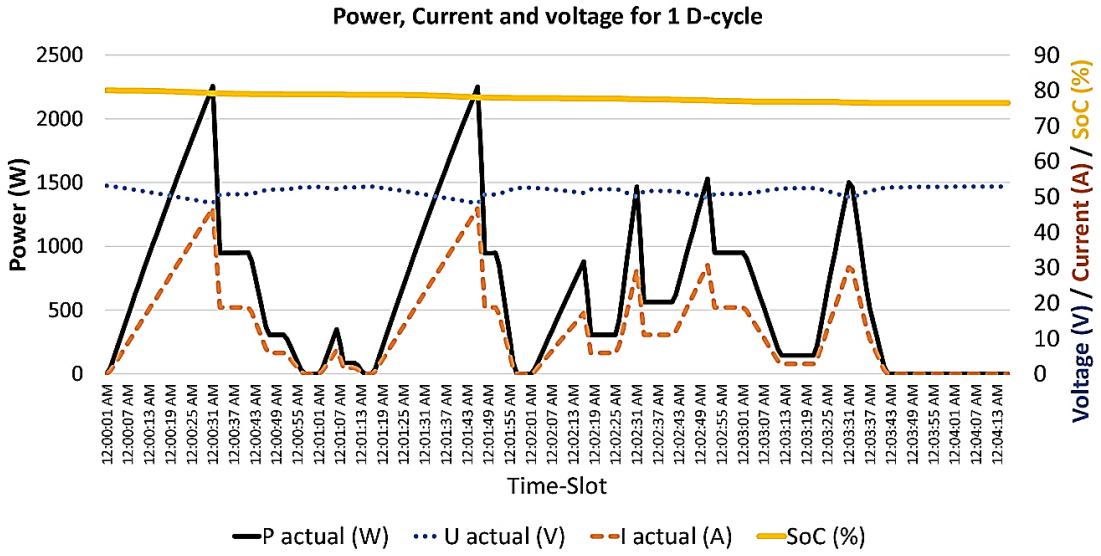

Figure 65: The response of studied li-ion battery in response to the applied D-cycle.

5.2.3 Open-cathode PEMFC system characterization

A scalable test-bench is developed by our research team to characterize the open-cathode PEMFC stack/system in context to their application in electric vehicles. The associated resources are provided by FCLab and Segula technologies. The overall test-bench is presented in Figure 66.

The bench is consisting of the open-cathode PEMFC stack, a Boost converter to regulate the DC bus voltage, an electronic load, a control desk (for data collection, regulation of cooling fan, and regulation of electronic valves), and a flow meter to measure the hydrogen consumption. Using this bench, a 24V/200W PEMFC stack was comprehensively tested under a diverse range of operating conditions and the regulation of DC-bus profile individually at 24V, 36V and 48V. However, the results are only presented for DC-bus being regulated at 48V. The details of the

major components of developed test-bench in correspondence to the characterized 24V/200W PEMFC stack are presented in Table 24.

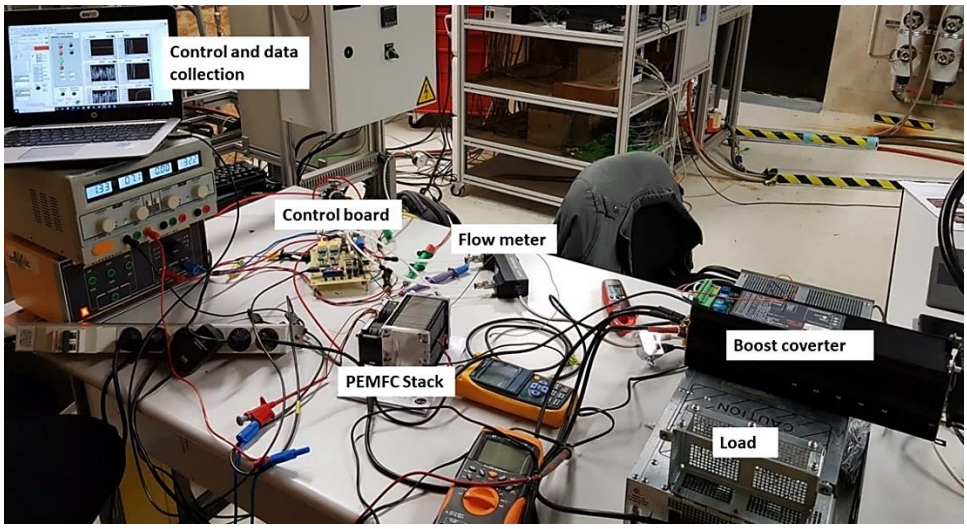

Figure 66: The test-bench for 24V/200W open-cathode PEMFC system characterization.

Table 24: Description and specifications of the test-bench for PEMFC characterization.

Components	Rating/Model
DC power supply	AL 963N (Fixed 5-12V for control board and auxiliary devices)
Open cathode PEMFC stack	Ballard 24-cells 24V/200W
Boost converter	Zahn electronics DC6350F 12V-63V
Flow meter	Bronkhorst M19201339F
Electronic load	RBL232 (50/150/800 A/V/W max)

5.2.3.1 Auxiliary devices powered through external means

For the first scenario, the 24V/200W PEMFC stack is tested under a reference load profile (stepwise over/under loading: 0A→5A→0A). The reference load profile was designed to match with the maximum permissible power output of the understudied PEMFC stack and considering that the DC-bus is regulated at 48V. Another important point to be noticed here is that the auxiliary devices including the control card, the cooling fan, and the fuel/purge-regulation valves are powered via external power supply (AL 963N), and not from the PEMFC stack.

The complete breakdown of the readings is presented in Figure 67a. The key observations are as follows: (i) the DC bus is effectively regulated at 48V, which proves the adequacy of the Boost converter and the associated onboard controller, (ii) the stack itself exhibits soft characteristics i.e., the voltage of the stack decrease in a nonlinear fashion (22V→15V) with respect to the demanded current (0A→5A at the load side). This is particularly true at the peak load, which is equivalently reflected by the difference between power supplied by PEMFC stack and power

consumed by load, and (*iii*) even though the cooling fan is supplied constant power through external means, the temperature of PEMFC stack keeps rising, though it is within the safe limits. The hydrogen consumption rate ($\dot{m}_{h_2}$) of the tested 24V/200W PEMFC stack is presented in Figure 67b, which depicts a scaled and linear relation between $\dot{m}_{h_2}$ and PEMFC current (A_{fc}). From Figure 67b, an easy-to-use polynomial fitting model is deduced and provided in (64) to approximate the hydrogen flowrate and PEMFC voltage (V_{fc}) from stack's current.

$$\dot{m}_{h_2} = -0.0193 + 0.2674 * A_{fc}$$
$$V_{fc} = 21.305 - 1.4983 * A_{fc} + 0.2169 * {A_{fc}}^2 - 0.0156 * {A_{fc}}^3 + 0.0004 * {A_{fc}}^4 \quad (64)$$

The polynomial fitting model of (64) is computationally efficient in terms of its inclusion in the OEMS of vehicle, where the reference current/power of the PEMFC stack (A_{fc}/P_{fc}) is generated as a control variable to essentially minimize the hydrogen consumption rate beyond other operational objectives. It is also noteworthy that the proposed test-bench is flexible in terms of characterizing the open-cathode PEMFC stacks with diverse range of power capacities. Though, other components such as electronic load and Boost converter should be scaled accordingly.

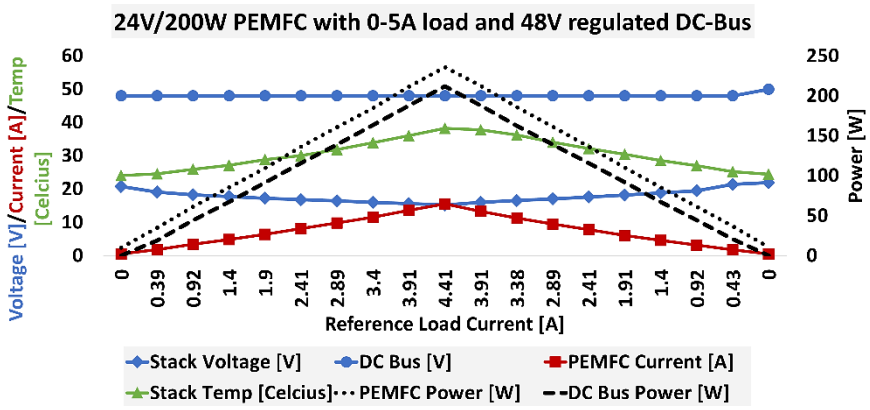

(a) Raw readings over recursive testing: over/under loading of 24V/200W PEMFC stack.

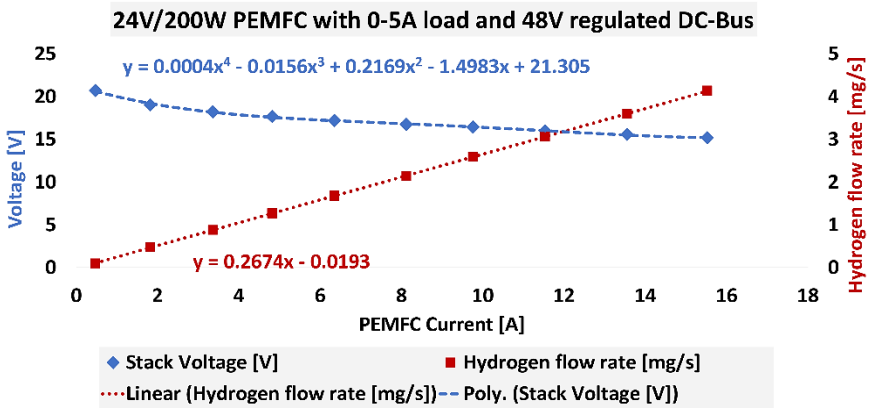

(b) Typical fitting models for 24V/200W PEMFC stack.

Figure 67: The characterization results for 200W open-cathode PEMFC stack.

5.2.3.2 Auxiliary devices powered through PEMFC stack

The second part of characterization is performed considering an operational condition very common in practice: the cooling fan being the major auxiliary device (power consumption wise) is powered via 24V/200W open-cathode PEMFC stack. For this purpose, a dedicated voltage-divider circuit is developed, which generates a 12V local source for the cooling-fan usage (presented in Figure 68). The voltage-divider based solution is power-inefficient but simple and cost-effective for the implementation purpose. In contrast, the residual devices including the control board and the fuel/purge regulation valves are still powered through external DC power supply (AL 963N). It is also worth recalling that the power consumption of the cooling fan is much higher compared to other auxiliary devices.

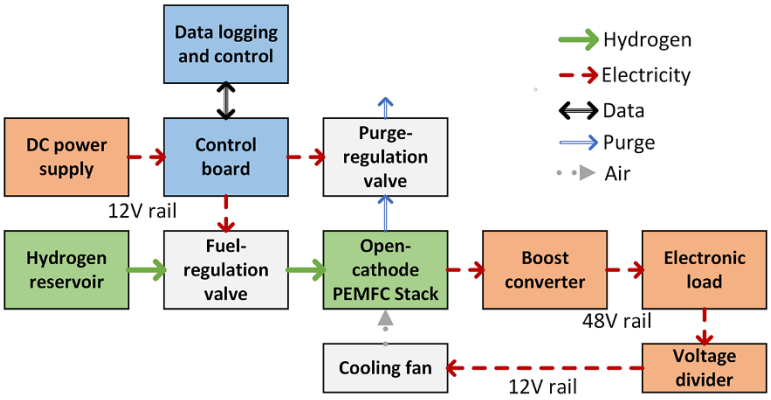

Figure 68: Abstract schematic of the test-bench with aux devices powered via PEMFC stack.

The readings obtained with this setup are presented in Figure 69a. The DC-bus is tightly regulated at the intended reference 48V, which exhibits the adequate performance of the Boost converter. The power losses at the PEMFC side are marginally increased due to the dependency of cooling-fan on the stack itself. The temperature of the stack gradually increases, even though the fan is supplied by the regulated local source. Still the temperature is well within the safe range of PEMFC stack.

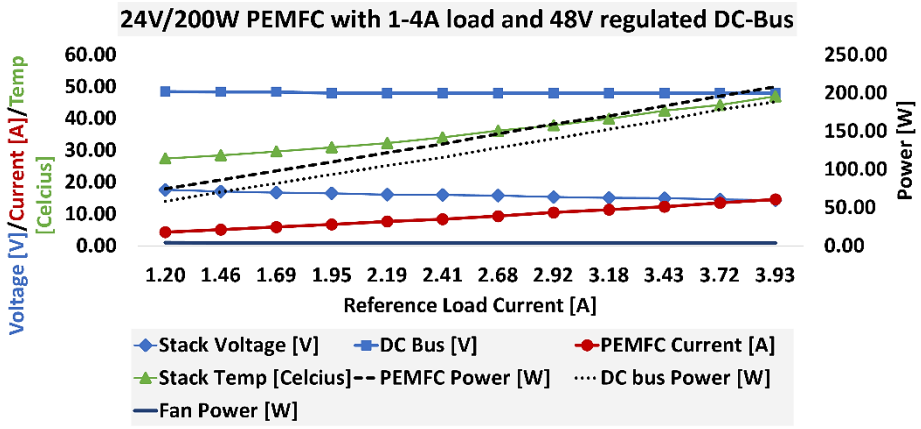

(a) Raw readings over recursive testing.

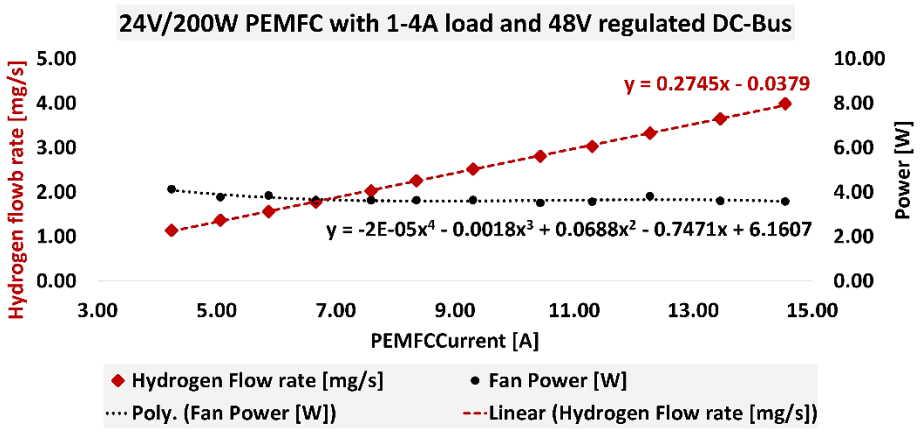

(b) Black-box fitting models for 24V/200W PEMFC stack.

Figure 69: The characterization results with auxiliary devices powered via PEMFC stack.

From Figure 69b, the polynomial fitting model for the hydrogen flowrate of 24V/200W PEMFC stack presented in (64) is modified, as the dependency of cooling-fan on the stack itself impacts its hydrogen consumption. The modified model to calculate the overall hydrogen consumption rate ($\dot{m}_{h_2}{}^{sys}$) is presented in (65). Likewise, the power consumption of the cooling-fan (P_{fan}) can be approximated as a higher order polynomial fitting function of the stack's current (A_{fc}), as depicted in (65). These models can be easily integrated in the OEMS, particularly facilitating an optimization framework.

$$\dot{m}_{h_2}{}^{sys} = -0.0379 + 0.2745 * A_{fc}$$
$$P_{fan} = 6.16 - 0.747 * A_{fc} + 0.069 * A_{fc}{}^{2} - 0.0018 * A_{fc}{}^{3} - 0.00002 * A_{fc}{}^{4} \quad (65)$$

As a distinct design step, the developed test-bench can be easily scaled to characterize a wide range of open-cathode PEMFC stacks with different power profiles. However, other components of the bench such as Boost converter and electronic load should be scaled accordingly.

5.2.4 Experimental setup for the validation of proposed OEMS

Given the availability of hardware resources, a small-scale hybrid power system for vehicular applications is developed to validate the control aspect. The objective is to verify the real-time applicability of proposed FSM as the dedicated OEMS of hybrid power system (and not the equivalency to powertrain topologies studied in the simulations). Given the available resources, a semi-active topology is designed: fuel cell is connected to the load via DC-DC boost converter, while battery is connected directly. The topology can be termed as a range-extender electric vehicle, and to match the observations/results of [137], an aggressive load-following mode is investigated at the control side. The developed system is extensively studied for a variety of driving conditions: a custom stepwise driving cycle and a standard urban/suburban US06 driving cycle.

5.2.4.1 Description and specifications of the test-bench

The complete test-bench along with the detailed connections diagram is presented in Figure 70. The bench is composed of two interconnected stages: the power stage and the control stage. Within the power stage, to emulate the behavior of fuel cell stack, a programmable power supply (EA-PSI 9080-120) is utilized. The emulated data points correspond to an actual open-cathode fuel cell (24 cells, 1200W). On the load side, an electronic load (EA-EL 9080-170 BHP) is employed to emulate the imposed driving cycle. A standard boost-converter (ZAHN Electronics DC6350F-SU) is utilized to interface the fuel cell emulator with the electronic load. To store the surplus energy and to support the fuel cell emulator during intermittent loading, a LiFePO4 battery pack (Winston LFP040) is integrated. Subsequently, the specifications of bench components are presented Table 25.

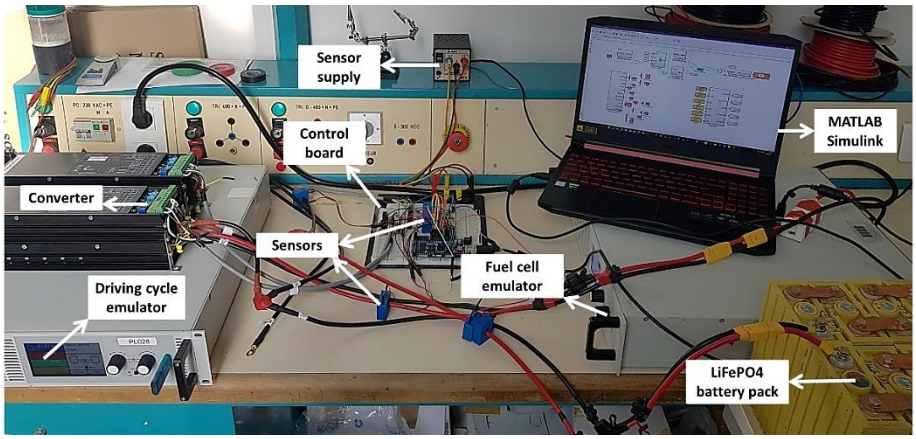

(a) Complete test-bench.

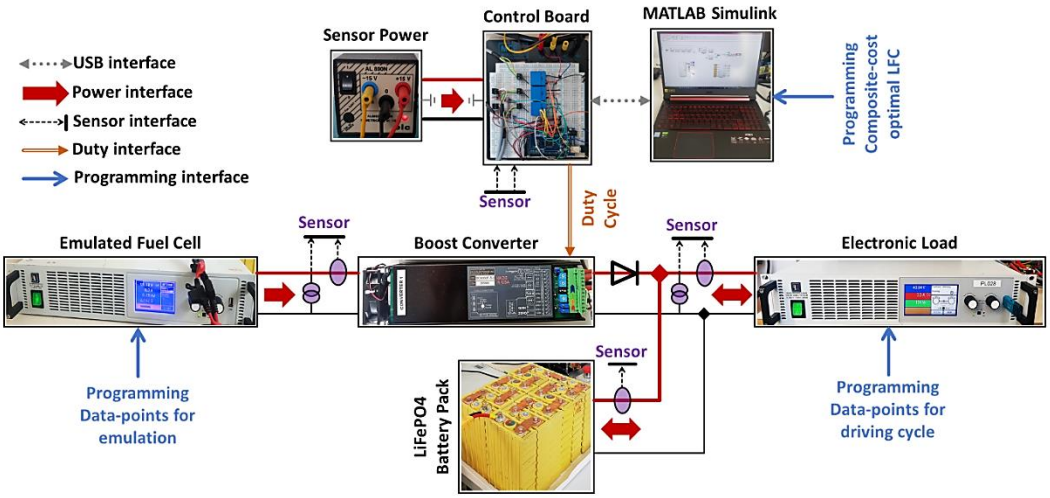

(b) Detailed inter-connections diagram.

Figure 70: Small-scale experimental bench devoted for vehicular applications.

At the control side, the Arduino 2560 kit is used to develop a bidirectional interface between the power stage and the decision-making device (MATLAB/Simulink installed on Acer Nitro-5 and

parameters presented in Appendix H: Table 33). The MATLAB/Simulink platform is exploited to implement the proposed OEMS. The Arduino kit serves the purpose of bidirectional signals flow: first feeding the sensors data to decision-making device; and later interpreting/converting the control signal (α_i= [0-1], $\alpha_i \in \mathbb{R}$) to an equivalent analogue signal (p_i= [0-5], $p_i \in \mathbb{R}$) using the DAC/SPI processing chip. This analogue signal is then imposed on the boost-converter to facilitate power-flow in agreement with the proposed OEMS.

Table 25: Exhaustive specifications of the test-bench components.

Stage	Component	Manufacturer (Model/Type)	Specifications
Power stage	Boost converter	ZAHN (DC6350F-SU)	0-50A, 12-63V
	Electronic PSU	EA-PSI (9080-120)	0-80V, 0-120A
	Electronic load	EA-EL (9080-170 BHP)	0-80V, 0-170A, 2400W
	Battery pack	Winston LFP040 (LiFePO4)	3.7V per cell, 40Ah 12 cells in series
Control stage	Control board	Arduino (Mega 2560)	-
	Current sensor	LEM (LA 55P)	0-50A
	Voltage sensor	LEM (LV 25P)	10-500V
	Decision-maker	Acer Nitro-5	-
	Power supply	ELC (AL 890N)	±15V with ground

5.2.4.2 Sensitivity analysis for parameters tuning

The sensitivity analysis is the first and foremost step to analyze the stability of the developed hybrid power system for a specific range of frequency-driven power separation rules (PSR). The initial value after rigorous test and trial (deemed as conventional/static PSR and denoted by Ψ_{fc} is selected as 0.5 Hz). The initial value dictates the nature of load-following (loose/aggressive [137]) only, and therefore can be chosen independently of the powertrain composition and nature of load. Subsequently, the upper and lower bounds (denoted by ${\Psi_{fc}}^{\pm}$) are set to 0.67/0.4 Hz. These limits are assumed and adjusted considering the aspects of stability and optimization. It is observed during the experiments phase that increasing the value of PSR bounds (that is increasing the search range) improves the optimization results, though overall stability of the system is negatively impacted. Another important parameter worth discussing is the dimension of the search-horizon φ, having the information of candidate power separation rules ($\Psi_{m=1,2,..M}$). A key role is played by the dimension parameter (M) in terms of establishing a compromise between computational complexity (obstructing online implementation) and quality of optimization. The upper limit of parameter M is set to 05, which is sufficient considering the practical limitations associated to Arduino based bidirectional interface.

After setting all the parameters, a suitable driving cycle is imposed for sensitivity analysis. To serve this purpose, a stepwise increasing/decreasing load profile is imposed using the driving cycle emulator. The impact of conventional/static PSR and its upper/lower bounds on the fuel

cell profile is exhibited in Figure 71a. It can be witnessed that the fuel cell emulator follows imposed load as dictated by the frequency-driven PSR (mentioned as LFR in the Figures). Consequently, the operation of hybrid system in maintaining the power balance is impacted by the associated PSR. Thereafter, the critical operational parameters of the hybrid power system: the global power balance, the expected hydrogen consumption, the LiFePO4 battery-pack profile (voltage and SoC), and the expected SoH profile of power sources are respectively presented in Figure 71b, Figure 71c, Figure 71d, and Figure 71e.

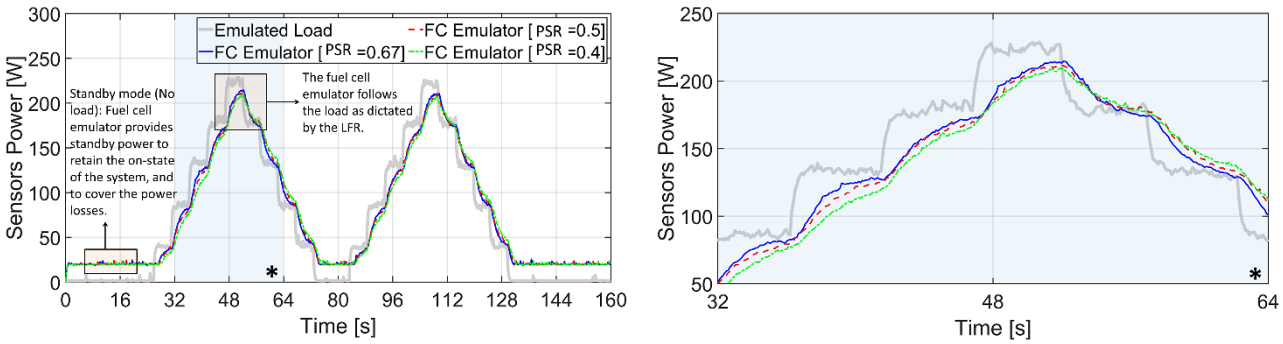

(a) Impact of conventional and bounded limits of PSR on the power profile of fuel cell emulator.

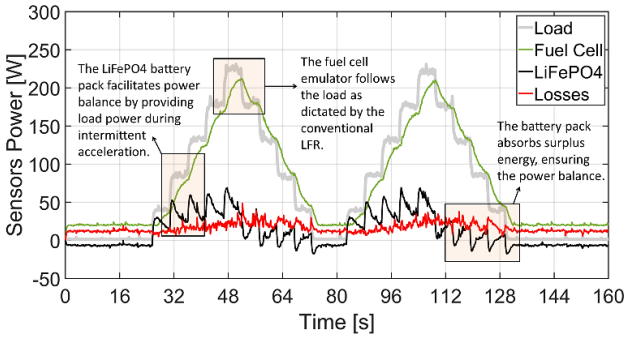

(c) Power balance with the conventional PSR.

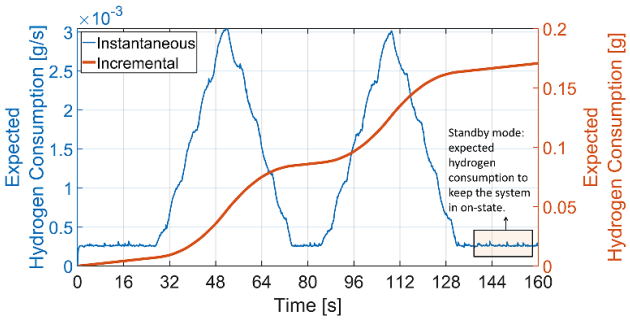

(d) Expected hydrogen consumption.

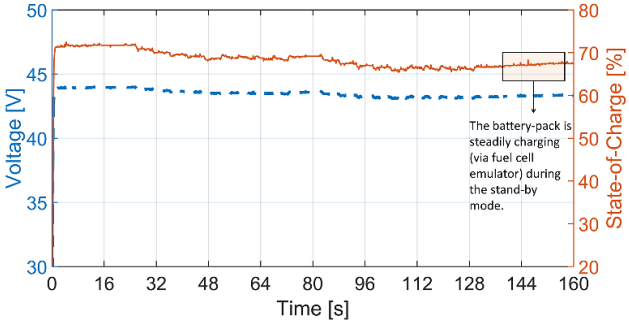

(e) LiFePO4 profile with the conventional PSR.

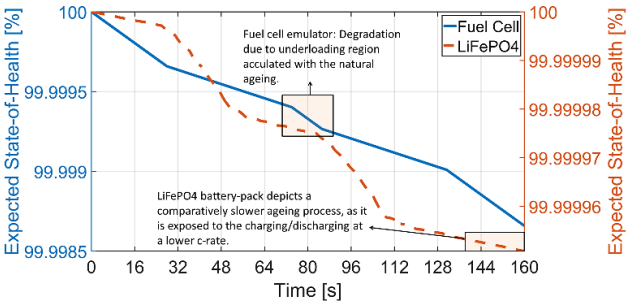

(f) Expected SoH profile with conventional PSR.

Figure 71: Sensitivity analysis under the action of custom stepwise load profile.

The extensive sensitivity analysis yields satisfactory statistical results (presented in Table 26) for the assumed conventional/static PSR and its bounded range. The obtained results also manifest

the possibility of an online optimizer to tune the instantaneous value of PSR (restrained by the bounded values), as a particular value of PSR impacts the system operation in a distinct manner.

5.2.4.3 Application under benchmark driving cycle

For assessment purpose, the comparatively harsh urban/suburban US06 driving cycle is extensively studied, which matches with the aim of this dissertation and fits with the limitations of available programmable load. The speed profile of US06 is presented in Appendix F: Figure 73, which is adopted from a well-known report [137]. To accommodate the limitations of the driving cycle emulator, the timespan of normal US06 cycle is modified and the cycle is repeated for two consecutive iterations. Moreover, the electronic load can only absorb power, which limits the emulated data points to the positive values (the regenerative power is not considered due to this limitation). As a note, beside US06 which is selected here because of its overall merits, any other standard driving cycle can be equally studied, if scaled (data-wise and points-wise) properly.

Table 26: Statistical results for the sensitivity analysis performed under stepwise cycle.

Power separation rule PSR [Hz]	Expected hydrogen consumption [g]	Expected State-of-Health [%]				State-of-Charge [%]	
		Fuel cell emulator		LiFePO4 battery		SoC_i	SoC_f
		SoH_i	$SoH_f \cong$	SoH_i	$SoH_f \cong$		
Static [Ψ=0.5]	0.1707	100	99.9987	100	99.99996	72.46	67.44
Upper-bound [Ψ^+=0.67]	0.1709	100	99.9987	100	99.99996	72.58	67.57
Lower-bound [Ψ^-=0.4]	0.1695	100	99.9986	100	99.99994	72.79	67.44

In that context, the power balance is exhibited in Figure 72a, reflecting efficacy of the proposed method in terms of distributing the traction power among hybrid power sources. Essentially, the fuel cell emulator follows traction load as dictated by the online-tuned PSR (Ψ_{fc}^{opt}), while the LiFePO4 battery-pack supports fuel cell in order to achieve global power balance. The expected instantaneous/incremental hydrogen consumption corresponding to fuel cell profile is presented in Figure 72b. The LiFePO4 battery profile is depicted in Figure 72c: the starting SoC of battery-pack exceeds its allocated soft limited (SoC_b > 75%), thereby manifesting the SoC violation cost in the same region (apparent from Figure 72e). Finally, the expected SoH profiles of the power sources are commutatively presented in Figure 72d.

Three PSRs with the distinct nature are compared: the online-tuned best PSR (Ψ_{fc}^{opt}), the worst PSR, and the conventional method with static PSR. The adaptive nature of these LFRs is exhibited in Figure 72g, given the instantaneous minimization/maximization of the rationalized cost. Subsequently, the rationalized costs associated with the distinct PSRs are presented in Figure 72f, highlighting that the chosen PSR bears least cost (suggesting the effectiveness of online optimizer). Finally, the constituent (operational) rationalized-costs corresponding to the chosen online-tuned PSR (Ψ_{fc}^{opt}) are presented in Figure 72e.

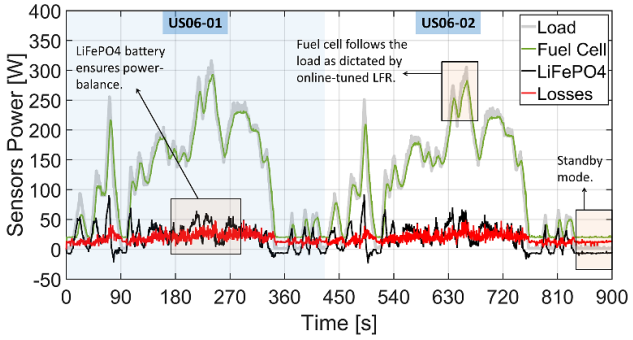

(a) Power balance with online-tuned PSR.

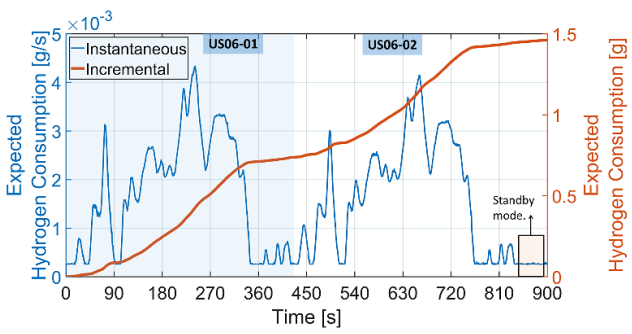

(b) Expected hydrogen consumption with online-tuned PSR.

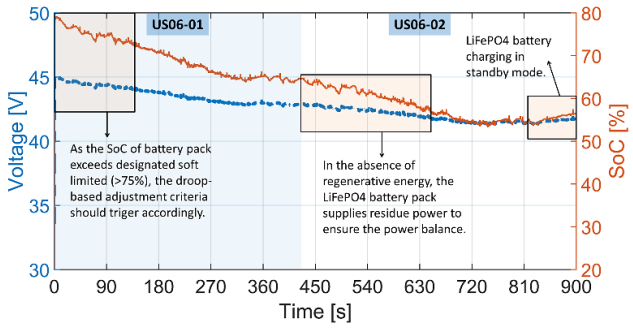

(c) LiFePO4 profile with online-tuned PSR.

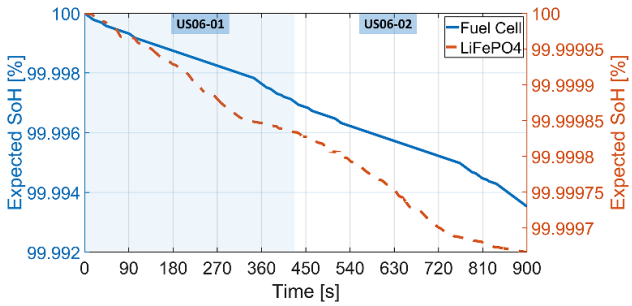

(d) Expected SoH profile with online-tuned PSR.

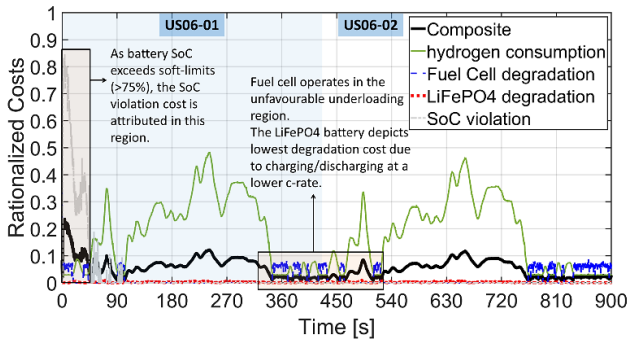

(e) Rationalized costs with online-tuned PSR.

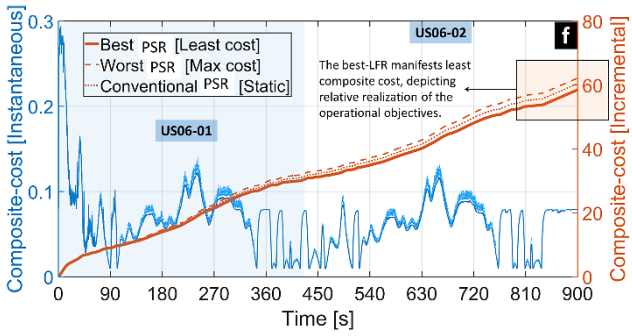

(f) Rationalized costs with comparative PSRs.

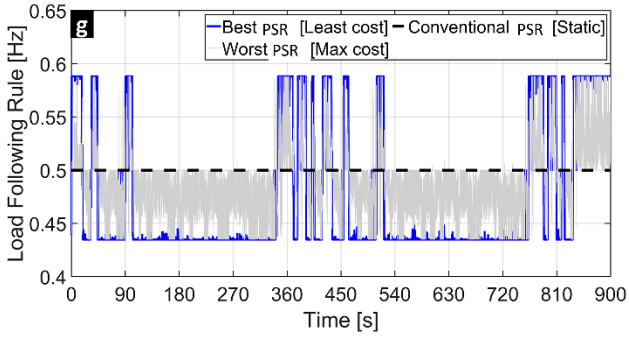

(g) Instantaneous adaptation of PSR.

Figure 72: Operational parameters of the studied system in the consecutive US06 cycles.

The results respectively presented in Figure 72 validates the applicability and efficacy of the proposed FSM method (in relation to the control aspect), especially for the real-time hybrid systems devoted for vehicular applications. It is also expected that the proposed method will perform in the same effective manner the similar (commercial and upscaled) hybrid systems, as it did with the small-scale hybrid system. The rigorous assessment under a comparatively harsh US06 driving cycle reflects promising prospects for the similar and other mixed driving environments.

Conclusion and perspectives

This thesis is devoted to the key design and control aspects of hybrid electric vehicles (HEVs) by improving both aspects at an individual level and coordinating them in a novel way. Within the HEV domain, the fuel cell hybrid electric vehicle (FCHEV) is selected as the core research area, and special attention is paid to urban driving environments due to their unique and rough nature compared to others, such as intermittent acceleration/braking and frequent start-stops.

The proposed FCHEV design process adheres to the following protocol: (i) the justified selection and adequate modeling of the HEV-dependent power/energy sources; (ii) the arrangement of selected sources into a viable topological structure and proposing an effective power processing stage; (iii) finally, the sizing of propulsion elements based on the desired road response and the selected vehicle dimensions.

The developed sizing algorithm is strictly analytical and generic in scope. It is computationally efficient, can be easily implemented at the system design level, and can be theoretically applied to a variety of HEVs. According to the proposed algorithm, the FCHEV propulsion system is systematically configured according to the cruising speed and the vehicle parameters. However, the baseline configuration generally favors oversized sources, which on the contrary may increase the ownership price. To address this problem, flexible but practical sizing of the propulsion sources is considered by introducing the concept of flexible design coefficients (FDC). Subsequently, the sizing algorithm is coordinated with the energy management system (EMS) to choose a suitable configuration from this sizing range with the best compromise. The application of the proposed sizing algorithm on two different hypothetical vehicles with equal effectiveness demonstrates its suitability.

From the vehicles studied and analyzed in detail, it emerges that the small-size hypothetical vehicle can either serve as light-duty logistics transportation or as an intercity passenger vehicle. Meanwhile, the mid-size vehicle is a dedicated passenger transport equivalent to a mid-size sedan or hatchback car.

On the control side, an online EMS with a new optimization framework is offered to ensure an informed trade-off among key operational objectives (hydrogen consumption and source degradation). Essentially, a rules-driven frequency separation method (FSM) is employed because of easier online implementation and less aggressive rules-transition. However, the conventional FSM uses a static power separation rule (PSR), which generally provides a suboptimal experience. Therefore, a frequency-horizon based online optimizer is designed in which the PSR is tuned in an instantaneous manner to reduce the total rationalized cost (weighted sum of hydrogen consumption cost, source degradation cost, and SoC violation cost). To achieve charge sustainability and reduce the violation of SoC limits, a droop-based method is integrated to adjust the reference signals in real-time.

To investigate the effectiveness and feasibility of the proposed methods (both design and control aspects), a validation criterion is developed around several driving cycles based on standard and real driving data. For the hypothetical light-duty vehicle, the optimal powertrain configuration exists at the upper spectrum of FDC (which promotes PEMFC stack of the same size as the base configuration: the largest possible rated capacity, equal to 6 k*W*) for the classic urban Artemis cycle with intermittent acceleration/deceleration and prolonged start-stops. While, for a less harsh suburban WLTP-class 1 cycle, the optimal config of PEMFC stack is at the lower side of spectrum (lowest possible 4.5 k*W*). Since both driving environments are inherently opposite, the preferred choice can be anything in the range of 4.5-6k*W*, as a viable global solution for the PEMFC stack. With the optimally selected configuration, the proposed online-EMS respectively yields 4.33% and 1.58% improvements in minimizing the overall rationalized cost (ORC) for the studied driving cycles (compared to the conventional FSM with static PSR[161, 162] and the offline-tuned FSM[54]). The observed %improvements indicate the possibility to reach actual fuel savings and prolong the sources lifespan in real-time scenarios, by the usage of proposed methods.

For the hypothetical mid-size vehicle, the optimal configuration is present at the lower side of (FDC) spectrum for the examined LA92 driving cycle. The LA92 cycle is preferred because it is comprehensive enough to study the nature and performance of mid-size vehicle (a combination of urban and suburban environments with a cruising speed matched with a highway). Accordingly, a PEMFC stack of 27 k*W* (nominal capacity) is chosen alongside 6.51 k*Wh* battery-pack, and 27 *F* supercap bank. Also, on the control side, the proposed online-tuned FSM delivers 7.33% and 6.67% improvements over the conventional FSM and offline-tuned FSM in terms of minimizing ORC. Inclusively, the obtained results demonstrate effectiveness of the proposed techniques (the design, control, and coordination aspect) in finding an appropriate trade-off between the expected price and the key operational objectives for a variety of vehicles (light-duty vehicle and mid-size passenger vehicle).

As a third and final test, a hybrid powertrain system of the studied FCHEV is studied with parameters and specifications similar to those of a commercial vehicle (Toyota-Mirai[137]). The performance of the commercial vehicle is examined for Artemis highway-cycle. Various aspects such as power balance, sources operational parameters and stability metrics are investigated to demonstrate the suitability of the proposed online-tuned FSM. The test is extended to examine performance of the studied vehicles in the driving cycle with real driving data (ETC FIGE-4[172]). The purpose is to examine the suitability and expectations of the proposed methods in the real driving environments.

Several small-scale experimental studies are conducted by our research group to validate the real-time applicability of the proposed methods, which is in context to design and control aspects. From the design side, (*i*) an experimentally validated power stage consisting of boost converters connected in parallel is developed for PEMFC based high power applications. The developed power stage is particularly suitable for vehicle applications, and its performance is validated first with programmable components (emulation), and later with the actual

components. (*ii*) A test bench is developed to characterize the open-cathode PEMFC stack, and tests are conducted for a 24 *V* stack with a nominal power of 200 *W*. The purpose is to study the performance of this particular PEMFC stack (under various operating conditions), and to develop the polynomial fitting models for the effective integration in the OEMS. Nevertheless, the test bench can be used to characterize a variety of PEMFC stacks with similar specifications. (*iii*) a series of tests are conducted to characterize a 48 *V* li-ion battery pack with 25 A*h* nominal capacity. The same battery pack is then rigorously tested under the designated driving cycle (developed from field tests conducted on electrified tuk-tuk vehicles) to estimate overall feasibility and cycle expectancy (electrical mileage) for the given battery pack. Alternatively, the same test can be conducted to size battery-pack in order to reach the target mileage. The developed bench is scalable in terms of characterizing other battery packs with similar power profiles, and to approximate the electrical mileage under the action of any real-time/hypothetical driving cycle. Finally, from the control side, a small-scale experimental bench is developed to examine the efficacy and real-time applicability of the proposed OEMS. For validation, two driving environments are extensively studied: a custom stepwise increasing/decreasing driving cycle and a standard US06 cycle with urban/suburban profile. The obtained results illustrate that the proposed methods are expected to function in a consistent manner for similar (commercial and upscaled) hybrid systems, as well for the driving environments with mixed profile/nature.

Limitations and future directions

- The proposed sizing algorithm (based on design-coefficients) is computationally efficient and generic in nature: in this dissertation, the applicability is only depicted for two hypothetical FCHEVs (light-duty and mid-size passenger vehicles). In the future studies, the application of this algorithm will be expanded to other HEVs (with different specifications and parameters), as well as other modes of transportation.
- Beside the studied vehicles (light-duty, mid-size passenger, and commercial), the inclusion of a heavy-duty logistic vehicle is planned to test the developed methods (the control and design aspects).
- Among the principal limitations is related to proposed online optimizer based on frequency-horizon (within online-tuned FSM). Being an online optimizer, the optimization performance and computational complexity are jointly linked to the dimensions of chosen horizon. This particular aspect is not investigated in detail, and given its importance, it is intended to be investigated in the future studies.
- The comparative study at the control-side (online-EMS based on FSM) was limited to two similar techniques: conventional FSM and offline-tuned FSM. The comparative study is projected to be extended for other similar (rules-based) and even entirely different techniques.
- The experimental studies are conducted with a small-scale perspective, in order to validate the real-time applicability of the proposed design and control methods. Consequently, it is expected that the proposed techniques will be validated in the future by building a suitable full-scale test bench.

Appendix A: Traction data for the studied vehicles

Table 27: The values of traction parameters corresponding to the studied vehicle.

Vehicle chassis		Coefficients				% Efficiency	
Area	Mass	Air density	Drag	Rolling	Gravity	Inverter	Motor
$S\ [m^2]$	$M_v\ [kg]$	$\rho_a\ [kg/m^3]$	$\mathbb{\Gamma}_d$	$\mathbb{\Gamma}_r$	$g\ [m/s^2]$	η_i	η_m
Hypothetical: light-duty (small-size) vehicle.							
2	980	1.202	0.32	.008	9.81	90	85
Hypothetical: mid-size passenger vehicle.							
2.1	1900	1.202	0.29	.004	9.81	90	90
Commercial-grade vehicle [137].							
2.1	1950	1.202	0.29	.0015	9.81	90	90

Appendix B: Polynomial fitting coefficients for the fuel cell system

Table 28: Details of fitting coefficients associated with the studied vehicles.

α_0	α_1	α_2
Hypothetical: light-duty vehicle.		
1050	1.15	1.369e-04
Hypothetical: mid-size vehicle.		
1050	1.5	1.969e-05
γ_1	γ_2	γ_3
Commercial-grade vehicle [137].		
0.0271	0.00378	1.556e-07

Appendix C: Degradation coefficients for the fuel cell stack

Table 29: Details of degradation coefficients associated with the studied vehicles.

β_1	β_2	β_3	β_4	β_5	β_6
Hypothetical: light-duty vehicle.					
0.002	1e-8	4e-6	2e-4	0.075+Δt*0.2e-4	4e-5
Hypothetical: mid-size vehicle.					
0.004	1e-7	4e-6	2e-4	0.075+Δt*0.2e-4	4e-5
Commercial-grade vehicle [137].					
0.005	0.00126	0.00147	0.00196	0.0000593	-

Appendix D: Design coefficients for the sizing procedure

Table 30: Description of design coefficients assumed in this dissertation.

Nature		Static					Flexible	
Coefficient		Δ_m	Δ_k	Δ_{dc}	Δ_{sc}	Δ_b	Δ_{fc}	Δ_{doh}
Influence	Motor	✓	✓	×	×	×	×	×
	PEMFC	×	×	✓	×	×	✓	×
	Supercap Bank	×	×	×	✓	×	×	✓
	Battery Pack	×	×	×	×	✓	×	✓
Value	Upper bound	0.2	1.0	0.65	0.65	0.5	1.0	0.75
	Lower bound						0.75	0.5

The values of design coefficients are assumed from the literature and from personal (and logical) interpretation. For example, facilitating a logical and realizable configuration of battery pack (cells in series/parallel, etc.).

Appendix E: System configuration for the commercial-scale vehicle

Table 31: Specifications of the propulsion elements employed in Toyota Mirai [137].

Component	No of cells/units		Capacity	Voltage $[V]$
	Series	Parallel		
PEMFC	$\mathcal{N}_{fc}$ =370	×	${P_{fc}}^{nom}$ =114 kW	${V_{cell}}^{fc}$*$\mathcal{N}_{fc}$
Battery pack	36 cells in total		${E_b}^{pack}$ ≅1.6 kWh	${V_b}^{nom}$ =325.6
Motor/DC Link	×	×	P_m^{max} =113 kW	${V_o}^{ref}$ =650

Appendix F: Speed profile of US06 driving cycle

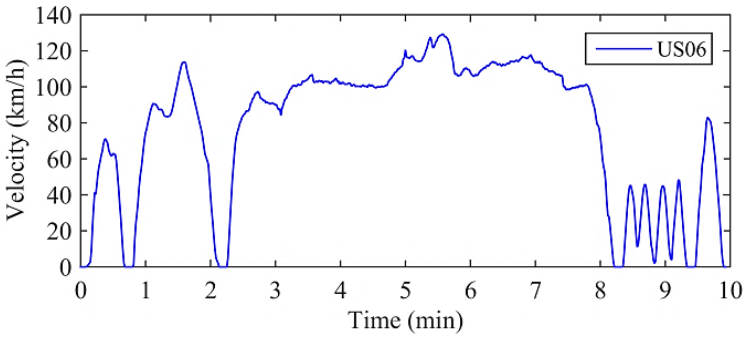

Figure 73: The speed profile of US06 driving cycle [173].

Appendix G: Parameters setting for simulations environment

Table 32: The MATLAB/Simulink based simulations environment.

Search-horizon	**Controller gains (current)**
Members $[M]$ = 10 – 15	Hypothetical → K_p = 1e-3, K_i = 1e-3
Bounds for FC $\Psi_{fc}^{\pm}$ $[Hz]$ 0.035 – 0.045 (hypothetical) 0.196 – 0.204 (commercial)*	Commerical-scale → K_p = 4e-3, K_i = 1e-3
Battery (fixed) → Ψ_b $[Hz]$ = 0.5	
Solver (MATLAB)	**Converter (hypothetical)****
Fixed-step (discrete) = Euler (ode1)	Input-side inductor $[H]$ = 1e-3
Ts (sample time) = 2e-4 (hypothetical)	DC-link capacitor $[F]$ = 2200e-6
Ts = 5e-5 (commercial-scale)	
System param	**Converter (commercial-scale)****
SoC limiters $SoC_{HSL}^{\pm}$ $[\%]$ = [95 – 85, 35 – 25]	Input-side inductor $[H]$ = 0.1e-3
EoL $[h]$ = 5000	DC-link capacitor $[F]$ = 1100e-6
SoH_i $[\%]$ = 100	
Controller gain (Voltage)	
K_p = 0.1, K_i = 450	

*Aggressive load-following to match [137], and with the fact that supercap is absent.

**Adopted from [174].

Appendix H: Parameters setting for experimental work

Table 33: The MATLAB/Simulink based experimental environment.

Search-horizon	**Controller gains (current)**
Members [M] = 04 – 06	K_p = 0.25
Bounds → $\Psi_{fc}{}^{\pm}$ [*Hz*] = 0.4 – 0.67	K_i = 0.015*3.5
Solver (MATLAB)	**System param**
Fixed-step (discrete) = Euler (ode1)	SoC limiters [*%*] = [80 – 75 and 25 – 20]
Ts (sample time) = 0.1	EoL [*h*] = 5000
	SoH_i [*%*] = 100

References

[1] OurWorldData. "Global emissions from Transport (An online report)." https://ourworldindata.org/co2 emissions-from-transport.

[2] StatistaResearchDepartment. "Distribution of green house gas emissions in Metripolitan France (An online report)." https://www.statista.com/statistics/1025515/greenhouse-gas-emissions-distribution-france/.

[3] A. Jillian, "UK plans to bring forward ban on fossil fuel vehicles to 2030," in *The Guardian*, ed, 2020.

[4] OfficialEUWebsite. "2050 long-term EU strategy regarding GHG emsissions." https://ec.europa.eu/clima/policies/strategies/2050_en.

[5] M. Mansoor Ashraf, T. Nadeem Malik, and M. Iqbal, "Peak load sharing based on blade pitch control of wind turbine in the presence of utility supply," *Journal of Renewable and Sustainable Energy,* vol. 6, no. 1, p. 013110, 2014.

[6] M. Ashraf, T. Malik, and M. Iqbal, "Development of a prototype micro wind energy system with adjustable blade pitch for experimentation purposes at laboratory level," *The Nucleus,* vol. 51, no. 1, pp. 75-86, 2014.

[7] S. Comello, G. Glenk, and S. Reichelstein, "Transitioning to clean energy transportation services: Life-cycle cost analysis for vehicle fleets," *Applied Energy,* vol. 285, p. 116408, 2021/03/01/ 2021, doi: https://doi.org/10.1016/j.apenergy.2020.116408.

[8] X. Zhao, Y. Ke, J. Zuo, W. Xiong, and P. Wu, "Evaluation of sustainable transport research in 2000–2019," *Journal of Cleaner Production,* vol. 256, p. 120404, 2020/05/20/ 2020, doi: https://doi.org/10.1016/j.jclepro.2020.120404.

[9] F. Orecchini and A. Santiangeli, "CHAPTER TWENTY TWO - Automakers' Powertrain Options for Hybrid and Electric Vehicles," in *Electric and Hybrid Vehicles*, G. Pistoia Ed. Amsterdam: Elsevier, 2010, pp. 579-636.

[10] Z. Liu *et al.*, "Comparing total cost of ownership of battery electric vehicles and internal combustion engine vehicles," *Energy Policy,* vol. 158, p. 112564, 2021/11/01/ 2021, doi: https://doi.org/10.1016/j.enpol.2021.112564.

[11] B. Lane, "Plug-in Fuel Cell Electric Vehicles: A Vehicle and Infrastructure Analysis and Comparison with Alternative Vehicle Types," UC Irvine, ProQuest ID: Lane_uci_0030M_14813, 2017. [Online]. Available: Retrieved from https://escholarship.org/uc/item/57h0j2sv

[12] Ö. Balcı *et al.*, "Numerical and experimental investigation of fuel consumption and CO2 emission performance for a parallel hybrid vehicle," *Alexandria Engineering Journal,* vol. 60, no. 4, pp. 3649-3667, 2021/08/01/ 2021, doi: https://doi.org/10.1016/j.aej.2021.02.025.

[13] Y. Zhang, C. Wei, Y. Liu, Z. Chen, Z. Hou, and N. Xu, "A novel optimal power management strategy for plug-in hybrid electric vehicle with improved adaptability to traffic conditions," *Journal of Power Sources,* vol. 489, p. 229512, 2021/03/31/ 2021, doi: https://doi.org/10.1016/j.jpowsour.2021.229512.

[14] L. Bretscher and E. Grieg, "Exiting the fossil world: The effects of fuel taxation in the UK," *Economics Working Paper Series,* vol. 20, 2020.

[15] D. Chabane *et al.*, "Coupling a metal hydride tank with a PEMFC for vehicular applications: A simulations framework," *International Journal of Energy Research,* vol. 45, no. 11, pp. 16511-16523, 2021, doi: https://doi.org/10.1002/er.6898.

[16] A. A. Kamel, H. Rezk, and M. A. Abdelkareem, "Enhancing the operation of fuel cell-photovoltaic-battery-supercapacitor renewable system through a hybrid energy management strategy," *International Journal of Hydrogen Energy,* 2020.

[17] W.-M. Chen and H. Kim, "Energy, economic, and social impacts of a clean energy economic policy: Fuel cells deployment in Delaware," *Energy Policy,* vol. 144, p. 111617, 2020.

[18] C. Zhang *et al.*, "Flexible grid-based electrolysis hydrogen production for fuel cell vehicles reduces costs and greenhouse gas emissions," *Applied Energy,* vol. 278, p. 115651, 2020.

[19] P. Ahmadi, S. H. Torabi, H. Afsaneh, Y. Sadegheih, H. Ganjehsarabi, and M. Ashjaee, "The effects of driving patterns and PEM fuel cell degradation on the lifecycle assessment of hydrogen fuel cell vehicles," *International Journal of Hydrogen Energy,* vol. 45, no. 5, pp. 3595-3608, 2020.

[20] M. Iqbal, H. S. Ramadan, and M. Becherif, "Health-aware frequency separation method for online energy management of fuel cell hybrid vehicle considering efficient urban utilization," *International Journal of Hydrogen Energy,* vol. 46, no. 29, pp. 16030-16047, 2021/04/26/ 2021, doi: https://doi.org/10.1016/j.ijhydene.2021.02.072.

[21] M. Iqbal, M. Becherif, H. S. Ramadan, and A. Badji, "Dual-layer approach for systematic sizing and online energy management of fuel cell hybrid vehicles," *Applied Energy,* vol. 300, p. 117345, 2021/10/15/ 2021, doi: https://doi.org/10.1016/j.apenergy.2021.117345.

[22] M. Iqbal, A. Benmouna, F. Eltoumi, F. Claude, M. Becherif, and H. S. Ramadan, "Cooperative Operation of Parallel Connected Boost Converters for Low Voltage-High Power Applications: An Experimental Approach," *Energy Procedia,* vol. 162, pp. 349-358, 2019/04/01/ 2019, doi: https://doi.org/10.1016/j.egypro.2019.04.036.

[23] M. Iqbal, J. Laurent, A. Benmouna, M. Becherif, H. S. Ramadan, and F. Claude, "Ageing-aware load following control for composite-cost optimal energy management of fuel cell hybrid electric vehicle," *Energy,* vol. 254, p. 124233, 2022/09/01/ 2022, doi: https://doi.org/10.1016/j.energy.2022.124233.

[24] F. Orecchini, A. Santiangeli, and F. Zuccari, "Hybrid-electric system truth test: Energy analysis of Toyota Prius IV in real urban drive conditions," *Sustainable Energy Technologies and Assessments,* vol. 37, p. 100573, 2020/02/01/ 2020, doi: https://doi.org/10.1016/j.seta.2019.100573.

[25] K. Yoshimoto and T. Hanyu, "NISSAN e-POWER: 100 % Electric Drive and Its Powertrain Control," *IEEJ Journal of Industry Applications,* vol. advpub, 2021, doi: 10.1541/ieejjia.20013024.

[26] M. Bonci, "Fuel Cell Vehicle simulation: an approach based on Toyota Mirai," Politecnico di Torino, 2021.

[27] E. Pahon, D. Hissel, S. Jemei, and N. Y. Steiner, "Signal-based diagnostic approach to enhance fuel cell durability," *Journal of Power Sources,* vol. 506, p. 230223, 2021/09/15/ 2021, doi: https://doi.org/10.1016/j.jpowsour.2021.230223.

[28] S. Ahmadi, S. M. T. Bathaee, and A. H. Hosseinpour, "Improving fuel economy and performance of a fuel-cell hybrid electric vehicle (fuel-cell, battery, and ultra-capacitor) using optimized energy management strategy," *Energy Conversion and Management,* vol. 160, pp. 74-84, 2018/03/15/ 2018, doi: https://doi.org/10.1016/j.enconman.2018.01.020.

[29] Y. Feng and Z. Dong, "Optimal energy management strategy of fuel-cell battery hybrid electric mining truck to achieve minimum lifecycle operation costs," *International Journal of Energy Research,* vol. 44, no. 13, pp. 10797-10808, 2020, doi: https://doi.org/10.1002/er.5728.

[30] F. Peng *et al.*, "Development of master-slave energy management strategy based on fuzzy logic hysteresis state machine and differential power processing compensation for a PEMFC-LIB-SC hybrid tramway," *Applied Energy,* vol. 206, pp. 346-363, 2017/11/15/ 2017, doi: https://doi.org/10.1016/j.apenergy.2017.08.128.

[31] Y. Wang, Z. Sun, and Z. Chen, "Development of energy management system based on a rule-based power distribution strategy for hybrid power sources," *Energy,* vol. 175, pp. 1055-1066, 2019/05/15/ 2019, doi: https://doi.org/10.1016/j.energy.2019.03.155.

[32] K. Kaya and Y. Hames, "Two new control strategies: For hydrogen fuel saving and extend the life cycle in the hydrogen fuel cell vehicles," *International Journal of Hydrogen Energy,* vol. 44, no. 34, pp. 18967-18980, 2019/07/12/ 2019, doi: https://doi.org/10.1016/j.ijhydene.2018.12.111.

[33] C. H. Zheng, C. E. Oh, Y. I. Park, and S. W. Cha, "Fuel economy evaluation of fuel cell hybrid vehicles based on equivalent fuel consumption," *International Journal of Hydrogen Energy,* vol. 37, no. 2, pp. 1790-1796, 2012/01/01/ 2012, doi: https://doi.org/10.1016/j.ijhydene.2011.09.147.

[34] D. Chabane, L. Serairi, M. Iqbal, A. Djerdir, N. Fenineche, and O. Elkedim, "Innovative method to estimate state of charge of the hydride hydrogen tank: application of fuel cell electric vehicles," *International Journal of Modelling and Simulation,* pp. 1-14, 2021.

[35] W. Enang and C. Bannister, "Modelling and control of hybrid electric vehicles (A comprehensive review)," *Renewable and Sustainable Energy Reviews,* vol. 74, pp. 1210-1239, 2017/07/01/ 2017, doi: https://doi.org/10.1016/j.rser.2017.01.075.

[36] Y. Wang, Z. Sun, and Z. Chen, "Energy management strategy for battery/supercapacitor/fuel cell hybrid source vehicles based on finite state machine," *Applied Energy,* vol. 254, p. 113707, 2019/11/15/ 2019, doi: https://doi.org/10.1016/j.apenergy.2019.113707.

[37] Q. Xun, Y. Liu, and N. Zhao, "Energy efficiency comparison of hybrid powertrain systems for fuel-cell-based electric vehicles," in *2020 IEEE Transportation Electrification Conference & Expo (ITEC)*, 2020: IEEE, pp. 1234-1239.

[38] X. Lü, P. Wang, L. Meng, and C. Chen, "Energy optimization of logistics transport vehicle driven by fuel cell hybrid power system," *Energy Conversion and Management,* vol. 199, p. 111887, 2019/11/01/ 2019, doi: https://doi.org/10.1016/j.enconman.2019.111887.

[39] D. Zhou, A. Al-Durra, I. Matraji, A. Ravey, and F. Gao, "Online Energy Management Strategy of Fuel Cell Hybrid Electric Vehicles: A Fractional-Order Extremum Seeking Method," *IEEE Transactions on Industrial Electronics,* vol. 65, no. 8, pp. 6787-6799, 2018, doi: 10.1109/TIE.2018.2803723.

[40] S. Farhani, A. N'Diaye, A. Djerdir, and F. Bacha, "Design and practical study of three phase interleaved boost converter for fuel cell electric vehicle," *Journal of Power Sources,* vol. 479, p. 228815, 2020.

[41] A. Subramanian and S. Kr, "Review of multiport isolated bidirectional converter interfacing renewable and energy storage system," *International Journal of Power Electronics and Drive Systems,* vol. 11, no. 1, p. 466, 2020.

[42] G. Zhang, N. Jin, L. Qu, and S. S. Yu, "Inherently non-pulsating input current DC-DC converter for battery storage systems," *IEEE Access,* vol. 8, pp. 140293-140302, 2020.

[43] I.-S. Sorlei *et al.*, "Fuel cell electric vehicles—a brief review of current topologies and energy management strategies," *Energies,* vol. 14, no. 1, p. 252, 2021.

[44] Y. Zhang, C. Zhang, Z. Huang, L. Xu, Z. Liu, and M. Liu, "Real-Time Energy Management Strategy for Fuel Cell Range Extender Vehicles Based on Nonlinear Control," *IEEE Transactions on Transportation Electrification,* vol. 5, no. 4, pp. 1294-1305, 2019, doi: 10.1109/TTE.2019.2958038.

[45] T. Wang *et al.*, "An optimized energy management strategy for fuel cell hybrid power system based on maximum efficiency range identification," *Journal of Power Sources,* vol. 445, p. 227333, 2020.

[46] H. S. Das, C. W. Tan, and A. H. M. Yatim, "Fuel cell hybrid electric vehicles: A review on power conditioning units and topologies," *Renewable and Sustainable Energy Reviews,* vol. 76, pp. 268-291, 2017/09/01/ 2017, doi: https://doi.org/10.1016/j.rser.2017.03.056.

[47] Y. Huang *et al.*, "A review of power management strategies and component sizing methods for hybrid vehicles," *Renewable and Sustainable Energy Reviews,* vol. 96, pp. 132-144, 2018/11/01/ 2018, doi: https://doi.org/10.1016/j.rser.2018.07.020.

[48] H. Jiang, L. Xu, J. Li, Z. Hu, and M. Ouyang, "Energy management and component sizing for a fuel cell/battery/supercapacitor hybrid powertrain based on two-dimensional optimization algorithms," *Energy,* vol. 177, pp. 386-396, 2019.

[49] T. Zhu, R. Lot, R. G. Wills, and X. Yan, "Sizing a battery-supercapacitor energy storage system with battery degradation consideration for high-performance electric vehicles," *Energy,* vol. 208, p. 118336, 2020.

[50] S. Ahmadi, S. Bathaee, and A. H. Hosseinpour, "Improving fuel economy and performance of a fuel-cell hybrid electric vehicle (fuel-cell, battery, and ultra-capacitor) using optimized energy management strategy," *Energy Conversion and Management,* vol. 160, pp. 74-84, 2018.

[51] P. Atwood, S. Gurski, D. J. Nelson, K. B. Wipke, and T. Markel, "Degree of hybridization modeling of a hydrogen fuel cell PNGV-class vehicle," SAE Technical Paper, 0148-7191, 2002.

[52] O. Hegazy and J. Van Mierlo, "Optimal power management and powertrain components sizing of fuel cell/battery hybrid electric vehicles based on particle swarm optimisation," *International journal of vehicle design,* vol. 58, no. 2-4, pp. 200-222, 2012.

[53] L. Xu, M. Ouyang, J. Li, F. Yang, L. Lu, and J. Hua, "Optimal sizing of plug-in fuel cell electric vehicles using models of vehicle performance and system cost," *Applied Energy,* vol. 103, pp. 477-487, 2013.

[54] J. Snoussi, S. B. Elghali, M. Benbouzid, and M. F. Mimouni, "Optimal Sizing of Energy Storage Systems Using Frequency-Separation-Based Energy Management for Fuel Cell Hybrid Electric Vehicles," *IEEE Transactions on Vehicular Technology,* vol. 67, no. 10, pp. 9337-9346, 2018, doi: 10.1109/TVT.2018.2863185.

[55] X. Wu, X. Hu, X. Yin, L. Li, Z. Zeng, and V. Pickert, "Convex programming energy management and components sizing of a plug-in fuel cell urban logistics vehicle," *Journal of Power Sources,* vol. 423, pp. 358-366, 2019.

[56] S. Ebbesen, C. Dönitz, and L. Guzzella, "Particle swarm optimisation for hybrid electric drive-train sizing," *International Journal of Vehicle Design,* vol. 58, no. 2-4, pp. 181-199, 2012, doi: 10.1504/ijvd.2012.047382.

[57] J. Zhu, L. Chen, X. Wang, and L. Yu, "Bi-level optimal sizing and energy management of hybrid electric propulsion systems," *Applied Energy,* vol. 260, p. 114134, 2020/02/15/ 2020, doi: https://doi.org/10.1016/j.apenergy.2019.114134.

[58] L. Xu, C. D. Mueller, J. Li, M. Ouyang, and Z. Hu, "Multi-objective component sizing based on optimal energy management strategy of fuel cell electric vehicles," *Applied Energy,* vol. 157, pp. 664-674, 2015/11/01/ 2015, doi: https://doi.org/10.1016/j.apenergy.2015.02.017.

[59] T. Ishikawa *et al.*, "Development of next generation fuel-cell hybrid system-consideration of high voltage system," SAE Technical Paper, 0148-7191, 2004.

[60] M. Iqbal *et al.*, "APPLICATION OF EVOLVED EVOLUTIONARY ALGORITHMS FOR THE SOLUTION OF DIFFERENT ASPECTS OF HYDROTHERMAL SCHEDULING–A COMPREHENSIVE OVERVIEW," *The Nucleus,* vol. 50, no. 2, pp. 99-115, 2013.

[61] M. Ashraf, M. O. Ullah, T. Malik, A. Waqas, M. Iqbal, and F. Siddiq, "A Hybrid Water Cycle Algorithm-Least Square based Framework for Robust Estimation of," *The Nucleus,* vol. 55, no. 2, pp. 47-60, 2018.

[62] H. S. Ramadan, M. Iqbal, M. Becherif, and H. Haes Alhelou, "Efficient control and multi-criteria energy scheduling of renewable-based utility grid via pareto-metaheuristic optimizers," *IET Renewable Power Generation,* vol. 16, no. 6, pp. 1246-1266, 2022, doi: https://doi.org/10.1049/rpg2.12444.

[63] N. Murgovski, *Optimal powertrain dimensioning and potential assessment of hybrid electric vehicles*. Chalmers University of Technology, 2012.

[64] X. Hu, N. Murgovski, L. M. Johannesson, and B. Egardt, "Optimal Dimensioning and Power Management of a Fuel Cell/Battery Hybrid Bus via Convex Programming," *IEEE/ASME Transactions on Mechatronics,* vol. 20, no. 1, pp. 457-468, 2015, doi: 10.1109/TMECH.2014.2336264.

[65] A. Valente, D. Iribarren, D. Candelaresi, G. Spazzafumo, and J. Dufour, "Using harmonised life-cycle indicators to explore the role of hydrogen in the environmental performance of fuel cell electric vehicles," *International Journal of Hydrogen Energy,* vol. 45, no. 47, pp. 25758-25765, 2020/09/25/ 2020, doi: https://doi.org/10.1016/j.ijhydene.2019.09.059.

[66] K. Chen, S. Laghrouche, and A. Djerdir, "Aging prognosis model of proton exchange membrane fuel cell in different operating conditions," *International Journal of Hydrogen Energy,* vol. 45, no. 20, pp. 11761-11772, 2020.

[67] J. Han, J. Han, and S. Yu, "Experimental analysis of performance degradation of 3-cell PEMFC stack under dynamic load cycle," *International Journal of Hydrogen Energy,* vol. 45, no. 23, pp. 13045-13054, 2020/04/28/ 2020, doi: https://doi.org/10.1016/j.ijhydene.2020.02.215.

[68] B. Wang *et al.*, "Current technologies and challenges of applying fuel cell hybrid propulsion systems in unmanned aerial vehicles," *Progress in Aerospace Sciences,* vol. 116, p. 100620, 2020.

[69] R. Koubaa, S. Bacha, and M. Smaoui, "Robust optimization based energy management of a fuel cell/ultra-capacitor hybrid electric vehicle under uncertainty," *Energy,* vol. 200, p. 117530, 2020.

[70] S. Farhani and F. Bacha, "Design and hardware investigation of a new configuration of an isolated DC-DC converter for fuel cell vehicle," *Ain Shams Engineering Journal,* vol. 12, no. 1, pp. 591-598, 2021.

[71] N. Sulaiman, M. A. Hannan, A. Mohamed, P. J. Ker, E. H. Majlan, and W. R. Wan Daud, "Optimization of energy management system for fuel-cell hybrid electric vehicles: Issues and recommendations," *Applied Energy,* vol. 228, pp. 2061-2079, 2018/10/15/ 2018, doi: https://doi.org/10.1016/j.apenergy.2018.07.087.

[72] G. Du, Y. Zou, X. Zhang, T. Liu, J. Wu, and D. He, "Deep reinforcement learning based energy management for a hybrid electric vehicle," *Energy,* vol. 201, p. 117591, 2020.

[73] Z. Yang, Q. Du, Z. Jia, C. Yang, and K. Jiao, "Effects of operating conditions on water and heat management by a transient multi-dimensional PEMFC system model," *Energy,* vol. 183, pp. 462-476, 2019/09/15/ 2019, doi: https://doi.org/10.1016/j.energy.2019.06.148.

[74] F. Mojica, M. A. Rahman, J. Mora, J. Ocon, and P. Y. Chuang, "Experimental study of three channel designs with model comparison in a PEM fuel cell," *Fuel Cells,* vol. 20, no. 5, pp. 547-557, 2020.

[75] X. Hu, C. Zou, X. Tang, T. Liu, and L. Hu, "Cost-optimal energy management of hybrid electric vehicles using fuel cell/battery health-aware predictive control," *IEEE Transactions on Power Electronics,* vol. 35, no. 1, pp. 382-392, 2019.

[76] R. Xiong, H. Chen, C. Wang, and F. Sun, "Towards a smarter hybrid energy storage system based on battery and ultracapacitor-A critical review on topology and energy management," *Journal of cleaner production,* vol. 202, pp. 1228-1240, 2018.

[77] M. Yue, S. Jemei, R. Gouriveau, and N. Zerhouni, "Review on health-conscious energy management strategies for fuel cell hybrid electric vehicles: Degradation models and strategies," *International Journal of Hydrogen Energy,* vol. 44, no. 13, pp. 6844-6861, 2019.

[78] H. Zhang, X. Li, X. Liu, and J. Yan, "Enhancing fuel cell durability for fuel cell plug-in hybrid electric vehicles through strategic power management," *Applied Energy,* vol. 241, pp. 483-490, 2019/05/01/ 2019, doi: https://doi.org/10.1016/j.apenergy.2019.02.040.

[79] N. Bizon, "Real-time optimization strategies of Fuel Cell Hybrid Power Systems based on Load-following control: A new strategy, and a comparative study of topologies and fuel economy obtained," *Applied Energy,* vol. 241, pp. 444-460, 2019/05/01/ 2019, doi: https://doi.org/10.1016/j.apenergy.2019.03.026.

[80] N. Bizon, "Real-time optimization strategy for fuel cell hybrid power sources with load-following control of the fuel or air flow," *Energy Conversion and Management,* vol. 157, pp. 13-27, 2018/02/01/ 2018, doi: https://doi.org/10.1016/j.enconman.2017.11.084.

[81] Q. Li, W. Chen, Z. Liu, M. Li, and L. Ma, "Development of energy management system based on a power sharing strategy for a fuel cell-battery-supercapacitor hybrid tramway," *Journal of Power Sources,* vol. 279, pp. 267-280, 2015.

[82] Q. Li, W. Chen, Y. Li, S. Liu, and J. Huang, "Energy management strategy for fuel cell/battery/ultracapacitor hybrid vehicle based on fuzzy logic," *International Journal of Electrical Power & Energy Systems,* vol. 43, no. 1, pp. 514-525, 2012.

[83] M. Yue, S. Jemei, and N. Zerhouni, "Health-Conscious Energy Management for Fuel Cell Hybrid Electric Vehicles Based on Prognostics-Enabled Decision-Making," *IEEE Transactions on Vehicular Technology,* vol. 68, no. 12, pp. 11483-11491, 2019.

[84] Y. Liu, J. Li, Z. Chen, D. Qin, and Y. Zhang, "Research on a multi-objective hierarchical prediction energy management strategy for range extended fuel cell vehicles," *Journal of Power Sources,* vol. 429, pp. 55-66, 2019/07/31/ 2019, doi: https://doi.org/10.1016/j.jpowsour.2019.04.118.

[85] S. N. Motapon, L.-A. Dessaint, and K. Al-Haddad, "A comparative study of energy management schemes for a fuel-cell hybrid emergency power system of more-electric aircraft," *IEEE transactions on industrial electronics,* vol. 61, no. 3, pp. 1320-1334, 2013.

[86] H. Li, A. Ravey, A. N'Diaye, and A. Djerdir, "A novel equivalent consumption minimization strategy for hybrid electric vehicle powered by fuel cell, battery and supercapacitor," *Journal of Power Sources,* vol. 395, pp. 262-270, 2018.

[87] H. Hemi, J. Ghouili, and A. Cheriti, "Combination of Markov chain and optimal control solved by Pontryagin's Minimum Principle for a fuel cell/supercapacitor vehicle," *Energy Conversion and Management,* vol. 91, pp. 387-393, 2015.

[88] Q. Li, W. Huang, W. Chen, Y. Yan, W. Shang, and M. Li, "Regenerative braking energy recovery strategy based on Pontryagin's minimum principle for fell cell/supercapacitor hybrid locomotive," *International Journal of Hydrogen Energy,* vol. 44, no. 11, pp. 5454-5461, 2019.

[89] C. M. Martinez, X. Hu, D. Cao, E. Velenis, B. Gao, and M. Wellers, "Energy management in plug-in hybrid electric vehicles: Recent progress and a connected vehicles perspective," *IEEE Transactions on Vehicular Technology,* vol. 66, no. 6, pp. 4534-4549, 2016.

[90] Z. Hu *et al.*, "Multi-objective energy management optimization and parameter sizing for proton exchange membrane hybrid fuel cell vehicles," *Energy Conversion and Management,* vol. 129, pp. 108-121, 2016/12/01/ 2016, doi: https://doi.org/10.1016/j.enconman.2016.09.082.

[91] C. Gao, J. Zhao, J. Wu, and X. Hao, "Optimal fuzzy logic based energy management strategy of battery/supercapacitor hybrid energy storage system for electric vehicles," in *2016 12th World Congress on Intelligent Control and Automation (WCICA)*, 2016: IEEE, pp. 98-102.

[92] C. Wang, R. Yang, and Q. Yu, "Wavelet transform based energy management strategies for plug-in hybrid electric vehicles considering temperature uncertainty," *Applied Energy,* vol. 256, p. 113928, 2019/12/15/ 2019, doi: https://doi.org/10.1016/j.apenergy.2019.113928.

[93] P. Pany, R. Singh, and R. Tripathi, "Active load current sharing in fuel cell and battery fed DC motor drive for electric vehicle application," *Energy conversion and management,* vol. 122, pp. 195-206, 2016.

[94] A. Same, A. Stipe, D. Grossman, and J. W. Park, "A study on optimization of hybrid drive train using Advanced Vehicle Simulator (ADVISOR)," *Journal of Power Sources,* vol. 195, no. 19, pp. 6954-6963, 2010.

[95] J. Li, Y. Wang, J. Chen, and X. Zhang, "Study on energy management strategy and dynamic modeling for auxiliary power units in range-extended electric vehicles," *Applied Energy,* vol. 194, pp. 363-375, 2017.

[96] X. Hu, N. Murgovski, L. M. Johannesson, and B. Egardt, "Optimal dimensioning and power management of a fuel cell/battery hybrid bus via convex programming," *IEEE/ASME transactions on mechatronics,* vol. 20, no. 1, pp. 457-468, 2014.

[97] X. Wu, X. Hu, X. Yin, Y. Peng, and V. Pickert, "Convex programming improved online power management in a range extended fuel cell electric truck," *Journal of Power Sources,* vol. 476, p. 228642, 2020.

[98] Y. Huang, H. Wang, A. Khajepour, H. He, and J. Ji, "Model predictive control power management strategies for HEVs: A review," *Journal of Power Sources,* vol. 341, pp. 91-106, 2017.

[99] D. Zhou, A. Ravey, A. Al-Durra, and F. Gao, "A comparative study of extremum seeking methods applied to online energy management strategy of fuel cell hybrid electric vehicles," *Energy Conversion and Management,* vol. 151, pp. 778-790, 2017/11/01/ 2017, doi: https://doi.org/10.1016/j.enconman.2017.08.079.

[100] Y. Wang, S. J. Moura, S. G. Advani, and A. K. Prasad, "Power management system for a fuel cell/battery hybrid vehicle incorporating fuel cell and battery degradation," *International Journal of Hydrogen Energy,* vol. 44, no. 16, pp. 8479-8492, 2019/03/29/ 2019, doi: https://doi.org/10.1016/j.ijhydene.2019.02.003.

[101] T. Wang, Q. Li, Y. Qiu, L. Yin, L. Liu, and W. Chen, "Efficiency Extreme Point Tracking Strategy Based on FFRLS Online Identification for PEMFC System," *IEEE Transactions on Energy Conversion,* vol. 34, no. 2, pp. 952-963, 2019, doi: 10.1109/TEC.2018.2872861.

[102] M. S. Ismail, D. B. Ingham, K. J. Hughes, L. Ma, and M. Pourkashanian, "An efficient mathematical model for air-breathing PEM fuel cells," *Applied Energy,* vol. 135, pp. 490-503, 2014/12/15/ 2014, doi: https://doi.org/10.1016/j.apenergy.2014.08.113.

[103] A. Amamou, M. Kandidayeni, A. Macias, L. Boulon, and S. Kelouwani, "Efficient model selection for real-time adaptive cold start strategy of a fuel cell system on vehicular applications," *International Journal of Hydrogen Energy,* vol. 45, no. 38, pp. 19664-19675, 2020/07/31/ 2020, doi: https://doi.org/10.1016/j.ijhydene.2020.04.253.

[104] M. Derbeli, O. Barambones, M. Farhat, J. A. Ramos-Hernanz, and L. Sbita, "Robust high order sliding mode control for performance improvement of PEM fuel cell power systems," *International Journal of Hydrogen Energy,* vol. 45, no. 53, pp. 29222-29234, 2020.

[105] A. M. Fernandez, M. Kandidayeni, L. Boulon, and H. Chaoui, "An Adaptive State Machine Based Energy Management Strategy for a Multi-Stack Fuel Cell Hybrid Electric Vehicle," *IEEE Transactions on Vehicular Technology,* vol. 69, no. 1, pp. 220-234, 2020, doi: 10.1109/TVT.2019.2950558.

[106] C. Balerna, N. Lanzetti, M. Salazar, A. Cerofolini, and C. Onder, "Optimal low-level control strategies for a high-performance hybrid electric power unit," *Applied Energy,* vol. 276, p. 115248, 2020/10/15/ 2020, doi: https://doi.org/10.1016/j.apenergy.2020.115248.

[107] G. A. Munoz-Hernandez, G. Mino-Aguilar, J. F. Guerrero-Castellanos, and E. Peralta-Sanchez, "Fractional Order PI-Based Control Applied to the Traction System of an Electric Vehicle (EV)," *Applied Sciences,* vol. 10, no. 1, p. 364, 2020. [Online]. Available: https://www.mdpi.com/2076-3417/10/1/364.

[108] S. Devi Vidhya and M. Balaji, "Hybrid fuzzy PI controlled multi-input DC/DC converter for electric vehicle application," *Automatika,* vol. 61, no. 1, pp. 79-91, 2020.

[109] Y. Zhou, H. Obeid, S. Laghrouche, M. Hilairet, and A. Djerdir, "A novel second-order sliding mode control of hybrid fuel cell/super capacitors power system considering the degradation of the fuel cell," *Energy Conversion and Management,* vol. 229, p. 113766, 2021/02/01/ 2021, doi: https://doi.org/10.1016/j.enconman.2020.113766.

[110] S. A. Siffat, I. Ahmad, A. U. Rahman, and Y. Islam, "Robust integral backstepping control for unified model of hybrid electric vehicles," *IEEE Access,* vol. 8, pp. 49038-49052, 2020.

[111] D. Shen, C.-C. Lim, and P. Shi, "Robust fuzzy model predictive control for energy management systems in fuel cell vehicles," *Control Engineering Practice,* vol. 98, p. 104364, 2020.

[112] S. Tronci and R. Baratti, "A Gain-Scheduling PI Control Based on Neural Networks," *Complexity,* vol. 2017, p. 9241254, 2017/10/19 2017, doi: 10.1155/2017/9241254.

[113] R. P. Borase, D. Maghade, S. Sondkar, and S. Pawar, "A review of PID control, tuning methods and applications," *International Journal of Dynamics and Control,* pp. 1-10, 2020.

[114] O. A. Somefun, K. Akingbade, and F. Dahunsi, "The dilemma of PID tuning," *Annual Reviews in Control,* 2021.

[115] V. B. Kumar, D. Sampath, V. S. Praneeth, and Y. P. Kumar, "Error Performance Index Based PID Tuning Methods for Temperature Control of Heat Exchanger System," in *2021 IEEE International IOT, Electronics and Mechatronics Conference (IEMTRONICS)*, 2021: IEEE, pp. 1-6.

[116] N. N. B. M. Mazlan, N. M. Thamrin, and N. A. Razak, "Comparison Between Ziegler-Nichols and AMIGO Tuning Techniques in Automated Steering Control System for Autonomous Vehicle," in *2020 IEEE International Conference on Automatic Control and Intelligent Systems (I2CACIS)*, 20-20 June 2020 2020, pp. 7-12, doi: 10.1109/I2CACIS49202.2020.9140089.

[117] A. Ghosh, A. K. Ray, M. Nurujjaman, and M. Jamshidi, "Voltage and frequency control in conventional and PV integrated power systems by a particle swarm optimized Ziegler–Nichols based PID controller," *SN Applied Sciences,* vol. 3, no. 3, pp. 1-13, 2021.

[118] S. Oladipo, Y. Sun, and Z. Wang, "Optimization of PID and FOPID controllers with new generation metaheuristic algorithms for controlling AVR system: Concise Survey," in *2020 12th International Conference on Computational Intelligence and Communication Networks (CICN)*, 2020: IEEE, pp. 280-286.

[119] T. Zhao, Y. Chen, S. Dian, R. Guo, and S. Li, "General type-2 fuzzy gain scheduling PID controller with application to power-line inspection robots," *International Journal of Fuzzy Systems,* vol. 22, no. 1, pp. 181-200, 2020.

[120] G. A. R. Ibraheem, A. T. Azar, I. K. Ibraheem, and A. J. Humaidi, "A novel design of a neural network-based fractional PID controller for mobile robots using hybridized fruit fly and particle swarm optimization," *Complexity,* vol. 2020, 2020.

[121] H. Sartipizadeh, F. Harirchi, M. Babakmehr, and P. Dehghanian, "Robust Model Predictive Control of DC-DC Floating Interleaved Boost Converter With Multiple Uncertainties," *IEEE Transactions on Energy Conversion,* vol. 36, no. 2, pp. 1403-1412, 2021.

[122] D. Zhao, H. Li, Z. Liang, R. Ma, and Y. Huangfu, "Continuous model predictive control of interleaved boost converter with current compensation," *IET Power Electronics,* vol. 13, no. 17, pp. 4079-4088, 2020.

[123] A. Maitland and J. McPhee, "Quasi-translations for fast hybrid nonlinear model predictive control," *Control Engineering Practice,* vol. 97, p. 104352, 2020.

[124] M. A. Majeed, M. G. Khan, and F. Asghar, "Nonlinear control of hybrid energy storage system for hybrid electric vehicles," *International Transactions on Electrical Energy Systems,* vol. 30, no. 4, p. e12268, 2020.

[125] A. Lassioui, H. E. Fadil, A. Rachid, T. Bouanou, and F. Giri, "Adaptive Output Feedback Nonlinear Control of a Wireless Power Transfer Charger for Battery Electric Vehicle," *Journal of Control, Automation and Electrical Systems,* vol. 32, no. 2, pp. 492-506, 2021.

[126] C. Dépature, W. Lhomme, P. Sicard, A. Bouscayrol, and L. Boulon, "Real-time backstepping control for fuel cell vehicle using supercapacitors," *IEEE Transactions on Vehicular Technology,* vol. 67, no. 1, pp. 306-314, 2017.

[127] M. Sellali, A. Betka, S. Drid, A. Djerdir, L. Allaoui, and M. Tiar, "Novel control implementation for electric vehicles based on fuzzy-back stepping approach," *Energy,* vol. 178, pp. 644-655, 2019.

[128] Y. Dai, S. Ni, D. Xu, L. Zhang, and X.-G. Yan, "Disturbance-observer based prescribed-performance fuzzy sliding mode control for PMSM in electric vehicles," *Engineering Applications of Artificial Intelligence,* vol. 104, p. 104361, 2021.

[129] A. Lozynskyy, T. Perzyński, J. Kozyra, Y. Biletskyi, and L. Kasha, "The Interconnection and Damping Assignment Passivity-Based Control Synthesis via the Optimal Control Method for Electric Vehicle Subsystems," *Energies,* vol. 14, no. 12, p. 3711, 2021.

[130] B.-M. Nguyen *et al.*, "Passivity Based Hierarchically Decentralized Range Extension Control of In-wheel-motor Vehicles," in *2021 IEEE International Conference on Mechatronics (ICM)*, 2021: IEEE, pp. 1-6.

[131] P. V. Kokotovic, "The joy of feedback: nonlinear and adaptive," *IEEE Control Systems Magazine,* vol. 12, no. 3, pp. 7-17, 1992, doi: 10.1109/37.165507.

[132] Z. Feng, W. Liang, J. Ling, X. Xiao, K. K. Tan, and T. H. Lee, "Integral terminal sliding-mode-based adaptive integral backstepping control for precision motion of a piezoelectric ultrasonic motor," *Mechanical Systems and Signal Processing,* vol. 144, p. 106856, 2020.

[133] P. Ren, P. Pei, Y. Li, Z. Wu, D. Chen, and S. Huang, "Degradation mechanisms of proton exchange membrane fuel cell under typical automotive operating conditions," *Progress in Energy and Combustion Science,* vol. 80, p. 100859, 2020/09/01/ 2020, doi: https://doi.org/10.1016/j.pecs.2020.100859.

[134] H. Chen, Z. Zhang, C. Guan, and H. Gao, "Optimization of sizing and frequency control in battery/supercapacitor hybrid energy storage system for fuel cell ship," *Energy,* vol. 197, p. 117285, 2020.

[135] A. S. Veerendra, M. R. Mohamed, P. K. Leung, and A. A. Shah, "Hybrid power management for fuel cell/supercapacitor series hybrid electric vehicle," *International Journal of Green Energy,* vol. 18, no. 2, pp. 128-143, 2021.

[136] H. Li, A. Ravey, A. N'Diaye, and A. Djerdir, "Online adaptive equivalent consumption minimization strategy for fuel cell hybrid electric vehicle considering power sources degradation," *Energy Conversion and Management,* vol. 192, pp. 133-149, 2019.

[137] H. Lohse-Busch, K. Stutenberg, M. Duoba, and S. Iliev, "Technology assessment of a fuel cell vehicle: 2017 Toyota Mirai," Argonne National Lab.(ANL), Argonne, IL (United States), 2018.

[138] Z. Hailun, W. Sun, H. Xue, W. Sun, L. Wang, and L. Jia, "Performance analysis and prediction of ejector based hydrogen recycle system under variable proton exchange membrane fuel cell working conditions," *Applied Thermal Engineering,* vol. 197, p. 117302, 2021.

[139] Z. Huang, J. Zhou, Y. Cui, and J. Cao, "Proton exchange membrane fuel cell multi-stack parallel gas supply and load-up experiment," in *IOP Conference Series: Earth and Environmental Science*, 2021, vol. 702, no. 1: IOP Publishing, p. 012028.

[140] Y. Yan, Q. Li, W. Chen, B. Su, J. Liu, and L. Ma, "Optimal Energy Management and Control in Multimode Equivalent Energy Consumption of Fuel Cell/Supercapacitor of Hybrid Electric Tram," *IEEE Transactions on Industrial Electronics,* vol. 66, no. 8, pp. 6065-6076, 2019, doi: 10.1109/TIE.2018.2871792.

[141] S. C. de Almeida and R. Kruczan, "Effects of drivetrain hybridization on fuel economy, performance and costs of a fuel cell hybrid electric vehicle," *International Journal of Hydrogen Energy,* 2021.

[142] T. Wang, Q. Li, X. Wang, W. Chen, E. Breaz, and F. Gao, "A Power Allocation Method for Multistack PEMFC System Considering Fuel Cell Performance Consistency," *IEEE Transactions on Industry Applications,* vol. 56, no. 5, pp. 5340-5351, 2020.

[143] B. Dolenc, P. Boškoski, M. Stepančič, A. Pohjoranta, and Đ. Juričić, "State of health estimation and remaining useful life prediction of solid oxide fuel cell stack," *Energy Conversion and Management,* vol. 148, pp. 993-1002, 2017.

[144] J. Chen, D. Zhou, C. Lyu, and C. Lu, "A novel health indicator for PEMFC state of health estimation and remaining useful life prediction," *International Journal of Hydrogen Energy,* vol. 42, no. 31, pp. 20230-20238, 2017.

[145] H. Li, Y. Zhou, H. Gualous, H. Chaoui, and L. Boulon, "Optimal Cost Minimization Strategy for Fuel Cell Hybrid Electric Vehicles Based on Decision Making Framework," *IEEE Transactions on Industrial Informatics,* pp. 1-1, 2020, doi: 10.1109/TII.2020.3003554.

[146] Z. Zhang, X. Cheng, Z.-Y. Lu, and D.-J. Gu, "SOC estimation of lithium-ion battery pack considering balancing current," *IEEE Transactions on Power Electronics,* vol. 33, no. 3, pp. 2216-2226, 2017.

[147] C. Yang, X. Wang, Q. Fang, H. Dai, Y. Cao, and X. Wei, "An online SOC and capacity estimation method for aged lithium-ion battery pack considering cell inconsistency," *Journal of Energy Storage,* vol. 29, p. 101250, 2020.

[148] Q. Li, T. Wang, C. Dai, W. Chen, and L. Ma, "Power Management Strategy Based on Adaptive Droop Control for a Fuel Cell-Battery-Supercapacitor Hybrid Tramway," *IEEE Transactions on Vehicular Technology,* vol. 67, no. 7, pp. 5658-5670, 2018, doi: 10.1109/TVT.2017.2715178.

[149] W. Kai, R. Baosen, L. Liwei, L. Yuhao, Z. Hongwei, and S. Zongqiang, "A review of modeling research on supercapacitor," in *2017 Chinese Automation Congress (CAC)*, 2017: IEEE, pp. 5998-6001.

[150] J. Wang *et al.*, "Cycle-life model for graphite-LiFePO4 cells," *Journal of power sources,* vol. 196, no. 8, pp. 3942-3948, 2011.

[151] S. Ebbesen, P. Elbert, and L. Guzzella, "Battery state-of-health perceptive energy management for hybrid electric vehicles," *IEEE Transactions on Vehicular technology,* vol. 61, no. 7, pp. 2893-2900, 2012.

[152] G. Saldaña, J. I. San Martin, I. Zamora, F. J. Asensio, and O. Oñederra, "Electric vehicle into the grid: Charging methodologies aimed at providing ancillary services considering battery degradation," *Energies,* vol. 12, no. 12, p. 2443, 2019.

[153] Y. Huangfu, Q. Li, L. Xu, R. Ma, and F. Gao, "Extended state observer based flatness control for fuel cell output series interleaved boost converter," *IEEE Transactions on Industry Applications,* vol. 55, no. 6, pp. 6427-6437, 2019.

[154] A. Berigai Ramaiaha, R. Maurya, and S. R. Arya, "Bidirectional converter for electric vehicle battery charging with power quality features," *International Transactions on Electrical Energy Systems,* vol. 28, no. 9, p. e2589, 2018.

[155] M. S. Khan, I. Ahmad, and F. Z. U. Abideen, "Output voltage regulation of FC-UC based hybrid electric vehicle using integral backstepping control," *IEEE Access,* vol. 7, pp. 65693-65702, 2019.

[156] T. X. Dinh *et al.*, "Modeling and energy management strategy in energetic macroscopic representation for a fuel cell hybrid electric vehicle," *Journal of Drive and Control,* vol. 16, no. 2, pp. 80-90, 2019.

[157] W. Jiang, X. Zhang, F. Guo, J. Chen, P. Wang, and L. H. Koh, "Large-signal stability of interleave boost converter system with constant power load using sliding-mode control," *IEEE Transactions on Industrial Electronics,* vol. 67, no. 11, pp. 9450-9459, 2019.

[158] H. Ye, G. Jin, W. Fei, and N. Ghadimi, "High step-up interleaved dc/dc converter with high efficiency," *Energy sources, Part A: recovery, utilization, and environmental effects,* pp. 1-20, 2020.

[159] G. Zhang, Q. Li, W. Chen, X. Meng, and H. Deng, "A coupled power-voltage equilibrium strategy based on droop control for fuel cell/battery/supercapacitor hybrid tramway," *International Journal of Hydrogen Energy,* vol. 44, no. 35, pp. 19370-19383, 2019.

[160] N. Kittner, F. Lill, and D. M. Kammen, "Energy storage deployment and innovation for the clean energy transition," *Nature Energy,* vol. 2, no. 9, p. 17125, 2017.

[161] A. Badji, D. O. Abdeslam, M. Becherif, F. Eltoumi, and N. Benamrouche, "Analyze and evaluate of energy management system for fuel cell electric vehicle based on frequency splitting," *Mathematics and Computers in Simulation,* vol. 167, pp. 65-77, 2020/01/01/ 2020, doi: https://doi.org/10.1016/j.matcom.2019.02.014.

[162] C. Dépature, W. Lhomme, P. Sicard, A. Bouscayrol, and L. Boulon, "Real-Time Backstepping Control for Fuel Cell Vehicle Using Supercapacitors," *IEEE Transactions on Vehicular Technology,* vol. 67, no. 1, pp. 306-314, 2018, doi: 10.1109/TVT.2017.2728823.

[163] C. Dépature, A. Macías, A. Jácome, L. Boulon, J. Solano, and J. P. Trovão, "Fuel cell/supercapacitor passive configuration sizing approach for vehicular applications," *International Journal of Hydrogen Energy,* 2020.

[164] A. Florescu, S. Bacha, I. Munteanu, A. I. Bratcu, and A. Rumeau, "Adaptive frequency-separation-based energy management system for electric vehicles," *Journal of Power Sources,* vol. 280, pp. 410-421, 2015/04/15/ 2015, doi: https://doi.org/10.1016/j.jpowsour.2015.01.117.

[165] H. Marzougui, A. Kadri, J.-P. Martin, M. Amari, S. Pierfederici, and F. Bacha, "Implementation of energy management strategy of hybrid power source for electrical vehicle," *Energy Conversion and Management,* vol. 195, pp. 830-843, 2019.

[166] P. Thounthong, S. Pierfederici, J. Martin, M. Hinaje, and B. Davat, "Modeling and Control of Fuel Cell/Supercapacitor Hybrid Source Based on Differential Flatness Control," *IEEE Transactions on Vehicular Technology,* vol. 59, no. 6, pp. 2700-2710, 2010, doi: 10.1109/TVT.2010.2046759.

[167] S. J. Bae *et al.*, "Lifetime prediction of a polymer electrolyte membrane fuel cell via an accelerated startup–shutdown cycle test," *International Journal of Hydrogen Energy,* vol. 37, no. 12, pp. 9775-9781, 2012/06/01/ 2012, doi: https://doi.org/10.1016/j.ijhydene.2012.03.104.

[168] X.-Z. Yuan, H. Li, S. Zhang, J. Martin, and H. Wang, "A review of polymer electrolyte membrane fuel cell durability test protocols," *Journal of Power Sources,* vol. 196, no. 22, pp. 9107-9116, 2011/11/15/ 2011, doi: https://doi.org/10.1016/j.jpowsour.2011.07.082.

[169] M. Sandberg, "Convergence of the forward Euler method for nonconvex differential inclusions," *SIAM journal on numerical analysis,* vol. 47, no. 1, pp. 308-320, 2009.

[170] M. Ashraf, M. O. Ullah, T. Malik, A. Waqas, M. Iqbal, and F. Siddiq, "Robust extraction of harmonics using heuristic advanced gravitational search algorithm-based least square estimator," *The Nucleus,* vol. 54, no. 4, pp. 219-231, 2018.

[171] M. U. Ali, B. Habib, and M. Iqbal, "Fixed head short term hydro thermal scheduling using improved particle swarm optimization," *The Nucleus,* vol. 52, no. 3, pp. 107-114, 2015.

[172] "ETC test cycle, developed by the FIGE Institute, Aachen, Germany, FIGE Report 104 05 316, January 1994, 06040 http://www.dieselnet.com/standards/eu/hd.php."

[173] P. Keil, M. Englberger, and A. Jossen, "Hybrid energy storage systems for electric vehicles: An experimental analysis of performance improvements at subzero temperatures," *IEEE Transactions on Vehicular Technology,* vol. 65, no. 3, pp. 998-1006, 2015.

[174] T. Delaforge, "Optimal sizing of passive components in power converters using discrete methods," Université Grenoble Alpes, 2016.